AUTOMATED DESIGN OPTIMIZATION OF SYNCHRONOUS MACHINES: DEVELOPMENT AND APPLICATION OF A GENERIC FITNESS EVALUATION FRAMEWORK

A Dissertation

by

YATEENDRA BALKRISHNA DESHPANDE

Submitted to the Office of Graduate and Professional Studies of
Texas A&M University
in partial fulfillment of the requirements for the degree of

DOCTOR OF PHILOSOPHY

Chair of Committee,	Hamid A Toliyat
Committee Members,	Robert S Balog
	Shankar Bhattacharyya
	Alan Palazzolo
Head of Department,	Chanan Singh

December 2014

Major Subject: Electrical Engineering

ABSTRACT

A rotating synchronous electric machine design can be described to its entirety by a combination of 17 to 24 discrete and continuous parameters pertaining the geometry, material selection, and electrical loading. Determining the performance attributes of a design often involves numerical solutions to thermal and magnetic equations. Stochastic optimization methods have proven effective for solving specific design problems in literature. A major challenge to design automation, however, is whether the design tool is versatile enough to solve design problems with different types of objectives and requirements.

This work proposes a black-box approach in an attempt to encompass a wide variety of synchronous machine design problems. This approach attempts to enlist all possible attributes of interest (AoIs) to the end-user so that the design optimization problem can be framed by combination of such attributes only. The number of ways the end-user can input requirements is now defined and limited. Design problems are classified based on which of the AoI's are constraints, objectives or design parameters. It is observed that regardless of the optimization problem definition, the evaluation of any design is based on a common set of physical and analytical models and empirical data. Problem definitions are derived based on black-box approach and efficient fitness evaluation algorithms are tailored to meet requirements of each problem definition.

The proposed framework is implemented in Matlab/C++ environment encompassing different aspects of motor design. The framework is employed for designing synchronous machines for three applications where designs based on

conventional motor construction did not meet all design requirements. The first design problem is to develop a novel bar-conductor tooth-wound stator technology for 1.2 kW in-wheel direct drive motor for an electric/hybrid-electric two wheeler (including practical implementation). The second design problem deals with a novel outer-rotor buried ferrite magnet geometry for a 1.2 kW in-wheel geared motor drive used in an electric/hybrid-electric two wheeler (including practical implementation). The third application involves design of an ultra-cost-effective and ultra-light-weight 1 kW aluminum conductor motor.

Thus, the efficacy of automated design is demonstrated by harnessing the framework and algorithms for exploring new technologies applicable for three distinct design problems originated from practical applications.

DEDICATION

To my family

ACKNOWLEDGEMENTS

First and foremost, I would like to acknowledge the several past and present researchers of electric machines who dedicated their lives to advancement and understanding of this field for sharing their knowledge.

I consider myself lucky to get the opportunity of working with my supervisor Prof. Hamid A. Toliyat. I thank him for his continuous support and engagement, his valuable time, his commitment to excellence in research, his patience and his sense of humor.

I am grateful to my committee members Dr. Robert S Balog, Dr. Shankar P Bhattacharyya and Dr. Alan Palazzolo. I learnt a lot from attending their courses and advising during the course of study at Texas A&M. I would especially like thank Dr. Bhattacharyya for offering me a TA position for his course when I needed it most.

I would also like to thank ECE department staff - Tammy Carda, Jeanie Marshall, Eugenia Costa, Anni Brunker, Sheryl Mallett and Rebecca Rice, who have always been very pleasant and helpful.

I would like to thank TVS Motor Company, India for collaboration on development of tooth-wound bar conductor topology for closed slot stators. I am grateful to my ex-colleagues from TVS Motor Company - Sreeju Nair and Dr. Jabez Dhinagar for their support and enthusiasm in developing this technology.

I would like to mention the support of EMERF in framing the problem statement for the third design study in this dissertation and providing research grant for this study.

I would also like to thank EMERF for inviting me for a student presentation at SMMA Fall Technical Conference 2012.

I express my deep gratitude to my colleagues at EMPE lab and EPPEI group at Texas A&M University for their help in conducting experiments, building test setups and technical discussions. I would like to especially thank Vivek Sundaram, Dr. Siavash Pakdelian, Dr. Robert Vartanian, Matthew Johnson, Jaebum Park, Morteza Moosavi, Dr. Mahshid Amirabadi and Dr. Babak Farhangi for their help, friendship and maintaining a lively environment in lab. I would like to thank several of my friends and well-wishers for making my stay at College Station easy and memorable.

Last but not the least I would like to thank my parents, my wife Deepti and my brother Viraj for their love, patience, selfless support and encouragement over the years. This work would not have been possible without their support.

NOMENCLATURE

Abbreviations

ac	Alternating current
AoI	Attribute of interest
CPSR	Constant power speed ratio (Ratio of maximum to minimum speeds at which a machine can deliver rated power for voltage limited operation)
FEM/FEA	Finite element method/analysis
FW	Field weakening
GA	Genetic algorithm
HTC	High throughput computing
IPM / IPMSM	Internal permanent-magnet machine / Internal permanent magnet Synchronous Machine
MEC	Magnetic equivalent circuit
MTPA	Maximum torque per ampere
PM	Permanent magnet
SPM	Surface-mounted permanent-magnet machine
UCG	Un-controlled generation

Letter symbols

A_c	Conductor area in slot
A_z	z-component of vector magnetic potential
C^{θ}_{x}	Thermal heat capacity of component 'x' of the electric machine
h_M	Magnet height (along direction of magnetization)
i_d, i_q	d- and q- axis currents
I_{demag}	The current magnitude at which demagnetization begins if applied on

	the –d axis at most vulnerable temperature for the permanent magnets
I_{mas}	Maximum current magnitude the machine is subjected to
J_c	Conductor current density
J_z	z- i.e. axial component of the conductor current density
k_{dn}	Distribution factor for the n^{th} harmonic
k_{pn}	Pitch factor for the n^{th} harmonic
k_{sn}	Skew factor for the n^{th} harmonic
k_{wn}	Winding factor for the n^{th} harmonic (including pitch, distribution and skew factors)
l_{ax}	Axial length of the stator including end-windings and end connections
L_d, L_q	d- and q- axis inductances
L_{d_2D}, L_{q_2D}	d- and q- axis inductances for 1-turn per coil for 1mm of symmetric slice of the machine (e.g. half machine for 10-pole 12-slot config)
l_{stack}	Stack length
n_{pitch}	The pitch of each lap-wound coil in terms of number of slots
N_p	Number of poles
N_s	Number of stator slots
n_t	Number of turns per coil
$p^1{}_c$	Hysteresis loss coefficient for unit length of the machine under a particular current excitation
$p^1{}_h$	Eddy current loss coefficient for unit length of the machine under a particular current excitation
P_{core}	Core loss in the machine
P_{Cu}	Joule conduction loss in the machine
P_{loss}	Sum of all losses inside the machine

$R^{\theta}_{x,y}$	Thermal resistance between components *x* and *y* of the machine
r_{ph}	Phase resistance of the motor
R_{ri}	Rotor inner radius
R_{ro}	Rotor outer radius
R_{si}	Stator inner radius
R_{so}	Stator outer radius
SO	Slot opening
spp	Slots per pole per phase
SW	Slot width
T_{em}	Electromagnetic torque developed in the machine
T_{out}	Output torque seen at the shaft of the machine
TW	Tooth width
V_{Cu}	Volume of copper in the machine
V_{dc}	DC bus voltage of the inverter used to drive the machine
$V_{fundamental}$	Line voltage of the machine assuming one turn per coil and maximum possible parallel connections in stator

Greek symbols

α_{se}	Stator skew angle in electrical degrees
α_{sm}	Stator skew angle in mechanical degrees
β_{sm}	Geometrical angle between conductor of skewed stator with the transverse *x*-*y* plane
γ	Angle of current vector from q-axis
κ_{ac}	AC loss coefficient (based on total losses)
λ_M	Peak permanent magnet flux linkage for one phase

ρ_{air}	Mass density of air
ρ_{Al}	Mass density of aluminum
ρ_{Cu}	Mass density of copper
$\sigma^0_{Al}, \sigma_{Al}$	Electrical conductivity of aluminum (the '0' in superscript indicates temperature of 0 º C
$\sigma^0_{Cu}, \sigma_{Cu}$	Electrical conductivity of copper (the '0' in superscript indicates temperature of 0 º C
ω_e	Electrical fundamental angular frequency of operation (rad/s)
ω_r	Rotor mechanical speed of rotation (rad/s)

TABLE OF CONTENTS

Page

LIST OF FIGURES

Page

LIST OF TABLES

Page

1. INTRODUCTION

1.1. The need for design automation

Synchronous electrical machine drives are a subsystem of a plethora of industrial, transport and appliance systems; to mention a few examples – electric/hybrid electric vehicles, wind generators, home appliances, airplanes, pumps, fans, etc. In several cases, the performance, size, cost, efficiency of this subsystem is central to the feasibility or competitiveness of the system. Often, the system designer needs to understand if the chosen subsystem is "optimal" for the application in question. The tradeoff between different performance metrics of the electrical machine subsystem is also of great interest to the system designer. Similarly, material scientists need to understand whether improvement of a certain material for application in electric machines would be of significant interest to certain applications. Critical materials need to be replaced with certain more available ones if threat of supply scarcity exists as was a big concern with the use of rare-earth based permanent magnets in the last few years. All these scenarios call for an automated design tool that can optimize the design based on the end-user's requirements and help identify the correct combination of topology, materials, geometry and electrical loading for achieving multiple objectives. Desirable properties of such a tool can be listed as:

1. Applicable to wide variety of design scenarios and design analysis problems
2. Needs minimum intuition or judgment from the end-user[1]
3. Accurate i.e. one that gives a true optimum and therefore based on accurate model of the machine
4. Returns results in realistic time that the end user can afford to wait
5. Utilizes reasonable computing resources
6. Agile: one that can be easily extended beyond existing geometries, materials, analysis methods or problem definitions

[1]The end-user of the electric machine design tool is the system designer/material/ scientist/ business decision maker who understands design requirements of the desired electric machine

The first challenge in design automation is to understand the end-user's requirement and frame an optimization problem based on it. The end-user may choose to define the design problem in numerous different ways. To the best of my knowledge, no attempt has been made so far for classifying the problems or enumerating different possible ways it can be defined. This dissertation makes a modest attempt in classifying and identifying classes of design problems. However, it is by no means an attempt to encompass all design problems. The second challenge lies in understanding how the common framework of models and methods can be harnessed for addressing different classes of problem definitions while ensuring accuracy of the models and fast convergence towards optimum designs.

1.2. Description of the machine design and scope

The stator of the synchronous machine consists of slotted silicon steel laminations. Depending on the application, the rotor could be inside the stator or it could encapsulate the stator, which is known as outer-rotor topology. The rotor may be a round-rotor or salient pole rotor and may or may not have magnets. The design of magnetically active components of a motor can be described in terms of 11 parameters or group of parameters as listed in Table 1.

As an example, all the parameters required to describe the 2-dimensional geometry of an outer-rotor surface-mounted permanent magnet motor (SPM) is shown in Figure 1. The machine design for this type of SPM is described in its entirety by a minimum of 17 parameters [1] which include geometric, material selection and electrical

loading parameters. In all cases, it is assumed that the machine is driven by a converter that generates a sinusoidal voltage at the synchronous frequency of the machine.

Most problem definitions considered in this text use the machine in its 'motoring' mode i.e. when the machine delivers mechanical power to the load. With a modified set of analytical equations, the framework can be adapted for using the machine in the generating mode. Another possibility of using polyphase machines (more than 3 phases) is not covered directly, but may be easily incorporated into the proposed framework with some additional equations.

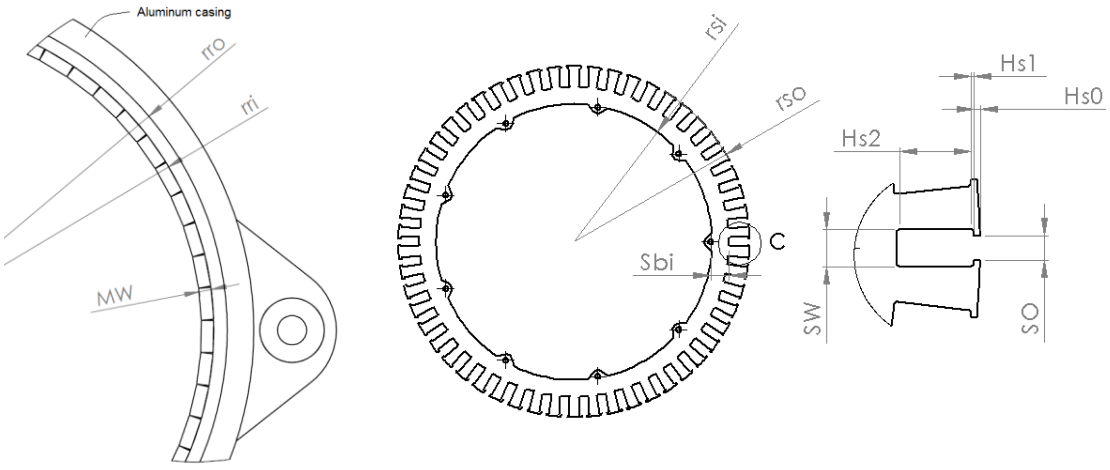

Figure 1 A simple surface permanent magnet geometry description

Table 1 Parameters required for describing the electric machine

#	Parameter	Description:
1	Outer diameter	The outermost diameter i.e. stator diameter ($2 \cdot R_{so}$) for inner rotor machine or rotor outer diameter ($2 \cdot R_{ro}$) for outer-rotor machines
2	Stack length	Axial length of the machine. It is the total length of the machine including end-windings and winding interconnections
3	Pole-spp combination	Valid spp (slots per pole per phase) combinations with even-numbered periodicity generated If(skew==0) and cogging/ripple is an objective along with at least one of cost/volume/efficiency/capability, then spp = all possible to be included
4	Air-gap split ratio	R_{ro}/R_{so} for inner rotor motors and Rso/R_{ro} for outer rotor motors
5	Rotor type	Each rotor structure is assigned a number, the value of this design parameter chooses from available rotor types.
6	Rotor internal geometry	This array of 3-8 parameters is interpreted based on choice of rotor type and rotor geometry is constructed based on it
7	Stator slot geometry	This set of 4 or 5 parameters defines the stator geometry per-unitized to radial length of the stator
8	Material selections	Selection of materials for stator and rotor is encoded in this parameter
9	Windings	Winding wire gauge and insulation type are encoded in this parameter
10	Slot fill	Percentage of actual fill factor to the maximum possible fill factor for the chosen stator geometry and wire diameter
11	Current density	The ratio of actual current loading to the maximum permissible current loading based on thermal constraint

Different rotor structures are used for achieving required parameter values, tradeoffs between rotor saliency, magnet flux, demagnetization characteristics, cost, etc. Figure 2 illustrates a few rotor structures for four-pole rotors proposed in prior literature. Each choice of rotor structure requires a different set of parameters to define its geometry. The minimum defining parameters for the machine could be anywhere between 17 and 24 depending on the choice of rotor geometry. It will be shown later that the choice of rotor type is not obvious and depends heavily on the design requirements

and parameters like pole count, permanent magnetic material, thermal limit on electric loading, etc

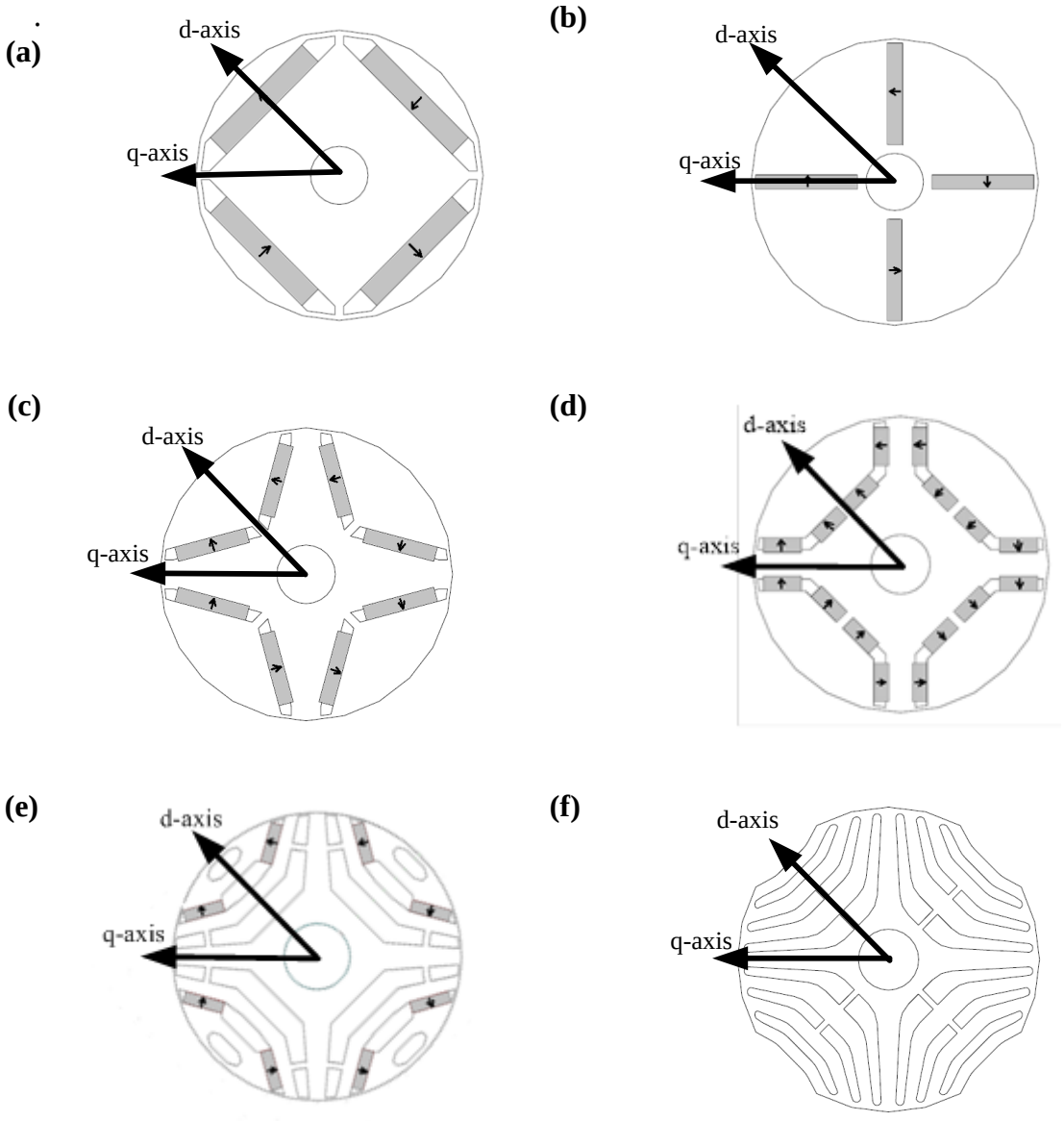

Figure 2 Different rotor shape proposed and studied in literature: (a) inset magnets, (b) spoke type magnets, (c) V-shaped magnets, (d) trough type magnets, (e) double layer rotor with magnets in first barrier, and (f) three layer SynRM

The electric machines discussed in this dissertation are limited to transversally laminated rotating machines that can be analyzed by means of 2-D Finite Element Analysis (FEA). Machines such as linear machines, axial flux machines, stepper motors, and transverse flux machines are considered out of scope of this dissertation.

1.3. The black-box approach

In an attempt to cover a wide variety of ways the end-user may define the design problem, a black-box approach is followed. As can be seen from the table, certain parameters of interest to the user that appear frequently are: attributes of the black-box (outer diameter, active length, volume, weight, cost, durability, and operating temperature), mechanical output/input metrics (torque, cogging torque, torque ripple, constant power speed ratio (CPSR)) and electrical input/output metrics (voltage, current, efficiency, power factor & frequency). These are termed as Attributes of Interest (AoI's) in this text.

Based on this, and a few more practical applications, eighteen AoI's identified are listed in Table 2. The end-user may define the problem that can have a combination of these AoI's as their objective or constraint. Objectives or constraints may contain an algebraic expression of two or more of these AoI's. Certain AoI's can achieve equality constraints by direct elimination as they are based on a direct closed equation. For instance, an equality constraint on volume/cost/weight can be met by choosing l_{ax} once R_{so} is set. Similarly, an inequality constraint on volume/weight/cost can be met by choosing the upper limit on l_{ax} based on R_{so}. It is known that certain AoI's are required to be minimized while others are to be maximized when they appear as objectives.

Similarly, constraints on these can be greater than or less than depending on the physical sense of the AoI. For instance, a problem statement may never ask for minimizing efficiency or may never have a less than constraint on it.

Table 2 Attributes of interest to the end user

	Attribute	As objective	As constraint
(i)	Outer radius	Minimize	Less than, Equal to
(ii)	Axial length	Minimize	Less than, Equal to
(iii)	Torque @ speed capability (thermally/magnetically limited – continuous/short time duty/ positive or braking)	Maximize	Greater than
(iv)	Power capability (thermally, mechanically or electrically limited),	Maximize	Greater than
(v)	Constant power speed ratio	Maximize	Greater than
(vi)	Weight / Moment of inertia	Minimize	Less than, Equal to
(vii)	Cost (& Materials availability, standards)	Minimize	Less than, Equal to
(viii)	Efficiency (at a fixed point/efficiency map for different operating points)	Maximize	Less than, Equal to
(ix)	Insulation life (mean time to failure of insulation)	Maximize	Greater than
(x)	Torque ripple and vibration	Minimize	Less than
(xi)	Cogging torque	Minimize	Less than
(xii)	No-load loss	Minimize	Less than
(xiii)	Uncontrolled generation current within operating speed range	Minimize	Less than
(xiv)	Power factor/ VA of the inverter	Maximize	Less than. Equal to
(xv)	Operating current	Minimize	Less than
(xvi)	Terminal voltage	Minimize	Less than
(xvii)	Temperature rise	Minimize	Less than

Thus it is assumed that the objective functions $\boldsymbol{O_m(X)}$, inequality constraint functions $\boldsymbol{h_m(X)}$ and equality constraints $\boldsymbol{g_j(X)}$ are defined by the end-user based on the AoI's of Table 2 when treating the machine as a black-box. Having defined the AoI's, next the rules of creating a well-defined design problem need to be established.

The black-box approach would thus cover most design problems from a designer would face and would allow for complete automation of the design process with some additional effort. However, there can be several practical design problems where the design algorithm needs to be tailored. For example, designing a motor around a given fixed slot geometry, or two designs that use the exact same block magnet dimensions, optimization of the rotor for a fixed stator [2], etc. It could also involve inclusion of certain aspects of the system/application into the design algorithm

1.4. Nature of design problems

Sizing of the machine (in terms of volume/cost/weight) and the capability of the machine (in terms of output torque or power) are strongly interrelated. The end-user may be interested in three kinds of problem definitions (classified based on constraint): (i) where required machine output or operating conditions (power or torque for motoring and output electrical power for generating) is known and at least one of volume, weight or cost is an objective for minimization, or (ii) where the volume/cost/weight is fixed and the capability of the machine needs to be maximized or (iii) where the volume/cost/weight and operating points – both are fixed. Furthermore, design problems can be classified based on whether the operating point is defined by specifying both the

speed and torque or whether the end-user is concerned about output power but not the speed which is left as a design parameter.

1.4.1. Case 1: Problems with known output power/torque

As graphically shown in Figure 3, the end user specifies different operating points in terms of output torque and shaft speed. By specifying the operating points, the user implicitly defines the thermal, mechanical and magnetic constraint on capability. Additionally, the user also specifies whether the output is continuous duty, drive cycle or short duty and time for which peak torque is required to be delivered if short duty. The efficiency constraint can be defined at each point separately as shown for the i^{th} point in the graph or it may be a weighted sum of efficiencies at different point. If the design problem does not involve field weakening operation, then the capability constraints are derived from the "dominating" operating points. If the problem defines that VA of the drive is limited, and permits field weakening operation, then the thermal limits are derived from the constant power curve and the constant torque line as shown in Figure 3(b). This type of specification imposes a constraint on CPSR. Another possibility is that the user may specify an output power requirement but choose not to specify the speed. Operating speed becomes a design variable in this case.

1.4.2. Case 2: Problems with fixed machine volume, weight or cost

Only one of size, cost or weight can be specified to be constant with the others optionally appearing as objectives. If size is fixed and there is no constraint on cost or weight, then the slot fill is assumed to be maximum, otherwise slot fill is also considered as an input. With this type of problem definition, it is assumed that the continuous time

capability in terms of torque or power is an objective. The objective for short time duty can be maximizing the torque for a fixed short duration or it could be the maximizing the duration for a specified torque.

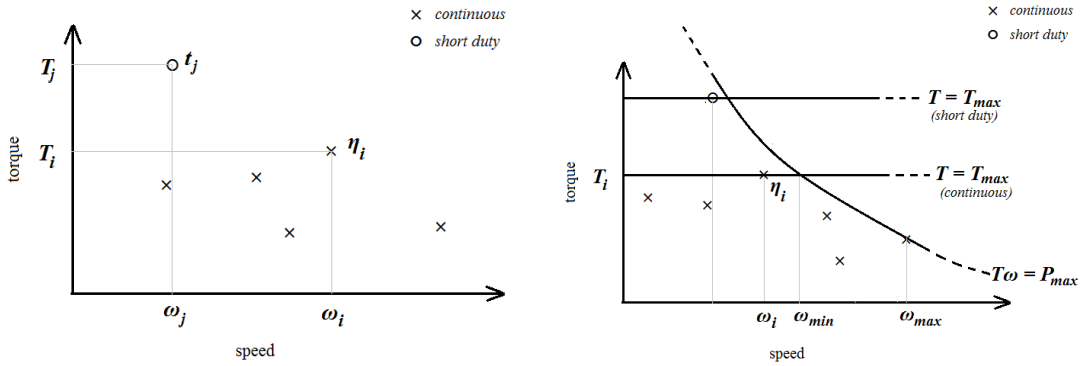

(a) **(b)**

Figure 3 User inputs for known operating points (a) with no limitation on drive size and (b) drive VA limited operation

1.4.3. Case 3: Problems with fixed volume/weight/cost and fixed output

As a third possibility, a user may define the problem by specifying one of volume, cost or weight as constant while also specifying operating points. In this case, certain individuals in the population may violate the thermal or magnetic constraint. If it is not known whether any feasible solution exists for a design problem definition, one of the constraints is converted to an objective to make the problem well-defined.

The category of design problems from the above description will determine which of the design parameters of Table 1 are fixed or can be included as design parameters in the optimization or can be internally determined by the fitness function. Fitness function algorithms are tailored for each problem definition in order to ensure

that all or some of the constraints are met or, in some cases, the likelihood of convergence is increased.

1.5. List of contributions

This dissertation proposes a generic evaluation framework to implement a design optimization tool – a significant step toward complete design automation. Additionally, to ensure the validity of the tool, design studies are performed and evaluated on actual prototypes. Original contributions are listed here:

1) An integrated structure that consolidates elements of machine design, that can be adapted easily to address different types of design problems based on the black-box approach is proposed
2) Design study 1: A semi-closed slot single tooth wound bar-conductor topology is proposed for high peak torque rating applied to in-wheel traction application. Detailed design study is presented with prototype implementation.
3) Design study 2: Buried PM structure is proposed for an outrunner rotor topology. Detailed design study is presented with prototype implementation.
4) Design study 3: Machine geometry that replaces copper conductors in stator with aluminum conductors and achieves the same efficiency and weight objectives is proposed for general purpose application.

1.6. Organization of the dissertation

The dissertation is organized as follows: Section 1 states the motivation of this work and provides background information related to the scope of work of this dissertation. List of contributions is also described in this chapter.

Chapter 2 gives an overview of synchronous machines and provides a summary of prior work related to modeling techniques used for synchronous machine design optimization and presents a review of design problems studied in literature.

Chapter 3 presents the high level organization of the proposed framework and describes the various components of the framework. Additionally, construction of fitness functions for solving some example design problems using the proposed framework is discussed.

Chapter 4 presents the detailed design study of the in-wheel direct drive machine The thermal-electromagnetic model of the machine is calibrated based on a prototype machine. The developed model is used for optimizing SPM machine with multi-strand conductors and bar-conductors to show that superior short duty capability can be achieved using bar-conductors.

Chapter 5 presents the detailed design study of the geared electric wheel machine. This topology is optimized to meet the design requirements for the same vehicle as section 5, but with a geared drive. The multi-objective optimization shows that the outer-rotor buried magnet topology can achieve good performance using ceramic PMs.

Chapter 6 presents the design study for a 1kW general purpose machine. Different stator geometry and winding topologies are compared with specific focus on comparing use of aluminum and copper conductors.

Chapter 7 discusses the learnings and analyzes aspects of machine design in reference of this dissertation work and concludes with recommendations for future work.

2. SYNCHRONOUS MACHINE DESIGN OPTIMIZATION:THEORY AND LITERATURE REVIEW

2.1. Modeling the synchronous machine

2.1.1. The electric lumped circuit model of the synchronous machine

The three-phase synchronous alternating current (ac) brushless machine is electrically modeled by transforming the three phase currents and voltages to an equivalent two phase machine with decoupled direct (d-) axis and quadrature (q-) axis circuits [3]. The average electromagnetic torque T_{em} over an electrical cycle is derived from this linear material model in rotor frame of reference and expressed as:

$$T_{em} = \frac{3}{2}\frac{N_p}{2}\left(\lambda_{\mathrm{M}} i_q + (L_d - L_q) i_d i_q\right) \tag{1}$$

where

N_p : number of poles on rotor

λ_M: permanent magnet flux linkage

L_d, L_q: d- and q axis inductances

i_d, i_q: d-and q- axis current components

The convention followed throughout the dissertation is that the d-axis is the axis which links the PM flux and has a smaller inductance as compared to the q-axis (L_d<L_q) for salient pole rotors. This convention is depicted in Figure 4 for SPM and in Figure 2 for various other rotor structures

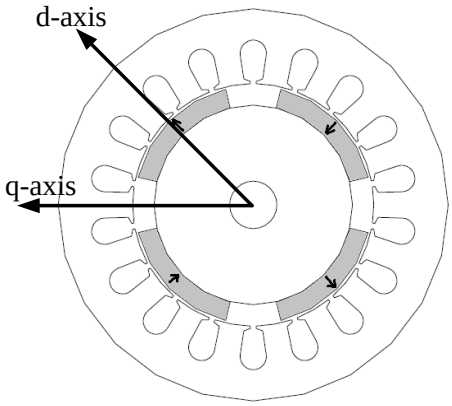

Figure 4 Stator and rotor of a 4-pole 18 slot SPM motor

The torque expression (1) has two components: the first term represents the reactance and the second term represents the reluctance torque. If an SPM rotor is chosen, the d-axis and q-axis inductances are equal and hence the second term in torque equation disappears. If a magnet-less synchronous reluctance rotor (SynRM) as in Figure 2(f) is considered, it results is zero reactance torque. If other rotor structures with a salient rotor and embedded magnets like Figure 2(a-e) are used, then both terms in the torque equation would be non-zero. To minimize conduction loss in stator, a SPM is operated with $i_d=0$ and a SynRM with $i_d=i_q$. In case of a salient pole PM motor, the maximum torque per ampere (MTPA) condition is achieved for the current angle

$$\gamma_{MTPA} = sin^{-1}\left(\frac{-\lambda_M + \sqrt{\lambda_M^2 + 8\left(L_q - L_d\right)^2 I_s^2}}{4\left(L_q - L_d\right) I_s}\right) \qquad (2)$$

where

I_s : magnitude of current, i.e. $\sqrt{i_d^2 + i_q^2}$

γ_{MTPA}: MTPA current angle; current angle γ: $tan^{-1}\left(\frac{i_d}{i_q}\right)$

The magnitude of current (I_s) is limited by thermal and magnetic constraints. The peak temperature of stator winding is limited by the choice of thermal class of insulation material and the mean time to failure of insulation correlates strongly with its operating temperature. It is assumed throughout this dissertation that operating environment and cooling method of the machine is known and specified by the end-user. Permanent magnets lose magnetization if regions inside the magnets are subjected to magnetic fields beyond "knee point" of the material. This imposes a second constraint on the maximum stator current magnitude.

Besides torque production and loss minimization, it is also important to operate the motor with a limit on voltage. The machine is driven by an inverter drive and the cost of the inverter increases with its VA (Volt-Ampere) rating. The equivalent 2-axes electrical circuit model of the machine is given by:

$$v_q = r_{ph} i_q + \omega_e (\lambda_M + L_d i_d) \tag{3}$$

$$v_d = r_{ph} i_d - \omega_e L_q i_q \tag{4}$$

where v_d and v_q are the stator phase voltages transformed to the synchronous rotating frame, r_{ph} is the phase resistance and ω_e is the electrical frequency in rad/s. These equations are represented graphically as vectors as shown in Figure 5.

For a motor that operates delivering rated torque (T_{rated}) at a fixed rated speed (ω_r), minimizing the inverter volt-ampere (VA) is the same as maximizing the power factor of the motor. However, if the application requires the motor to produce the rated power over a wide range of speeds, it is possible to achieve it without increasing the size of the inverter. This is done by simply advancing the current angle so that the last two terms in (3) oppose each other [4-6], thus limiting the magnitude of voltage. The

advancing of current angle keeping current magnitude within rated limits to achieve higher speeds so that the motor no longer operates at MTPA is called field weakening (FW) operation. The ratio of maximum speed at rated power to minimum speed with rated power under voltage constrained operation is called constant power speed ratio (CPSR). This linear model gives an idea of the basic working of the system and an approximate estimate of expected torque and ohmic losses. The equivalent circuit parameters need to be derived from the magnetic model. Apart from calculating the equivalent circuit parameters, the magnetics model of the machine would cover deeper effects such as saturation of lamination cores, torque ripple, core loss, etc.

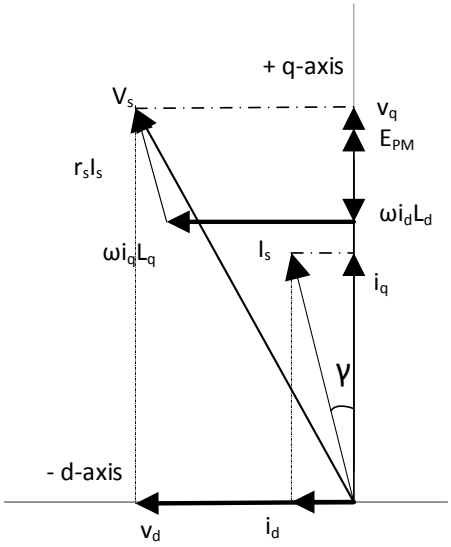

Figure 5 Vector representation of the voltages and currents of the 2-axis equivalent circuit

2.1.2. Magnetics model of the synchronous machine

Though the two-axis linear model is useful in understanding trends in torque and voltage, the actual machine may deviate from the linear model. Due to saturation of the

stator and/or rotor cores, the two inductances L_d and L_q are functions of stator current component aligned with the respective axis and in certain cases of the other axis. The lumped electrical circuit considered in this dissertation ignores the cross coupling between d- and q- axis inductances. Average machine performance can be predicted if the machine constants λ_M, $L_d(i_d)$, $L_q(i_q)$ and r_{ph} are computed from the specified machine design. Three common techniques are used for approximating the field inside the machine: analytical field models, magnetic equivalent circuits (MEC's) with non-linear elements and finite element method (FEM). Analytical methods have proven to give close to accurate results for calculation of magnetic fields in air-gaps and PMs for simple geometries like the surface mounted PM (SPM) machine [7, 8]. MECs have been developed for certain more complex geometries [9-11] that can incorporate soft magnetic material non-linearity as well as effects of moving parts [9]. While the analytical and MEC approaches are less computation intensive, they suffer from the following general drawbacks:

1. The model is based on an approximation of the field and cannot be validated to be correct for wide range of input parameters, thus compromising fidelity of the results.
2. The model does not extend to all types of geometries and tedious modeling exercise needs to be repeated for each choice of stator/rotor geometry.
3. Several effects of interest such as cogging torque, torque ripple are not easily modeled by this type of analysis.
4. The average model of the magnet does not predict demagnetization accurately as partial demagnetization requires the knowledge of field inside the magnet.

Despite these drawbacks, these methods can surely be used in situations where accuracy of the model is verified over wide range of feasible designs of the geometry. Analytical and MEC models are commonly used for initial sizing of the machine as well.

Finite Element Method (FEM) formulation meshes any given geometry to numerically solve a special case of Maxwell's equations. For a magneto-static analysis, the special case Maxwell's equation that assumes the z component of magnetic field $B_z=0$ and $\frac{\partial \boldsymbol{E}}{\partial t} = 0$ is solved for the magnetic potential for the anhysteretic isotropic equation at zero frequency [12]:

$$\frac{\partial}{\partial x}\left(\frac{1}{\mu(|B|)}\frac{\partial A_z}{\partial x}\right) + \frac{\partial}{\partial y}\left(\frac{1}{\mu(|B|)}\frac{\partial A_z}{\partial y}\right) = -J_z - J_{PM} \tag{5}$$

Here, J_z is the externally applied current density in the z direction and J_{PM} is the effective current density that is required to horizontally shift the PM demagnetization curve so that it passes through the origin and the material can be represented by a linear material with the same permittivity as calculated from the slope of the demagnetization curve. This method works well for most PM materials like grades of NdFeB, SmCo and hard magnetic ferrites as long as the operating point on the demagnetization curve is above the 'knee point,' beyond which the material may experience a permanent change in magnetic property.

A linear approximation of this method assumes that permeability of the material is constant. This method may give close to accurate results for SPM geometry because the lamination core material operates well below saturation point on its B-H characteristic. However, it may lead to large inaccuracies in case of buried magnet

topologies or any topology that is characterized by thin bridges in the rotor or stator geometries. A next level of approximation called the ‘frozen permeabilities’ approach [13] is used to speed up convergence for consecutive computations for different current excitation by linearizing permeability based on one non-linear solution found for the first step. A further study challenged the validity of this model as it is not based on direct physics while acknowledging the difficulty in verifying results experimentally[14]. This work borrows the idea of using permeabilities of elements from a previous computation from this method, but limits its use only as an initial guess, thus leading to faster convergence. This is explained further in section 3.5.

With the aim of harnessing FEM for design purposes, Ionel and Popescu [15, 16] proposed a further improvement in FEM specific for investigating the torque, flux and core loss in an electric machine. This model extracts the three phase flux data from a small number of magneto-static simulations for a 60° electrical angle rotation and assembles the 360° electrical angle waveform of the fluxes and magnetic fields by using a ‘space-time’ transform. The torque is computed from the flux after extracting the significant harmonics in the flux waveform. This means the user has control over how many significant harmonics to account for in the torque and core loss calculations. This method was further improved by separately accounting for cogging torque [17]. Further, the field data was used in conjunction with an approximate model of currents induced in PMs to calculate PM eddy current losses [18].

A model of the machine based on FEM overcomes the difficulties faced by other approximation methods. Prior to development of modern computers, this method

was deemed appropriate for a pre-manufacture analysis of a design or for final refinement of the design. An appropriate choice of magnetics model needs to be made for design optimization. An overview of possible choices of magnetics model of the machine is shown in Figure 6. Due to its generic nature (unlike MEC or analytical models), accuracy and use of computation resources, the multi-point magneto-static FEA model is adopted with certain modifications in this work.

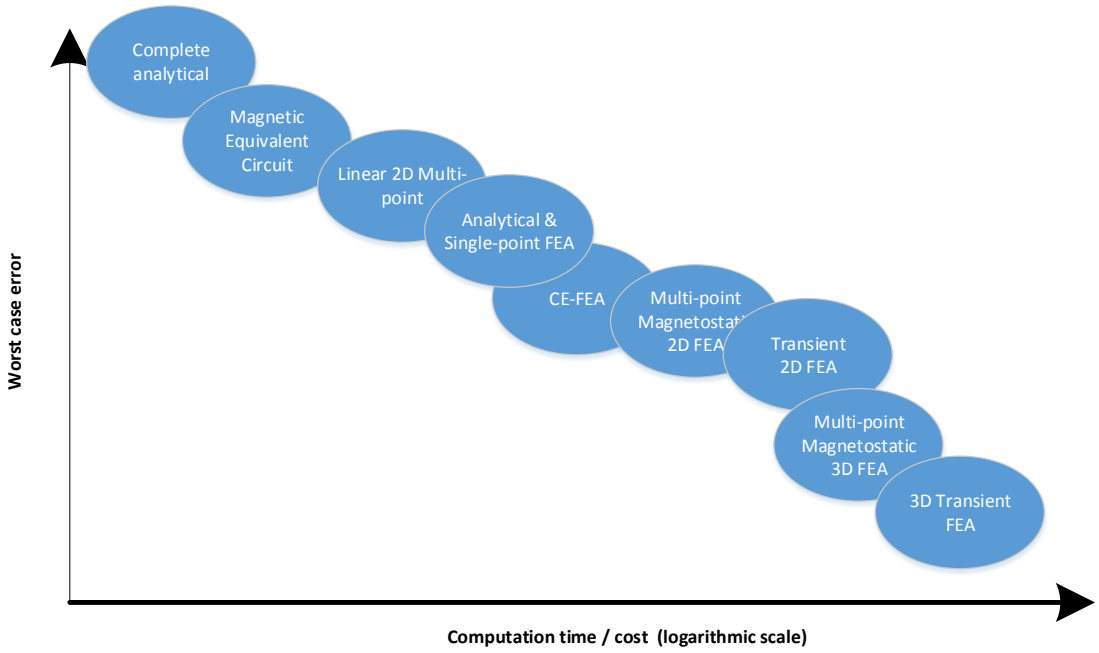

Figure 6 Choices for magnetics model of the electric machine

2.2. Stochastic optimization

The electric machine model is nonlinear, complex and often involves numerical methods for evaluation. Furthermore, evaluating the derivative with respect to design parameters may become overbearing if the number of design variables is large or it is undefined for discrete inputs. In such cases, gradient based search or grid search

becomes infeasible due to the complexity of the problem. Hence certain random, but smart search algorithms such as Genetic Algorithms (GA) [19], Differential Evolution (DE) [20], Controlled Random Search (CRS) [21] and Particle Swarm Optimization (PSO) [22] are employed. In stochastic optimization, a fitness function is a subroutine that returns objectives i.e. performance attributes of interest of a machine design for a set of input parameters. This dissertation aims at creating a unifying framework of essential modeling tools that can be interfaced with a stochastic optimization engine to optimize machine designs for a wide variety of problem definitions. Such a generic fitness function will set the stage for complete design automation in future.

The idea of employing stochastic optimization to electrical machines is not new [23, 24]. As in case of any design optimization problem, the problem statement should be defined by the designer that clearly states the input parameter vector $\boldsymbol{X}$, objectives $\boldsymbol{O(X)}$, equality constraints $\boldsymbol{h(X)}$, inequality constraints $\boldsymbol{g(X)}$ and bounds of parameters $\boldsymbol{X_l}$ and $\boldsymbol{X_h}$.

$$
\begin{array}{lll}
\text{Find} & \boldsymbol{X_i^*} & i = 1, 2...N; \\
\text{minimize/maximize} & \boldsymbol{O_m(X)} & m = 1, 2....M; \\
\text{subject to:} & & \\
 & \boldsymbol{h_k(X) = 0} & k = 1,2...K; \\
 & \boldsymbol{g_j(X) \leq 0} & j = 1, 2 \ldots J; \\
 & x_{li} \leq x_i \leq x_{hi} & i = 1, 2...N;
\end{array}
\tag{6}
$$

In case number of objectives is one (M=1), the optimizer returns one vector of parameters that maximizes/minimizes the objective function. If problem has more than one objective to optimize (M>1), the optimizer returns a non-dominated i.e. a Pareto optimal set of solutions. Multi-objective optimization allows the designer to understand the tradeoffs between different objectives and make selection based on this set rather than assign a weighing function without knowing the tradeoffs. Note than parameter bound limits are treated separately from inequality constraints because satisfying these does not need any function evaluation as they are easily satisfied by a linear mapping.

A very powerful feature of using population based search techniques is the flexibility to distribute computation [25]. Fitness evaluation of individuals in each population set is an independent computation and can be assigned to any computer on a network. This does not necessarily require a high throughput computing or grid computing environment. Also, the reliability of network and availability of nodes is not critical. This is demonstrated by the flowchart of Figure 7 that shows the implementation of a Genetic Algorithm based optimization server that is adopted for this work.

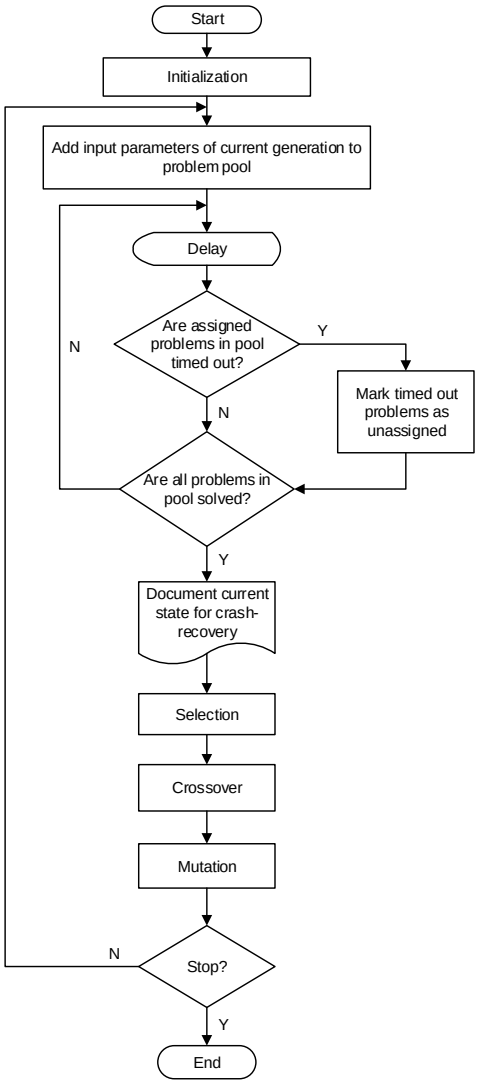

Figure 7 Flowchart of a Genetic Algorithm engine with distributed nodes evaluating individuals from a common shared location

2.3. Synchronous machine design using stochastic optimization

The idea of repeated computer runs for optimization of electrical machines dates back over 60 years [26]. In the context of modern computers and development of stochastic optimization methods, the use of GA's for optimization of electromagnetic devices was proposed by Uler *et al.* in 1994 [27]. Since then, this method has been

applied to several different design scenarios and has evolved in terms of methods and models adopted [28] as well as in terms of complexity of objectives of design [29]. An extensive literature review has been performed and a partial list of types of problem definitions previously studied is presented in Table 3. The objectives, constraints, input parameters and evaluation method adopted for each problem is listed in the table. In each of these cases, authors have developed a fitness function that is specific for solving the defined problem.

In one of the first applications of GA for optimization of an IPM [23], authors have coupled a MEC based model for maximizing efficiency for a fixed outer diameter 4-pole IPM. The calculations of equivalent circuit parameters are compensated (corrected) based on FEM for better accuracy. A similar efficiency optimization was performed for a case of outer-rotor topology for blower application [30].

An interesting study presenting different models and design problems formulated with different sets of objectives and constraints was published by Bianchi and Bolognani [24] (problems 2-4 in Table 3). Authors applied the technique to perform optimization for two different types of problems: in the first type of problem, the output was fixed and the objective was to minimize PM weight and in the second type of problem, the external dimensions of the machine were fixed and the output torque was maximized based on the thermal constraint. In the first problem, the authors employed MEC and FEM based models and exploited the linearity of electromagnetic torque with l_{stack} to achieve the desired torque in each case. Penalty functions were used for handling

inequality constraints. Later, a rotor optimization study was presented [31] to maximize torque capability while minimizing torque ripple for a fixed stator excitation.

Sudhoff *et al*. [1] expanded the scope of design optimization problem formulation (problem 8 of Table 3) by including almost all parameters that describe the machine geometry. This expanded the search space to span virtually all possibilities. This, coupled with a multi-objective GA ensured that a truly global pareto-optimal set was obtained. This also meant that convergence was far more difficult – the optimization needed a population of 5000 individuals over 500 generations to converge upon a dense and diverse two-objective pareto set. MEC based approach proved to be the correct choice for this scale of candidate designs as an FEA based approach would take prohibitively large computation effort.

Wrobel and Mellor [32] further advanced the process by incorporating thermal model of the machine for maximizing the torque capability for a casing-rotating motor (problem 9 of Table 3). This formulation also considered different slot-pole combinations and was aimed at development of a new winding construction for use in this type of motor topology.

For more complex geometric shapes of multi-barrier rotors, design studies were conducted by Pellegrino *et al.* [33-35] using FEA-based models. An important feature of these studies was the parametrization of three-layer rotor shape geometry that is most suited for achieving low torque ripple and high saliency ratio at the same time. A more complex design objective of achieving high CPSR was also studied in [33]. The different problem formulations (problems 10-13 of Table 3) were evaluated using more

computation resources e.g. the three objective optimization that employed multi-point FEA required 130 hours of computation time on a single Intel Centrino T7200 processor.

To solve the problem of rotor selection, without expanding the number of parameters needed to describe the geometry, a geometry morphing method was proposed to combine parametrization of the inset PM, V-shaped PM and spoke-PM rotor topologies[36].

A more computation intensive study was performed on a High Throughput Computation (HTC) environment [25] for weight optimization of SPM geometry to meet a fixed torque output. The fitness function used a transient FEA of each candidate design that required 25 hours to evaluate 4250 candidate designs that were generated by the optimization engine running on a population size of 85 over 50 generations against 29 days to run the same number of evaluations on a single computer node. Clearly, the compute time is lower for HTC, however, the reduction in time is not inversely proportional to the number of cores or population size due to under-utilization of resources. An important conclusion the authors have pointed out is the potential of HTC resources for combining electromagnetic, thermal and structural multi-physics analysis for design optimization.

Design optimization for field weakening operation presents a more complex optimization problem as the operating points may not be completely defined and may depend on the machine parameters itself. This type of design was studied by Parasiliti *et al.* in [29]. The base or rated speed of the machine is specified in the problem statement, whereas the top speed depends on the field weakening capability of the machine. The

three objectives of optimization are torque at rated speed, torque at maximum speed under field weakening and weight of the machine. For improved convergence, the authors combine the three objectives into one term to convert the problem to single objective and propose the use of modified version of CRS. This design problem formulation also uses virtually all design variables needed to describe the design (including current density indirectly by changing the number of conductors) and converges upon one design for a single objective optimization after evaluation of 13,000 candidate designs with a stopping criterion based on improvement over previous optimum design. The computational resources and time required is not mentioned.

A review of prior design optimization problems sheds light a rich variety of models, methods, approximations and problem formulations. Several design studies conducted in prior work demonstrates the ability of model based stochastic optimization to solve a variety of problems. As a next logical step toward design automation, we propose a framework that can weaves the web of common equations, methods and models underlying different types of synchronous machine design problems, an agile framework that can be expanded based on new models and methods and adapted to different design scenarios.

Table 3 Summary of selected machine design optimization problems studied in literature

	Ref.	Machine Type	Magnetics Model used	N_p, & spp	Design parameters	Objective(s)	Constraints & constraint handling
1	[23]	Inset block magnet inner rotor	MEC	N_p :4 spp: 1.5	Ns, Rro, Lax, Wbi, Hs2, MW, magnet fraction	η @ (T,ω_r)	Rso, current density†, fixed T@ $\omega_r > T_{rated}$, Flux density < B_{max} in teeth, back iron †
2	[24]	SPM inner rotor	MEC	N_p - 2-8 spp: 2-24	$l_{stack}/(2R_{si})$, $SW*N_s/(2\pi R_{si})$ H_{s2}/SW 3 Flux densities	Minimize PM weight	efficiency > 90% winding temperature < 80C g< function of R_{si}, l_{ax} constraint handling: penalty
3	[24]	SPM inner rotor	Static FEM	N_p = 8 spp = 2	Rsi, Hs2, TW, MW, magnet fraction	Minimize PM weight	T_{rated} > 200 Nm Winding temp < 105 C Minimum air-gap flux density > 0.4T† Rso l_{stack} calculated to satisfy first 2 constraints
4	[24]	SPM inner rotor	Static FEM	N_p = 8 spp = 2	Rsi, Hs2, TW, MW, magnet fraction	Maximize torque	R_{so}, l_{ax} fixed Winding temp < 105 C Minimum air-gap flux density > 0.4T†2
5	[30]	SPM, outer rotor	MEC	N_p :4 spp: 1	R_{si}, TW, S_{bi}, SO, MW, n_t	η @ (T,ω_r)	R_{so}, l_{ax} fixed T@ $\omega_r > T_{rated}$ Flux density < B_{max} in teeth, back iron †
6	[37]	Inset block magnet inner rotor	MEC	N_p :4 spp: 1.5	R_{ro}, l_{ax}, S_{bi}, H_{s2}, MW, magnet fraction, n_t	Weight, η @ (T,ω_r)	Phase current=constant, J<J_{max}†, Flux density < B_{max} in teeth, back iron †, T@ $\omega_r > T_{rated}$,
7	[31]	IPM trough barrier	Static FEM	N_p :4 spp: 2	5 rotor geometry parameters	Torque capability, torque ripple	Fixed stator geometry, Fixed current density

†constraints that may not be of actual interest to end-user, and in certain cases restrict the search space

Table 3 continued

8	[1]	SPM inner rotor	MEC	N_p :4 spp 1-4	17 geometry direct, material selection parameters	volume, copper loss for a fixed torque	$J<J_{max}$ †, Flux density < B_{max} in teeth, back iron†, T@ $\omega_r > T_{rated}$, fixed conduction loss Handled by penalty functions
9	[32]	SPM outer rotor	Static FEM	(Np,spp) (10,2/5) (14,2/7) (20/2/5) (28,2/7) (30,2/5) (42,2/7) (16,1/2)	MW, TW, R_{bi}, H_{s2}	Torque capability	Fixed R_{so}, l_{stack}, Current density fixed†, Limit: PM weight, slot area†
10	[33]	3 layer IPM rotor	FEA multi-point	N_p :4 spp: 2	6 geometric parameters needed to specify rotor geometry	Torque capability, torque ripple	Fixed stator geometry, V_{rms}, I_{rms}
11	[33]	3 layer IPM rotor	FEA multi-point	N_p :4 spp: 2	6 geometric parameters needed to specify rotor geometry	Torque capability, rotor loss	Fixed stator geometry, V_{rms}, I_{rms}
12	[33]	3 layer IPM rotor	FEA multi-point	N_p :4 spp: 2	6 geometric parameters needed to specify rotor geometry, PM remnant flux density	Torque capability, torque ripple, CPSR	Fixed stator geometry, V_{rms}, I_{rms}
13	[33]	3 layer IPM rotor	FEA multi-point	N_p :4 spp: 2	6 geometric parameters needed to specify rotor geometry	torque, ripple, rotorloss	Fixed stator geometry, V_{rms}, I_{rms}
14	[38]	Wound rotor	MEC	N_p :4 spp: 2	15 geometric paramaeters (some direct, some transformed)	Weight, loss	T@ $\omega_r > T_{rated}$, fixed current density† Vl-l < Vdc

Table 3 continued

15	[36]	Spoke, V-magnets, flat-inset	CE-FEA	N_p:10 spp: 2/5	6 geometric parameters needed to specify rotor geometry inset and spoke type, 9 for V-shaped	Material cost, loss, torque ripple	Stator fixed, T@ ω_r fixed
16	[25]	SPM	Transient FEA	N_p:10, spp:2/5	R_{si}/R_{so}, 6 encoded parameters internal to stator and rotor	Weight	R_{so} fixed, J_z fixed†
17	[39]	V-magnets	CE-FEA	N_p:10, spp:2/5	R_{si}/R_{so}, 8 encoded parameters internal to stator and rotor	Efficiency at rated, Material cost	R_{so} fixed, J_z fixed† Torque ripple < 5% Back-emf THD < 3%
18	[29]	U-shaped single layer IPM	Magneto-static FEA	N_p:6 spp:36	18 geometric variables (stator and rotor)	Torque at rated, torque under field weakening and weight combined into one objective	Fixed I_{ph} Flux density < B_{max} in teeth, back iron † bemf < V_{dc}, η_{rated}>90% $\omega_{r,max}$> $\omega^*_{r,max}$
19	[29]	U-shaped double layer IPM	Magneto-static FEA	N_p:4 spp:2	16 geometric variables (stator and rotor)	Torque at rated, torque under field weakening and weight combined into one objective	Fixed I_{ph} Fixed R_{so} Flux density < B_{max} in teeth, back iron † bemf < V_{dc}, η_{rated}>90% $\omega_{r,max}$> $\omega^*_{r,max}$

3. THE PROPOSED FRAMEWORK

3.1. Introduction

The proposed framework is an object oriented fitness evaluation class that is equipped with necessary interfaced models and methods that can be employed to predict performance of an electrical machine. Specifically, the class is organized in an abstraction that can be adapted to solve for the fitness of an individual for a wide variety of electrical machine design problems defined within the scope of the black-box approach and can be interfaced with the optimization engine. The overview of the framework is shown in Figure 8. The different components of the framework are discussed in sections 3.4 to 3.6.

At the optimization engine level, each design problem is characterized by its parameter space, parameter encoding scheme, constraints and objectives. For evaluating an individual design, we need the corresponding decoding scheme and evaluation algorithm specific to the problem. The decoding function is implemented at the fitness evaluation level and the solution algorithm is implemented at the machine class level as shown. Section 3.8 of this chapter is dedicated to evaluation algorithms for improvement of convergence characteristics of the optimizer by minimizing the number of independent design variables. Specifically, the variables current density, stack length and/or operating speed (wherever applicable) are exploited to eliminate equality constraints or meet design objectives. This is demonstrated by categorizing and listing design problems and developing solutions for some of them.

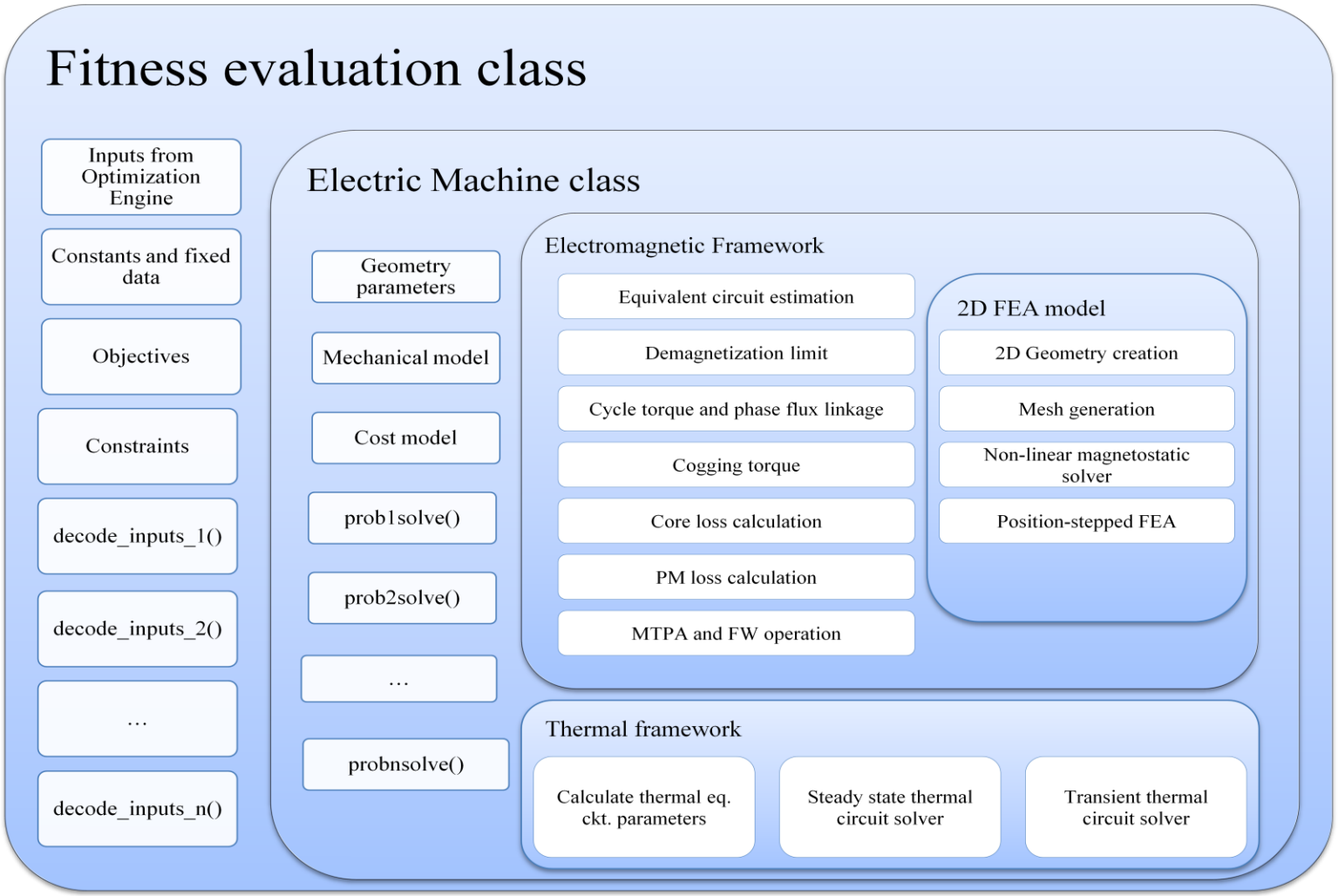

Figure 8 The fitness evaluation class

3.2. Categorization of design problems

One of the important objectives of this research is to show how the proposed framework can be used to solve a wide variety of design optimization problems that the user may define. The black-box approach followed defined AoI's that an end-user may be interested in. Some of these AoI's are related to the geometry of the machine while other can be categorized as performance metrics of the machine. The description of a machine design is complete when all its geometric parameters, current (assuming optimal control), and speed are defined for all operating conditions. The final evaluation of objectives for an individual gene is possible only after the full definition of the machine is complete. Parameters that describe the machine (column 1 of Table 4) if not specified directly by the user may be derived in different ways categorized as:

a) "free design parameters" that are calculated from the gene
b) fixed as a design choice at the beginning of optimization
c) calculated inside the fitness function to meet certain design criteria specified by user (this means they are indirectly specified by the user)

Thus, on one hand the user may specify the requirement in numerous different ways based on AoI's while on the other the definition of electric machine needs to be complete. A problem defined by the end user may fall in one of the three categories discussed in the next three subsections.

Table 4 Sources of parameters that describe the machine

Category of parameters:	Parameters fixed at the beginning of optimization	May be specified by user	Generated by optimizer	Calculated to meet constraints/ optimize objectives
Material selection	√			
Rotor geometry type	√	√		
Winding construction	√	√		
Slot fill	√	√	√	
Operating speed		√		√
Outer diameter		√	√	
Inner diameter		√	√	√
Stack length		√		√
Slot-pole combination			√	
Split ratio (R_{ro}/R_{so})			√	
Slot geometry parameters			√	
Rotor internal geometry parameters			√	
Conductor current density			√	√
Conductor insulation class	√	√		
Cooling method	√	√		
Skew (stator or rotor)			√	

Before proceeding to classification on design problems, it should be emphasized that all problems implicitly impose a thermal limit on operating temperature of the windings. It is assumed that this condition is implied and not mentioned explicitly in problem definitions. Additionally, black-box parameters of external dimensions, cost, weight, operating point, efficiency and CPSR are considered for categorization. Other AoI's are calculated during the evaluation process and the pareto-set that meets constraints based on these or optimizes objectives based on these relies more on the optimization engine for convergence.

3.2.1. Category 1: known operating points

For a problem that belongs to this category, the user is interested in operation of the motor at certain operating conditions specified in terms of torque, speed and output power. In order to limit the size of the design for this category of problem, it is assumed that minimizing at least one attribute out of volume, weight or cost is an objective. In case the user has not specified any such objective, minimizing weight is considered as the default objective. A (non-exhaustive) list of such problems is presented here:

1) Motor should be capable of producing torque T_{out} at speed ω_r for continuous operation. Maximize $\eta(T_{out}, \omega_r)$
2) Motor should be capable of producing torque T_{out} at speed ω_r for continuous operation such that $\eta(T_{out}, \omega_r)>\eta^*$
3) Motor should be capable of producing torque T_{out} at speed ω_r for continuous operation. $\eta(T_{out}, \omega_r)$ is neither objective nor constraint.

4) Motor should be capable of producing torque $T_{out,i}$ at speed ω_{ri} for times t_i ($t_i=\infty$ means continuous operation) and $i = 1,2,3....$
5) Should be able to operate over a cycle with period t_{cyc} and a $T_{out}(t)$ and $\omega_r(t)$ profile
6) Cases 4 or 5 with inverter VA as an objective (i.e. employs field weakening)
7) Maximize ω_r such that efficiency $\eta > \eta^*$ under continuous operation at (T_{out}, ω_r)
8) Should be capable of producing power P_i at speed $x_i\omega_r$ for times t_i where base speed ω_r is unspecified and is a design variable and $i = 1,2,3...$
9) Should be capable of producing power P_i at $x_i\omega_r$ with $\eta_i > \eta_i^*$ for time t_i where base speed ω_r is unspecified and $i = 1,2,3...$
10) Maximize CPSR for output power P^*
11) Maximize CPSR for output power P^* such that $\eta > \eta^*$ at maximum speed of operation

3.2.2. Category 2: fixed volume/weight/cost

In this category, the user specifies only one of volume, weight or cost of the machine. The aim of optimization is to maximize the capability of the machine under such a constraint. Optionally, the user may specify the outer radius, in which case the volume, weight or cost constraint is met by adjusting the stack length. In the other case, the outer radius is a design parameter and the model adjusts the stack length in the same way to meet the volume, weight or cost constraint. There may be further six subcategories in terms of the objective

1) Maximize Torque capability (continuous or short duty) at fixed speed

2) Maximize Torque (continuous or short duty) at fixed speed with efficiency constraint
3) Maximize power (speed is unspecified)
4) Maximize power (speed unspecified) with efficiency constraint
5) Maximize power (speed unspecified) with CPSR constraint
6) Maximize power (speed unspecified) with efficiency and CPSR constraint

3.2.3. Category 3: fixed volume/weight/cost and known operating point

This category includes all the problems of category 1 with additional constraint on volume, weight or cost. If the operating condition (torque and speed for motor or speed and output power for generator) is specified, then the only free variable to achieve the operating condition is current density.

3.3. Design choices and assumptions

The optimization problem formulation process begins with making certain design choices. Some of the design choices can be made either by the user or may be relegated as a design parameter to the GA. In the current form of implementation, it is assumed that the user makes these choices. In order to create a meaningful optimization problem and ensure that only valid and feasible designs are created by the optimizer, the following design choices and inputs need to be specified:

1) Material selection: The three materials used in the active part of the machine: lamination steel, conductor material, and PM material (for PMSM) need to be decided

2) Winding construction (random-wound, form-wound or bar conductor): This is a very important consideration that has direct influence on the slot-fill and hence efficiency, weight, volume, and cost of the machine. More importantly, it affects the labor cost and is also dependent on the type of automation available for manufacturing. In addition to this, the insulation class of winding should also be decided.
3) Rotor geometry type: Different example rotor geometries for four-pole rotors were presented in Figure 2. Depending on the pole-count, PM material and whether field-weakening is used, an appropriate choice of rotor geometry needs to be made at the beginning of the design process. Since the GA performs a geometric optimization, the set of minimum parameters "internal" to each rotor geometry (refer Table 4 for definition) is different. Hence, only one geometry is considered for each run of optimization. An attempt to "morph" different rotor geometries was made by Zhang *et al*. in [36]. However, this approach is not universal and may not be readily extended to multiple layers and bridge configurations and is not considered for this study.
4) Slot-pole combinations: Slot-pole combination and winding slot pitch are important design parameters that influence winding pattern, and winding labor cost. The slot per pole per phase (spp) of a three phase machine is given by,

$$spp = \frac{N_s}{N_p N_{ph}} = a + \frac{b}{c} \tag{7}$$

where a is the integral part and b/c is the fractional part (b and c have no common factor). It can be deduced that if a=0, the winding pitch will be one or two slots. The

one slot-pitch combination $\left(\frac{b}{c} < 0.5\right)$ would result in a non-overlapping winding. For a ≠ 0, and b = 0, it is an integral slot distributed winding (ISDW) and for a >1 and b ≠ 0, it is called a fractional slot concentrated winding (FSDW). ISDW combinations are characterized by high winding factor, however, suffer from high cogging torque and torque ripple. For these windings, a wave winding construction can be adopted that minimizes the number of end-connections. FSCW and FSDW windings show lesser cogging torque and torque ripple but lower winding factor as compared to ISDW and usually need larger number of coil-interconnects. If the design requirement specifies constraints on cogging torque or torque pulsations, ISDW designs can be used in conjunction with rotor or stator skew to mitigate these effects. Pole-slot combinations are encoded as a discrete input parameter of the GA. The choice of what type of combinations to include needs to be made in order to define the optimization problem. By default, all combinations are chosen.

5) Skew type: If cogging torque or torque ripple is a constraint or design objective, ripple can be minimized for certain slot-pole combinations $\left(\frac{b}{c} = 0 \; or \; 0.5\right)$ by introducing stator or rotor skew. This may have implications on the manufacturing process and cost. The type of skew needs to be specified in the beginning of design process.
6) Voltage rating and coil connections: Each slot-pole configuration has a fundamental periodicity associated with it, which is given by the greatest common divisor (gcd) of N_p and N_s for double layer windings and needs to be calculated for single layer windings from its winding function. For instance, 10-slot 12-pole (gcd=2) single

layer winding is twice periodic with one half opposite in polarity to the other whereas the winding pattern 20-pole 18 slot (also gcd=2) single layer configuration does not repeat its pattern. Lap-wound coils in stator can be connected in series or parallel. A double layer lap-wound stator can have *p* parallel connections where *p* is a factor of *gcd* (N_p, N_s). For instance, a 10-pole 60-slot configuration may have all coils in series *(p=1)*, or *2*, *5*, or *10* parallel paths. Let us define a new term called "fundamental voltage" $V_{fundamental}$ which is the line voltage at the terminals of the motor if all coils were connected in parallel with only 1 turn per coil. This voltage is characteristic of the choice of design. By having more turns or different number of parallel paths, the line voltage of the motor can be adjusted to:

$$V_{ll} = n_t \cdot \frac{\gcd\,(N_p, N_s)}{p} \cdot V_{fundamental} \tag{8}$$

where n_t is the number of turns per coil. Thus, a voltage rating that is any integer multiple of $V_{fundamental}$ can be achieved by proper choice of turns and parallel paths. For instances where it can be realized by different choice of connections, the best choice is one that minimizes the number of winding operations or one that minimizes the phase resistance. The choice of end connections is not given consideration for evaluation of fitness function and is left as a "post-design" decision.

7) Implied thermal constraint: It is assumed that any design produced by the optimizer should not violate the condition that winding temperature under worst case scenario does not exceed its insulation class temperature.

8) Manufacturability: If the user narrows down on any design in the optimal set, she should be able to practically build the machine to that specification. This imposes constraints on these aspects:
    a) Air-gap width should not be too small for the expected geometric tolerance stack-up
    b) The lamination geometry should not have any sharp angles that are difficult to punch or cut. The minimum fillet radius should be at least 0.5 mm.
    c) The width of bridges and center posts should greater than the chosen lamination thickness
    d) Barriers designed for buried magnets should be wider than the maximum expected tolerance for PM thickness
    e) PM thickness should not be less than what can be manufactured. Special consideration needs to be given for thinner PMs as the best magnetic properties of the material are not guaranteed [40] for smaller dimensions e.g. less than 3 mm thickness for hard ferrites.
9) Cooling method and ambient conditions: Depending on the rating and operating environment, the type of cooling needs to be decided. Standard cooling methods are: naturally cooled, shaft coupled fan cooled, external forced cooled, liquid cooling jacket, etc. For each condition the coolant temperature (ambient temperature for air-cooled), flow rate and control type (for external active controlled) should be specified. For air-cooled, construction of fin profile is needed for calculating heat exchange coefficients.

10) Casing and frame construction: The frame selection of the desired machine depends on the working environment. Common types of frames are open, closed, sealed, etc. In certain cases, the machine is a part of another system e.g. a hybrid vehicle drive-train. In such cases, a separate frame is not required. Frame information is required to calculate the overall weight and cost of the machine. This aspect is considered out of scope of the context of this research, but may be desirable for practical motor design.

3.4. Thermal framework and model

Thermal design and electromagnetic design of the electric machine are highly inter-dependent. Losses in the machine are dependent on temperature distribution inside the machine and vice versa. Material properties that are altered with temperature are:

1) Demagnetization curve of the permanent magnets
2) Resistivity of conducting material
3) Viscosity of medium inside the motor
4) Heat exchange coefficients of the coolant itself

Hence temperature distribution of the machine has an influence on all AoI's of the machine. Another consideration that is even more important is that winding insulation of the machine should not exceed its rating during the worst case operating condition of the machine. Depending on the excess temperature rise above rated winding insulation temperature, the machine may either experience a catastrophic failure due to short circuited stator windings or reduced insulation life. Hence thermal design should be integrated into the design process for accurately predicting machine performance.

While this aspect is important, it should be kept in mind that performance is not "highly sensitive" to temperature. For example, the resistivity of copper increases 0.39%/°C rise in temperature and the coercivity of a typical NdFeB grade decreases 0.12%°C rise in temperature. For the purpose of design, a temperature estimate within 2-5°C accuracy is considered acceptable.

The temperature distribution inside the machine is modeled using two basic approaches: the lumped parameter approach and numerical methods involving computational fluid dynamics and 3-dimensional thermal FEA. Heat exchange inside the machine and from machine to environment occurs due to conduction, convection, and radiation. Heat transfer due to conduction can be studied accurately with 3D thermal FEA. Radiation heat transfer calculations depend on the emissivity of the surface and the angle of view. These physical quantities are readily available and can be included easily into the model. Convective heat transfer requires fluid flow analysis and needs prohibitively large computation time. It may still involve the use of empirical relations for estimating heat exchange coefficients and exhibit some level of inaccuracy when extending it for different designs.

3.4.1. Lumped parameter thermal model of the machine

The lumped parameter model assumes constant temperature distribution within each component with high thermal conductivity. Such a component is represented as thermal capacitance, conduction paths between components with relatively larger temperature drops are represented as thermal resistances and losses in the machine are

represented as current sources in the thermal equivalent circuit. A typical thermal circuit for an outer-rotor machine (studied later in chapter 4) is shown in Figure 9.

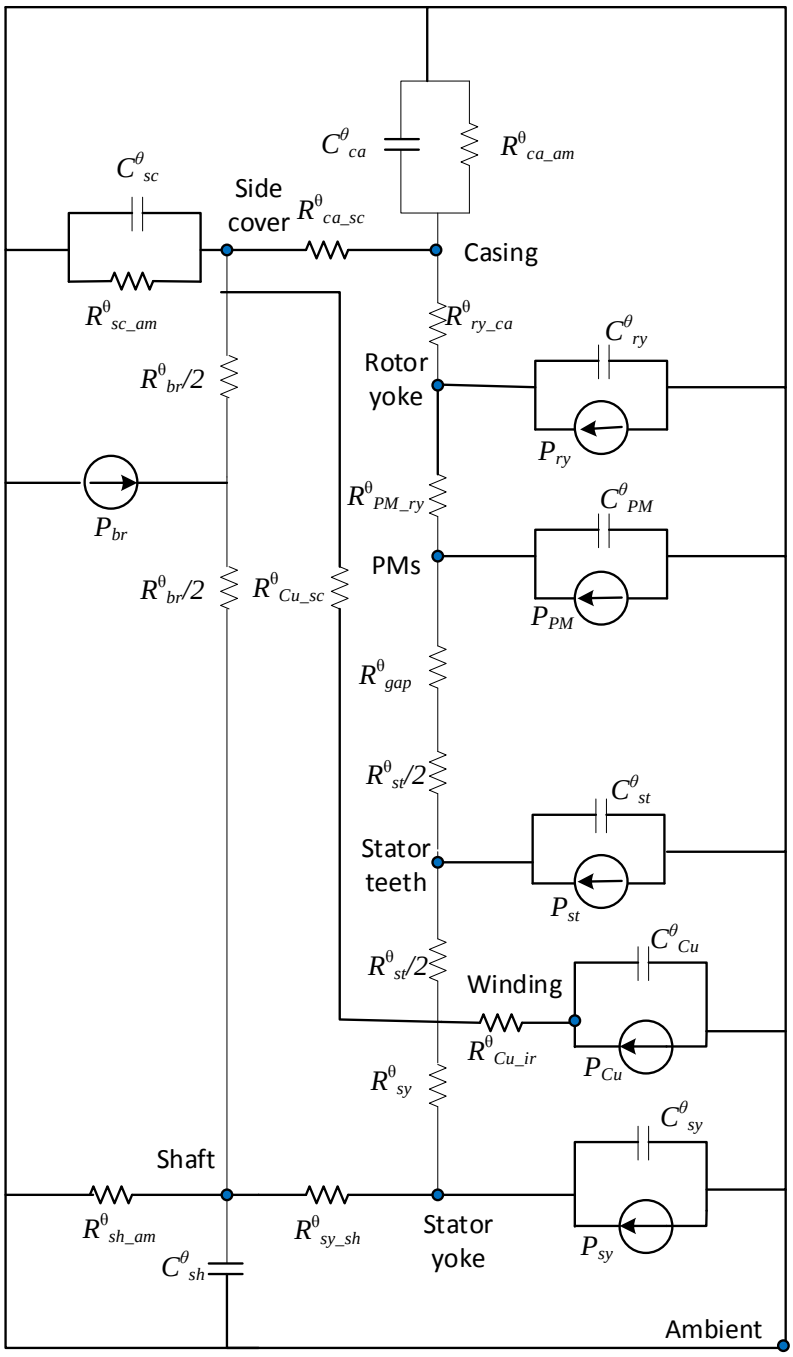

Figure 9 Lumped parameter thermal equivalent circuit of an outer-rotor SPM

In Figure 9, each lumped node is denoted by a capacitor C^{θ}, each loss source is denoted by a current source with letter P and lumped thermal resistance is denoted by R^{θ}. Subscripts of each symbol are as follows: Cu – copper, ir – lamination, sy – stator yoke, st – stator teeth, gap – air-gap, br – bearing, sh – shaft, ca – casing, sc – side cover, PM – permanent magnet, am – ambient, ry – rotor yoke. This lumped thermal circuit may be based on thermal impedances derived from physical construction of the machine or an approximation of the "minimum" number of nodes in order to calculate key component temperatures with sufficient accuracy.

The accuracy of this method depends on precise calculation of thermal resistances of key heat transfer paths. The approach followed for calculating different types of thermal resistances is described here:

1) Contact resistances: Thermal contact resistance between two metal components is modeled as an interface airgap. The interface gap depends on factors such as surface roughness and type of fit between the components. Typical values of such gaps between metals are given in [41]. However, the surface roughness of laminated steel stack needs special consideration. The effective interface gap is assumed based on experimental data reported in literature [42].
2) Convective heat transfer: Heat transfer from casing/housing to external cooling medium and from windings to casing takes place due to convection. The external flow rate will depend on the type of cooling method used: natural convection, force convection coupled to the shaft or externally

controlled flow rate. In each case, the velocity profile of the flow along the periphery of the casing needs to be estimated in order to calculate the effective heat transfer coefficient. Empirical dimensionless convective heat transfer correlations are used for estimation of this thermal resistance. Coefficient of convective heat transfer between end-winding to side casing is experimentally found to be (8) [43]:

$$h_c = 41.4 + 6.22 v_{air} \quad (9)$$

3) Air-gap heat transfer: Heat transfer in air-gap depends on the relative surface speeds between the rotor and stator surfaces, air-gap width and the smoothness of the rotor and stator. This is studied extensively in [44]. It is concluded based on dimensionless analysis that air-gap heat transfer is due to conduction only at low surface speeds when flow in air-gap is laminar. For a medium speed range, when the flow assumes a vortex form, heat transfer is enhanced. The heat transfer rate is maximum for turbulent flow. Heat transfer coefficients are calculated from empirical formulas derived based on dimensionless convection correlations.
4) Conductor to stator core thermal resistance: Conductors are separated from stator core with wire insulation, slot impregnation, and slot liner as depicted in Figure 10. The slot is filled with thermally conducting resin to establish good thermal contact. However, in practical motors, the resin does not completely penetrate the slot and leaves air-bubbles and voids reducing the impregnation fill. Typically, an impregnation fill of 0.4 to 0.5 is observed for

dip impregnation process. The thermal resistance for one slot is computed by means of a thermal FEA as shown in Figure 10.

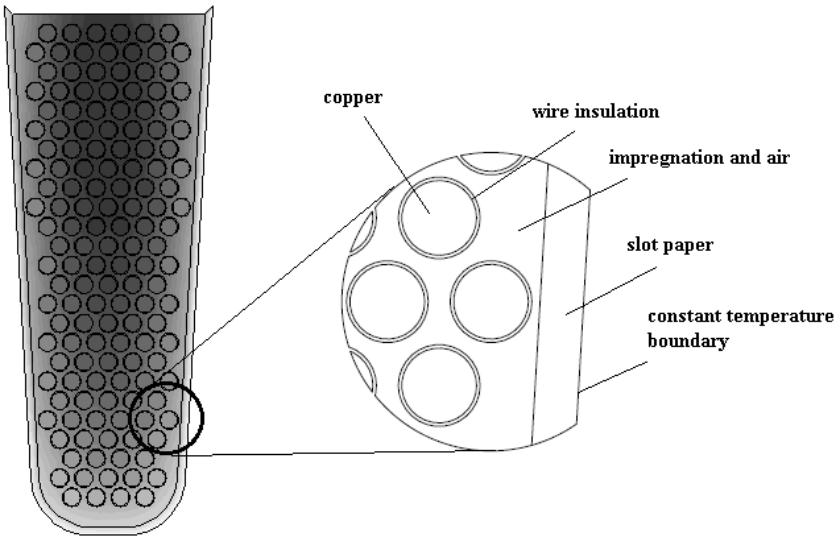

Figure 10 Thermal FEA model to compute effective thermal resistance between copper and stator core

3.4.2. Practical considerations in modeling thermal resistances

The modeling technique used to determine elements of the lumped parameter model depends on experimental data gathered over the years [45]. It is observed that the data in different experiments is not consistent. This is expected because the contact resistances are sensitive to manufacturing process and the flow distribution is sensitive to the size of the machine and flow field around the machine during testing. Therefore, any modeling technique is not guaranteed to achieve an accurate thermal model without calibration. The model needs to be calibrated using a test machine of a very close to

expected geometry of the final optimum. From a thermal analysis perspective, the operating duty of the machine can be specified for three types of operation, discussed next.

3.4.3. Thermal steady-state operating condition

A machine rated for steady state operation is said to reach its steady state when it reaches a stable thermal operating condition. Some machines require operating in continuously repeating drive cycle with no cool down where the machine reaches a thermal steady state. This definition of steady state operation allows for small temperature fluctuations in each component during each drive cycle in thermal steady state such that loss calculation of the electromagnetic model is not significantly altered. Constant torque operation at a constant speed is a special case of this type of operation which will not see this fluctuation. For determining the steady state performance of a machine under this condition, the capacitances of the thermal equivalent circuit can be neglected. The losses and temperature distribution are inter-dependent and need to be calculated iteratively to find the thermal equilibrium state. This is achieved by adopting an algorithm as shown in Figure 11.

3.4.4. Short duty rating transient thermal model

A machine rated for short duty high torque is subjected to relatively very high current densities in stator (2-6 times as that of a similarly sized steady state operation machine, and hence 4 to 36 times the loss). This leads to rapid temperature rise in windings. In short-time duty operation the machine operates over a torque and speed profile and is allowed to cool down to ambient temperature before the next cycle. This

case is analyzed by means of a transient thermal-electromagnetic time domain response of the lumped parameter thermal circuit similar to one shown in Figure 9. Unlike the steady state operation, this process is an actual time stepped response of thermal circuit to the power loss under overload. It should be noted that the loss during this transient is not constant and should be updated based on conductor temperature at each time step.

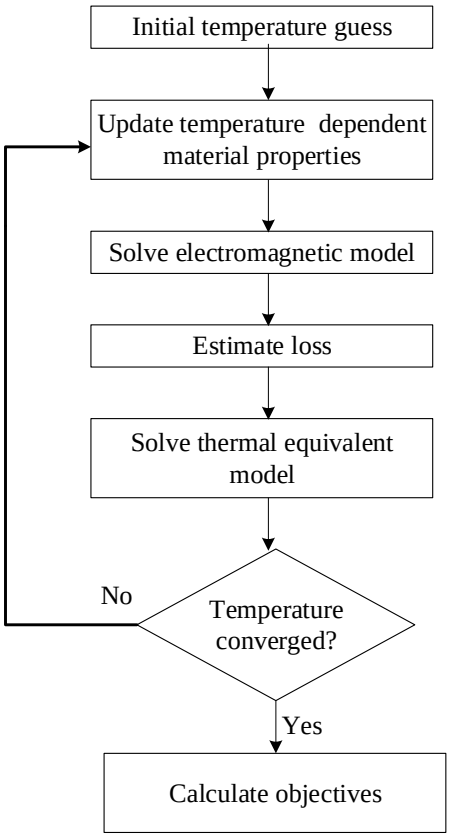

Figure 11 Thermal outer loop that iteratively estimates the steady state operating temperature distribution of the machine

3.4.5. Continuously repeating drive cycle with intermittent cool down period

This mode of operation is characterized by low power operation or cool-down and intermittent overload. During the low power or cool-down period, the machine tends

to reach a stable thermal state. However, the short-duty overload occurs before reaching a steady temperature and rapidly heats up the machine. A machine that operates in such a fashion may have an active cooling system that controls the coolant flow depending on the temperature. For such a case, the transient model needs to be solved for a longer duration till the repeating thermal cycle of the machine is established.

3.5. Components of the 2D-FEA based electromagnetic model

The multi-point static FEA approach is adopted in this work. The finite element magnetic model uses the FEMM [46] package along with a library of additional functions to customize for analysis of electrical machines. The elements of the FEA based model are described here.

3.5.1. Geometry creation, mesh generation and mesh transformation

Geometry creation is the first step for harnessing FEA for modeling magnetic aspects of the machine. The geometry creation module consists of a library of rotor and stator geometry creation scripts. The input geometric parameters are converted into FE entities of nodes, lines, curves, regions that define the solution domain. The axis periodicity of the domain is found from the winding function of the selected pole-slot combination and winding layers. The domain is sliced to the minimum possible "pie" based on its periodicity. Appropriate periodic or anti-periodic boundary conditions are chosen.

The domain is meshed using the 'Triangle' package [47]. The mesh generator uses a random triangulation for meshing. If the rotor is rotated to its next position for a position stepped analysis, the air-gap needs to be re-meshed. If the entire geometry is re-

meshed, the new mesh will be different from the original. This creates a difficulty for accurate computation of core losses. The air-gap is split into three layers. For position stepped FEA, only the middle layer of the air-gap is re-meshed while retaining the mesh of the stator and rotor. This new mesh is then "stitched" with the existing stator and the rotated rotor mesh.

3.5.2. 2D Fast nonlinear magneto-static FE solver

The basic theory and methods used in solution of non-linear magneto-static FEA were discussed in section 2.1. In the context of the fitness function framework, the description of this method is presented here.

The direct implementation starts from a guess of zero magnetic potential A_z at all nodes in the mesh. However, it was observed that if an initial guess of A_z is made from a previous solved step, it significantly reduces the time for convergence of the non-linear magnetic field solver. Thus the initial guess of permeabilities of elements from a previous step leads to faster convergence.

As an example, this is implemented in a fitness function of a machine with 2D geometry with 11352 mesh elements as show in Figure 12. The solution time per step is 5.97 s with initialization at zero. Now the closeness of the solution increases if initialization is done from a previous step and is even closer if the previous step is not very different in terms of rotation or excitation. It was observed that the computation time was reduced to 2.72 s for a step size of 6° electrical and to 2.03 s for a rotation of 1.875° electrical. Thus the computational cost does not increase in proportion to the number of steps computed. This is shown in Figure 13 for the example case.

As described in the previous subsection, performance evaluation needs to be repeated for a design if material properties are updated due to change in temperature. In this case, the previous position stepped series of magnetostatic solutions are even "closer" because of the small change in properties. It was observed that the computation time was reduced to 1.16 s from 2.72 s for the 6° rotation per step case.

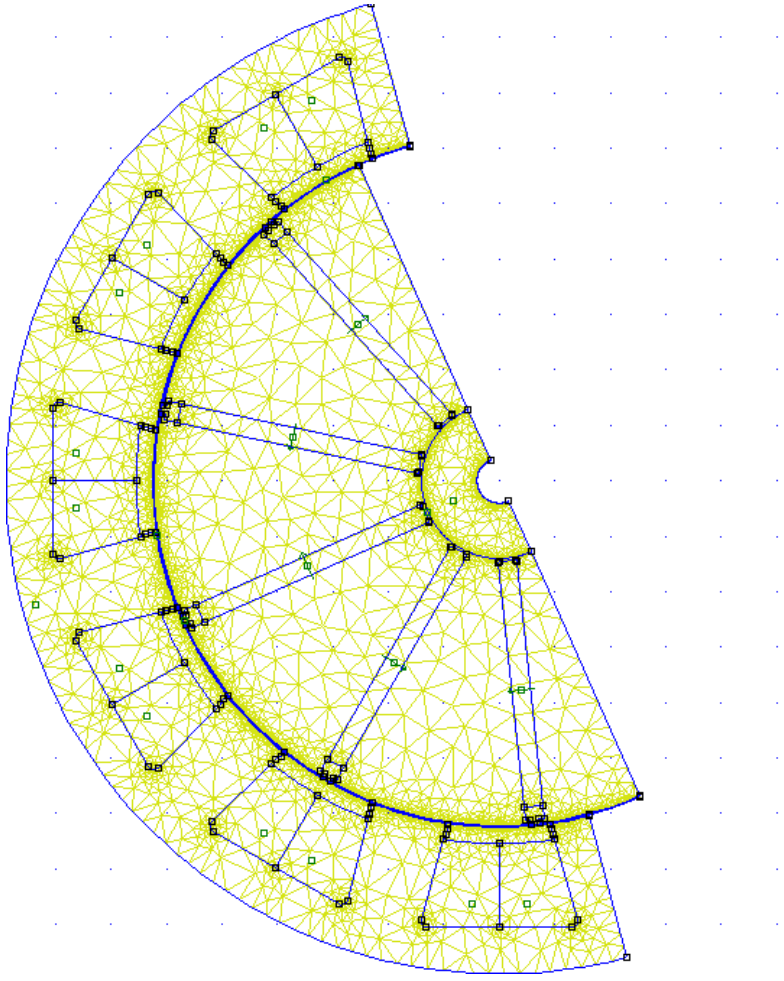

Figure 12 A finite element mesh with 11352 elements

This strategy has a significant impact on the time taken for fitness evaluation because the nonlinear magnetostatic solution is the most time consuming step in the

process. For the example considered here, fitness evaluation involved 72 magnetostatic solutions. The overall time was reduced to less than half as shown in Figure 14.

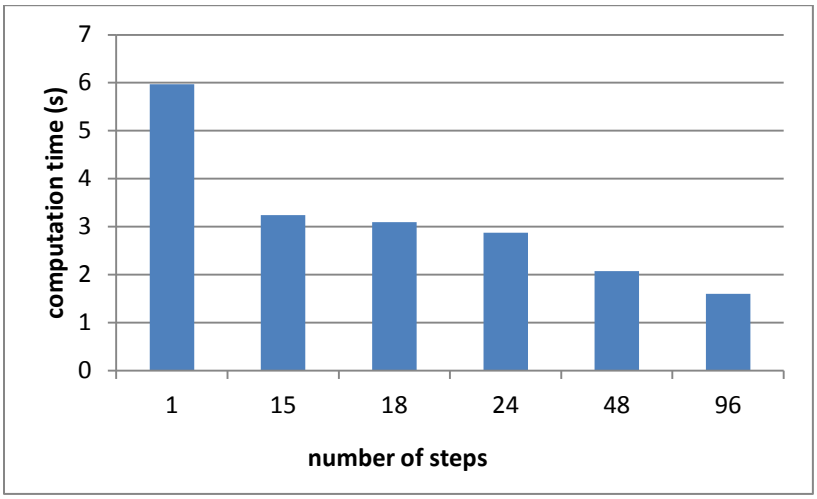

Figure 13 Computation time per step reduces if the previous step is closer to the current step (for different number of steps of a 180° electrical angle rotation)

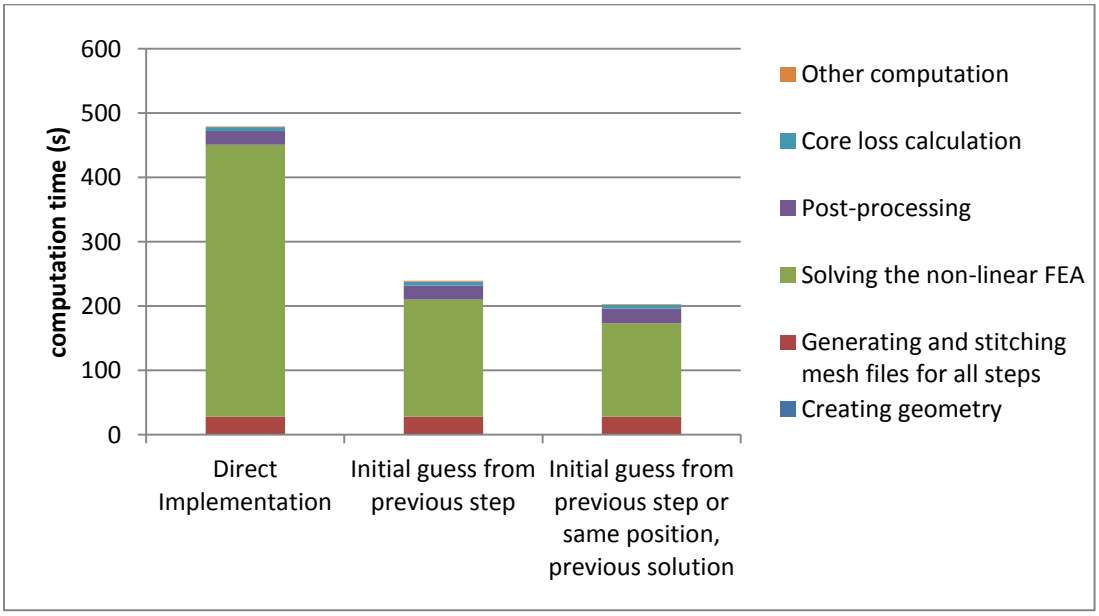

Figure 14 Reduction in overall fitness evaluation time involving 72 magnetostatic solutions (18 position steps repeated 4 times by changing current excitation/material properties based on temperature)

3.5.3. Position stepped FEA

This subroutine constitutes a building block for several different subroutines explained further in this text. The inputs to this block are:

Inputs:

a) Reference rotor position
b) Initial rotor position
c) Current density to be applied
d) Angle of rotation
e) Step size of rotation

Outputs:

a) Torque as a function of rotor position
b) Phase flux linkages as a function of rotor position
c) x- and y components of magnetic field intensity for each element of the mesh

The rotor position is stepped from initial to final and magneto-static FEA is performed at each step. The subroutine assumes that the stator and rotor geometry is already meshed, and only meshes the air-gap at each step and integrates it with the rest of the mesh. The A_z data of the solution at each time step is used to compute the outputs of this function:

The A_z data at each step is not discarded as it can be used as an initial guess for the next position step for faster convergence. This has a huge impact on the convergence time. Though computation at different rotor positions is parallelizable, due to the

different convergence time of each step, and to use only one core of the processor for each fitness function, only one instance of the solver is used. Note that this step resembles the conventional time-stepped FEA, except that current distribution in conductors is not updated based on rate of change of magnetic field. This eliminates the need of a small time step for accuracy and hence time step size is chosen based on the resolution or harmonics needed in computation of torque, flux and core loss.

3.6. Electromagnetic framework: analytical relations and algorithms

This section briefly describes the analytical models and algorithms adopted to calculate physical parameters in intermediate steps of the fitness function evaluation. The inputs for the fitness function (which are design parameters for the optimization) are defined in such a manner that decisions related to stack length, current density, series and parallel connections of coils can be taken at a later stage of the design phase in order to meet certain design requirements. To allow the design process to scale stack length, most results are derived for unit length of the geometry. Also, to allow maximum granularity on the terminal voltage, analysis is done assuming all coils in parallel with single turn per coil. The parameters derived under this definition are termed as motor's "fundamental" parameters. It will be shown in 3.5.8 that none of the MTPA or field weakening calculations is affected by this model.

3.6.1. Computing key lumped circuit parameters

Inputs:

a) Maximum expected current density

b) Stator skew

c) Rotor skew steps and step angles

d) Reference rotor position

Outputs:

a) Fundamental phase flux linkage λ_{M_2D} per unit length of stack

b) Fundamental d- and q- axis inductances for unit length of stack as a function of current density: $L_{d\_2D}(J_{z,d}), L_{q\_2D}(J_{z,q})$

The two-axes lumped equivalent electrical circuit of the synchronous machine (without a cage) can be described by a set of four parameters: r_{ph}, λ_M, $L_d(i_d)$, $L_q(i_q)$. These parameters are useful in calculating the MTPA, field weakening mode operation, power factor, etc. In certain cases, preliminary designs can be evaluated using only lumped parameters instead of performing a full analysis for all designs. These parameters can also be used for discarding designs that lead to poor performance and full analysis of such "bad" designs is avoided and only an approximate value of the objectives is returned.

This subsection presents the method adopted for computing λ_M, L_d, L_q by means of magneto-static FEA solutions. It is observed that harmonic effects in integer spp machines lead to inaccuracies if a single static FEA is used for evaluating and different methods with certain analytical calculations need to be adopted for the cases of integer spp, non-integer (fractional) spp, skewed stator and stepped rotor skewed motors.

Equivalent circuit parameters for non-skewed motors

FEA solution is found by applying zero excitation in the windings for a known electrical rotor position. The fluxes associated with the three phases are used to compute

λ_M. This operation may be performed at a stage in the algorithm when the number of turns or stack length is not known. Hence flux linkage for unit length of machine for the symmetric slice is calculated assuming that each coil is wound using a single turn. The effect of increasing the number of turns will be incorporated in the design process separately. This flux linkage is denoted by the symbol λ_{M_2D}

$$\lambda^1_{qs0} = \frac{2}{3}\left(\lambda^1_{as0} - \frac{\lambda^1_{bs0}}{2} - \frac{\lambda^1_{cs0}}{2}\right) \tag{9}$$

$$\lambda^1_{ds0} = \frac{1}{\sqrt{3}}\left(\lambda^1_{bs0} - \lambda^1_{cs0}\right) \tag{10}$$

$$\lambda^1_{qds0} = \lambda^1_{qs0} - j \cdot \lambda^1_{ds0} \tag{11}$$

$$\lambda^1_{qdr0} = \lambda^1_{qds0} e^{-j\theta_e} \tag{12}$$

$$\lambda_{M\_2D} = -\mathrm{imag}(\lambda^1_{qdr0}) \tag{13}$$

For the transforms given in equations (9)-(13) above, a pure sine winding and a sinusoidal air-gap flux density or one with a very low winding factor for harmonics would yield a λ^1_M that is invariant with position at which the FEA was performed to find the phase linkages of PM flux. For motors rich in harmonics, spp=1,2, 3, λ_{M_2D} would show a dependence on rotor position with sixth and multiples of sixth harmonics. To extract the fundamental component of the flux, the FEA computation is repeated over 60°/spp electrical angle and the average is taken. Effect of skew incorporated analytically and is discussed in a further subsection.

For the expected range of operation of current density, similarly, $L_{d\_2D}(i_d)$ and $L_{q\_2D}(i_q)$ is found by applying current density in steps on the –d and q axes.

$$L_{q\_2D} = \frac{\lambda_q^1}{i_q} \tag{14}$$

$$L_{d\_2D} = \frac{\lambda_d^1 - \lambda_M^1}{i_d} \tag{15}$$

Stators of synchronous machines are skewed (especially for spp=1, 1.5, 2, 3) for reducing or eliminating cogging torque or torque harmonics. The effects of skewing are incorporated a-posteriori into the equivalent circuit calculations. For eliminating cogging torque, the skew angle is given by

$$\alpha_{sm} = \frac{2\pi}{lcm(N_s, N_p)} \tag{16}$$

$$\alpha_{se} = \frac{N_p}{2}\alpha_{sm} \tag{17}$$

Stator skew results in a reduced fundamental of magnetic flux linkage and is very accurately modeled using the skew factor as given in (18). Similar to this effect, the saliency ratio of the machine will also get reduced by another factor. Due to the double periodicity of inductance saliency, the skew factors in (19) and (20) as for twice the skew angle as that affecting the fundamental flux.

$$\lambda_{M\_skew} = \lambda_{M\_2D}\frac{\sin(\alpha_{se}/2)}{\alpha_{se}/2} \tag{18}$$

$$L_{d\_sskew} = \frac{(L_{d\_2D} + L_{q\_2D})}{2} + \frac{(L_{d\_2D} - L_{q\_2D})}{2}\frac{\sin(\alpha_{se})}{\alpha_{se}} \tag{19}$$

$$L_{q\_sskew} = \frac{(L_{d\_2D} + L_{q\_2D})}{2} - \frac{(L_{d\_2D} - L_{q\_2D})}{2}\frac{\sin(\alpha_{se})}{\alpha_{se}} \tag{20}$$

where λ_{M_2D} is the PM flux linkage of the non-skewed stator computed by FEA and λ_{M_skew} is the PM flux linkage after skewing, L_{d_2D} and L_{q_2D} represent the d- and q- axis

inductances computed by FEA while L_{d_skew} and L_{q_skew} represent the d- and q- axis inductances due to effect of skewing

Unlike stator skew, rotor skew is difficult and impractical if a continuous skew is used. Instead, a stepped skew is easily manufactured. For electrically conducting PM's, splitting the rotor also offers an advantage of reduced PM eddy current losses. Cogging torque may not be completely eliminated as in the case of stator skew, but the fundamental component of cogging torque may be eliminated by a shift of half stator slot pitch between two equal rotor stepped parts.

Thus if the rotor has 'n_{rs}' slices, each of stack length l_{rsk}, that are shifted by an electrical angle from a reference angle of θ_r=0 by θ_{rsk}, then the rotor skew factor for n^{th} harmonic is given in equation (21) and the effect on unit length of d- and q- axis inductances can be calculated as in equations (22) and (23):

$$k_{srn} = \frac{\sum_{k=1}^{n_{rs}} L_{rks}\, e^{jn\theta_{rsk}}}{\sum_{k=1}^{n_{rs}} L_{rsk}} \tag{21}$$

$$L_{d\_rskew} = \frac{(L_{d\_2D} + L_{q\_2D})}{2} + \frac{(L_{d\_2D} - L_{q\_2D})}{2} \frac{\sum_{k=1}^{n_{rs}} l\, e^{j2\theta_{rsk}}}{\sum_{k=1}^{n_{rs}} l_{rsk}} \tag{22}$$

$$L_{q\_rskew} = \frac{(L_{d\_2D} + L_{q\_2D})}{2} - \frac{(L_{d\_2D} - L_{q\_2D})}{2} \frac{\sum_{k=1}^{n_{rs}} l\, e^{j2\theta_{rsk}}}{\sum_{k=1}^{n_{rs}} l_{rsk}} \tag{23}$$

It is worthwhile to note here that the effect and formulation is analogous to that of winding distribution factor due to phase differences between coils. For a PM motor, a rotor with half step that is displaced by 180°/5 electrical from the other half can eliminate 5^{th} harmonic from its back emf. If two such sections are displaced from each other by 180°/7 electrical, that would eliminate 7^{th} harmonic torque from its back-emf.

This would, however, not eliminate 6th harmonic torque as the effects on harmonics in inductances will be different and components causing 6th harmonic torque would still be present, but to a lesser degree as compared to the un-skewed case.

Including end-winding inductances into equivalent circuit

The effective d- and q- axis inductances for the equivalent circuit of the machine are then given by (for double layer):

$$\lambda_M = \frac{\gcd\,(N_p, N_s)}{p} l_{stack} \lambda_{M\_2D} \cdot n_t \tag{24}$$

$$L_d = \frac{\gcd(N_p, N_s)}{p^2} (L_{d\_2D} l_{stack} + L_{ew}^1) \cdot n_t^2 \tag{25}$$

$$L_q = \frac{\gcd(N_p, N_s)}{p^2} (L_{q\_2D} l_{stack} + L_{ew}^1) \cdot n_t^2 \tag{26}$$

It can be similarly calculated for single layer as well, depending on periodicity of the winding function.

End-winding leakage

The leakage inductance of the end winding is calculated by assuming that end winding current produces only circular flux in the plane normal to direction of the current[48]. Figure 15 shows the end winding region portion for a form wound coil consisting of a straight portion and a slanted portion. To determine the end-winding leakage inductance, the current flowing through the slant portion of the winding is divided into two components i.e. the axial component (I_{ax}) and the circumferential component (I_{cir}). The total end winding inductance is calculated by taking following flux in to account:

1) flux produced by the winding current over the straight portion of the conductor
2) flux produced by the axial component of winding current over the slant portion of conductor
3) flux produced by the circumferential component of winding current over the slant portion of conductor
4) flux linkage within the conductor

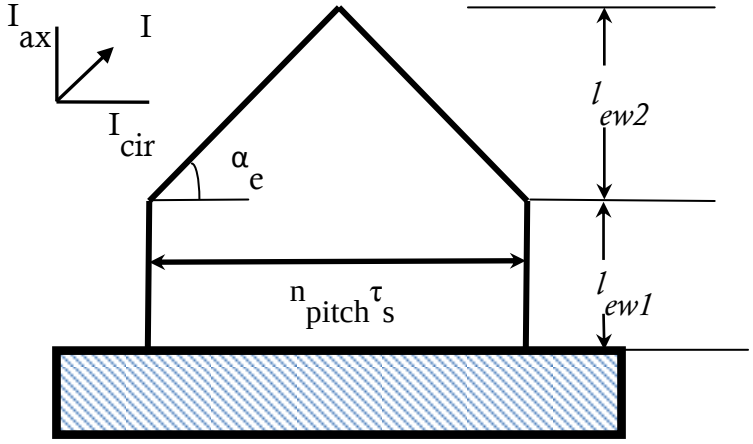

Figure 15 End-winding inductance modeling

This model leads to the effective calculation as presented in ()-() for form-wound coils. The full derivation is presented in [48]. The formulae are adapted to the notation presented in this text.

$$L_{ew}^{1} = 8\frac{{k_{d1}}^{2}{k_{p1}}^{2}}{N_p}\left(\frac{N_s}{3p}\right)^{2}(L_{ew1} + L_{ew2} + L_{ew3} + L_{ew4}) \tag{27}$$

where k_{d1} and k_{p1} are the pitch and distribution factors for fundamental flux component, other terms are calculated as shown below:

$$L_{ew1} = \frac{\mu_o l_{ew2}}{\pi} \log_e \left(\frac{n_{pitch} \tau_s}{\Delta R} \right) \tag{28}$$

$$\Delta R = \sqrt{\frac{A_c}{k_f \pi}} \tag{29}$$

$$L_{ew2} = \frac{\mu_o l_{ew1}}{\pi} \left[\log_e \left(\frac{n_{pitch} \tau_s}{\Delta R} \right) - 1 \right] \sin \alpha_e \tag{30}$$

$$L_{ew3} = \frac{\mu_o}{\pi} \left[\frac{n_{pitch} \tau_s}{2} \log_e \left(\frac{\frac{n_{pitch} \tau_s}{2} \tan \alpha_e + l_{ew1}}{\Delta R} \right) + \frac{l_{ew2}}{\tan \alpha_e} \log_e \left(\frac{\frac{n_{pitch} \tau_s}{2} \tan \alpha_e + l_{ew1}}{l_{ew2}} \right) - \frac{n_{pitch} \tau_s}{2} (1 + \log_e 2) \right] \tag{31}$$

$$L_{ew4} = \frac{\mu_o}{8\pi} \left(2 l_{ew2} + \frac{n_{pitch} \tau_s}{\cos \alpha_e} \right) \tag{32}$$

The end-winding inductance calculation of random-wound coils is a special case with $\alpha_e = 0$ and can be derived from the same set of equations presented above.

3.6.2. Demagnetization limits

This function first checks if the PMs in a machine would face the risk of demagnetization at the maximum expected operating current. If the machine does face this risk, then the maximum limit of safe operation is determined.

Inputs:

a) reference rotor position

b) expected maximum current I_{max} in the single-turn coil

c) demagnetization curve of the PMs at most vulnerable temperature

Output:

a) min(I_{max}, I_{demag}) where I_{demag} is the current at which demagnetization begins

For each design, a quick check whether the design faces risk of demagnetization should be made. In order to find the safe limit, the fully magnetized B-H characteristic of the PM material is changed to its most vulnerable temperature for demagnetization. For instance, the knee point of ceramic 8 grade ferrite happens at low temperature. Also, for accurate estimation, a relatively finer mesh of at least $1/5^{th}$ the smallest edge of the magnet is used.

At first, the maximum expected winding current is applied on the negative d-axis and percentage demagnetization is found. If the PM shows no sign of demagnetization, then the maximum current I_{max} for the design is left unaltered and the function returns I_{max} as the limit without checking for higher currents. Otherwise, a binary search is performed to find the demagnetization current as shown by algorithm of figure. The process is further sped up by using initial field at each node from a previously computed field solution. For models with multiple PMs within the slice of the machine, which happens for non-integral spp machines, each PM is subjected to different demagnetizing field. In this case, the percentage demagnetization of each PM should be checked.

3.6.3. Electromagnetic torque and terminal voltage for an operating condition

Torque and coil flux linkage for a known current excitation in the windings can be found by a series of magnetostatic solutions assuming that the current excitation is pure sine 120° electrical shifted between the three phases. For an un-skewed geometry,

this is done by simply calling the position stepped FEA function and specifying the current excitation angle based on the operating point. For operating points within the voltage ellipse, the current angle is chosen from the MTPA condition. For field weakening operation the optimum point of operation is calculated from the voltage limited ellipse at the required speed.

While the skew factors in (18), (19), and (20) account for the effect of adding rotated 'slices' of the machine [49], torque is produced in each slice only due to the axial component of current. To include this effect, the winding current is multiplied by a factor $cos(\beta_{sm})$ as given in (34), where β_{sm} is the weighted average of the conductor angle β (shown in Figure 16) over the slot as in (33), where ⟨R⟩ is the average conductor location radius from motor axis. The subscript 'm' in β_{sm} indicates that this is a purely mechanical i.e. geometry based quantity. Note that this angle is dependent on the axial length of the stack. A shorter stack will result in a larger angle causing a more detrimental impact on the resistance as compared to a longer stack with a smaller β_{sm}.

$$\beta_{sm} = \tan^{-1}\left(\frac{\alpha_{sm}\langle R\rangle}{l_{stack}}\right) \tag{33}$$

$$i_{ph\_skew} = i_{ph}\cos\beta_{sm} \tag{34}$$

Torque computation is performed for the three cases using the procedures shows in Table 5.

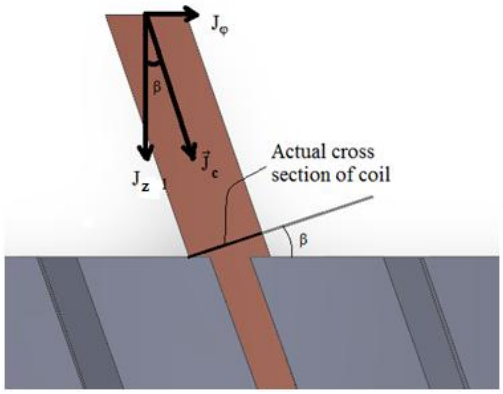

Figure 16 Torque producing component of the coil current is reduced due to skew

Table 5 Algorithm for computing torque for different cases of skew

Algorithm: compute_torque()

Inputs: *initial rotor position, final rotor position, current magnitude, current excitation angle, rotation step size, skew steps*
Outputs: *Torque vs. rotor position, flux linkage of three phases vs. rotor position for unit stack length*

switch: skew type
case: no skew
[T_{em}, *lambda*] = position_stepped*(initial rotor position, final rotor position, current magnitude, current angle, rotation step size, 0)*$*l_{stack}$

case: rotor skew
For each rotor step
[T_{em}*_step, lambda*] += position_stepped(*initial rotor position, final rotor position, current magnitude, current excitation angle, rotation step size, theta_step*) *l_{step}
EndFor

case: stator skew
For each slice
[T_{em}*_step, lambda*] += position_stepped(*initial rotor position, final rotor position, current magnitude, current excitation angle, rotation step size, theta_slice*) *l_{slice}
EndFor

3.6.4. Cogging torque

Certain applications impose a requirement on the machine that the shaft should be able to rotate freely without cogging when the machine windings are unexcited.

Cogging torque has a periodicity of *lcm(N_s,N_p)* for one mechanical rotation of the shaft. Hence it can be almost completely eliminated by a stator skew of $\frac{360^\circ}{lcm(N_s,N_p)}$ mechanical angle. In general, machines with larger *lcm(N_s,N_p)* exhibit lower magnitude of cogging torque. Cogging torque is computed by calling the position stepped FEA function for a total rotation of $\frac{360^\circ}{lcm(N_s,N_p)}$ and zero current excitation.

For stepped rotor skew, the same procedure is followed by shifting position for each stepped skew unit of the rotor.

Magnetic fields in stator show single slot pitch symmetry at no-load. This means that the field solution of cogging torque for $\frac{360^\circ}{lcm(N_s,N_p)}$ mechanical angle can be utilized for calculating no-load (zero current) core losses.

3.6.5. Ohmic losses

For the general formula for ohmic loss in the machine is given by:

$$P_{Cu} = \frac{\kappa_{ac}}{\sigma_{Cu}} \frac{J_c^2}{2} V_{Cu} \tag{35}$$

$$V_{Cu} = N_s A_c (l_{stack} + l_{ew}) \tag{36}$$

where V_{Cu} is the total volume of copper in the machine, l_{ew} is the length of the end turn and $\kappa_{ac}$is the ac resistance coefficient arising from eddy currents due to skin and proximity effects in stator conductors. The ac loss coefficient κ_{ac} is defined as the ratio of ac loss to dc loss. For multi-strand windings, $\kappa_{ac} \cong 1$.

Inclusion of skin and proximity effects

For thicker conductors in high frequency operation of machines, especially conductors with dimensions comparable or greater than skin depth may show increased ac resistance due to eddy effects. Ac resistance coefficient needs to be included in ohmic loss calculation. The steady state one dimensional diffusion equation applies to each conductor with the constraint that the total current over the cross section of each conductor is known. The ac loss coefficient is difficult to model for round conductors and is based on certain approximations or is calculated by time harmonic FEA [50]. For rectangular conductors, an exact solution can be found for the diffusion equation:

$$\frac{\partial^2 J_z(y,t)}{\partial y^2} = \frac{b_c \mu_0 \sigma}{SW} \frac{d}{dt} J_z(y,t) \tag{37}$$

where b_c is the width of the conductor which is the slot width (*SW*) less the insulation, interface gap and slot paper, J_z is the current density in axial direction, σ is conductivity of conductor, and μ_0 is permittivity of free space. On solving, simplifying, and integrating for conduction loss, for i^{th} conductor, we get the power loss:

$$P_{ac,i} = \frac{l_{stack}}{\sigma h_{ci} b_c} \{(I_i - I_{i-1})^2 \Delta F(\Delta) + 2 I_i I_{i-1} \Delta G(\Delta)\} \tag{38}$$

where $\Delta = h_{ci} \sqrt{\frac{\omega \mu_0 \sigma b_c}{2 \cdot SW}}$,

$$F(\Delta) = \frac{\sinh(2\Delta)+\sin(2\Delta)}{\cosh(2\Delta)-\cos(2\Delta)}, \text{ and } G(\Delta) = \frac{\sinh(\Delta)-\sin(\Delta)}{\cosh(\Delta)+\cos(\Delta)} \tag{39}$$

Note: The above equations represent an exact model of eddy effects in conductors that has been tested on a prototype motor for accuracy in a separate study involving bar conductors.

Effect of stator skew on ohmic loss calculations

Stator skew has a two-fold effect on the phase resistance and hence ohmic losses: one due to increased length of conductors and second due to decreased cross section due to skew. This is accounted for by including a factor in the resistance as in (40) where r_{ph} is calculated resistance based on slot area, slot fill factor and a model for accounting end-turn length; r_{ph_skew} is the modified resistance due to skew.

$$r_{ph\_skew} = \frac{r_{ph}}{\cos^2(\beta_{sm})} \tag{40}$$

From the definition of β_{sm}, it can be deduced that this factor affects designs with shorter stack lengths more.

3.6.6. Core loss estimation

Input:

a) Magnetic field intensity B_x and B_y for each element of the mesh for 60° electrical rotation

Output:

a) Hysteresis loss coefficient (p_h^1) per unit stack length

b) Eddy current loss coefficient (p_c^1) per unit stack length

The total machine core loss for the given current density excitation applied at the given current angle can be found by:

$$P_{core} = (p_h^1 \cdot f_e + p_c^1 \cdot f_e^2) \cdot l_{stack} \tag{41}$$

Core losses may account for a significant loss component for an electric machine. For any operating condition of the electrical machine, the core loss can be predicted by

an *a-posteriori* computation based on the magnetic field data at each element of the finite element mesh [51]. Core loss computation in rotating machines requires special consideration due to presence of non-sinusoidal and rotating fields. Conventional models use the Steinmetz formula with separation of hysteresis and eddy current losses given by:

$$P_{core} = P_h + P_e = \frac{1}{T}\int_0^T k_h \left|\frac{d\bar{B}}{dt}\right| B^a + k_e \left|\frac{d\bar{B}}{dt}\right|^2 \tag{42}$$

The coefficients a, k_h and k_e are constants for this formulation. However, this model may not accurately predict losses over the entire range of operating frequency and magnetic field [52]. A variable coefficient model that relies on curve-fitting these coefficients to available Epstien test loss data for a large range of frequencies and magnetic fields was proposed in [53]. The improved model proposed in [53] assumes the loss coefficients to be functions of magnetic field and frequency. A variation of this model uses a frequency domain approach. The improved formula is thus:

$$\mathrm{P_{core}} = \mathrm{P_h} + \mathrm{P_e} = \sum_{\mathrm{n=1}}^{\mathrm{n_{max}}} \mathrm{k_h}(\mathrm{nf_1}, \mathrm{B_n})(\mathrm{nf_1})\mathrm{B_n^2} + \sum_{\mathrm{n=1}}^{\mathrm{n_{max}}} \mathrm{k_e}(\mathrm{nf_1}, \mathrm{B_n})(\mathrm{nf_1})^2\mathrm{B_n^2} \tag{43}$$

where *n* represents the order of harmonic considered and f_1 represents the frequency of fundamental harmonic. The maximum number of harmonics that would be included in this computation depends on the step size used for position-stepped FEA. The frequency components are calculated by assembling the magnetic field variation over 60° electrical computation to construct the full 360° cycle of variation of vector magnetic field for each element of the mesh [16].

3.6.7. Rotor solid loss estimation

Eddy currents are induced in electrically conducting PMs from exposure to time-varying magnetic fields induced by stator currents. Sintered NdFeB and SmCo magnets are susceptible to this loss due to their high electrical conductivity. Hard ferrite PMs are non-conducting and do not experience this additional loss component. In practical motors, these losses are mitigated by segmenting the PM into several axial and circumferential pieces [54].

At any point, the field variation over an electrical cycle is known from the position-stepped FEA and can be used to predict the induced current density from:

$$J_{PM} = -\sigma_{PM} \frac{\partial A_z}{\partial t} \tag{44}$$

However, this does not account for end effects due to the shape of current loops inside the PMs. This formula is expected to predict losses for magnets that have a large axial dimension as compared to the circumferential direction. Methods to compute solid PM loss are typically based on 3D transient FEA [55]. Recently Zhang *et al*. proposed a method that combines 2D magnetic field data [56] with an approximate analytical model of the current loops to estimate PM loss. These methods need to be included in the framework for fast computation of PM losses. In case of SPM motors, a 'retaining can' may be used to prevent PMs from flying off due to centrifugal force. This may lead to an additional loss component due to eddy currents in the retaining can. This loss component needs to be included in loss calculations as well [57].

3.6.8. Current angle: MTPA operation and field weakening

This module has several functions that use the electrical lumped circuit model to calculate optimum current angle with or without field weakening and CPSR. The torque and loss obtained using the electrical lumped equivalent circuit should match the results obtained using position-stepped FEA. This would imply that the lumped parameters used for MTPA and FW calculations are accurate. However, if there is an error, the approximate values returned from this module are corrected by a search for the optimum current angle based on position-stepped FEA in the proximity of the values calculated from this lumped electrical circuit.

MTPA current angle

Inputs:

a) λ_{M_2D} ,

b) $L_{q\_2D}(J_{z\_q})$,

c) $L_{d\_2D}(J_{z\_d})$,

d) J_z,

e) A_c

Output:

a) γ_{MTPA}

The MTPA calculation step determines the optimum current angle to apply in order to achieve the best torque for a given current excitation. Since this step is performed before the torque computation, for certain design problems for which the l_{stack} is not fixed from the design specification or is not determined when this function is

called, the lumped circuit parameters are unknown. Therefore we consider current density J_z as the input instead of the phase current. The phase current is now a dependent parameter that is given by (for double layer winding):

$$I_{ph} = p\frac{J_c A_c}{2n_t} \tag{45}$$

The optimum current angle for MTPA condition, can be expressed in terms of L_{d_2D} and L_{q_2D}, λ_{M_2D} and J_z:

$$\begin{aligned}\sin(\gamma_{MTPA}) &= \frac{-\lambda_M + \sqrt{\lambda_M^2 + 8\left(L_q - L_d\right)^2 I_{ph}^2}}{4\left(L_q - L_d\right)I_{ph}} \\ &= \frac{-\lambda_{M\_2D} + \sqrt{\lambda_{M\_2D}^2 + 8\left(L_{q\_2D} - L_{d\_2D}\right)^2 \left(\frac{J_z A_c}{2}\right)^2}}{4\left(L_{q\_2D} - L_{d\_2D}\right)\left(\frac{J_z A_c}{2}\right)}\end{aligned} \tag{46}$$

This happens because the end-winding leakage inductance terms contribute equally to d- and q- axis inductances and are cancelled out in (L_q-L_d) terms in numerator and denominator and all the terms related to l_{stack}, n_t and p disappear. The calculations for optimum current angle are based on equivalent circuit parameters derived from 2D FEA. Thus saturation effects are taken into consideration. Since L_{q_2D} and possibly L_{d_2D} are dependent on J_{z_q} and J_{z_d}, the calculation is carried out iteratively until γ_{MTPA}, $L_{q\_2D}(J_z*cos(\gamma_{MTPA}))$ and $L_{d\_2D}(J_z*sin(\gamma_{MTPA}))$ are converged.

FW Mode current angle

Inputs

a) λ_{M_2D} ,

b) $L_{q\_2D}(J_{z\_q})$

c) $L_{d\_2D}(J_{z\_d})$

d) r_{ph}

e) l_{stack}

f) L_{ew}

g) V_s

h) I_s

i) T^*_{em}

j) ω^*_e

Outputs:

a) Optimum current angle γ_{opt}

b) If VA is not sufficient to operate at (T^*_{em}, ω^*_e) then the minimum required VA_{min}

This module is invoked only when VA limited operation is a given constraint or if minimization of VA is an objective in the problem definition. If a design problem requires the machine to operate at more than one operating point (defined by T_{out} and ω_r), such that $T_{out1} > T_{out2}$, $\omega_{r1} < \omega_{r2}$ and $T_{out1}\omega_{r1} > T_{out2}\omega_{r2}$ as shown in Figure 17, then the VA of the drive is decided based on MTPA operating point 1, and operation at point 2 is achieved by means of field weakening operation. In order to compute the minimum VA requirement at point 2 and to perform a position stepped FEA for this point, we need to specify the current magnitude and current angle. In the FW region, the current components i_d and i_q can be found by traversing the voltage limited operation ellipse

while ensuring that the magnitude of current is less than rated current as shown in Figure 17(b). If the operating point (T_{out2}, ω_{r2}) lies outside the FW region of the machine, then the VA of the drive is determined by expanding the voltage ellipse such that current excitation required to achieve (T_{out2}, ω_{r2}) lies exactly on the ellipse.

VA limited operation in the field weakening regime of the machine is dependent on the stack length unlike the MTPA calculation. This is because the voltage equations (3) and (4) depend on the d- and q- axis inductances which include the end-winding leakage inductance. Hence, this function requires two additional inputs: stack length l_{stack} and end-winding inductance $L_{ew,}$ in addition to inputs provided to MTPA function.

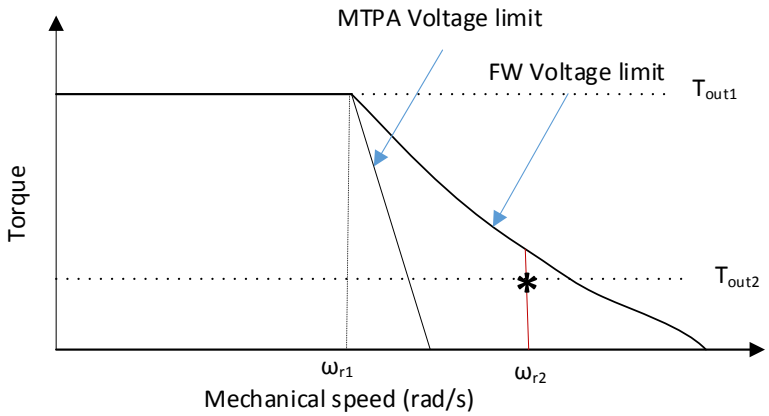

(a)

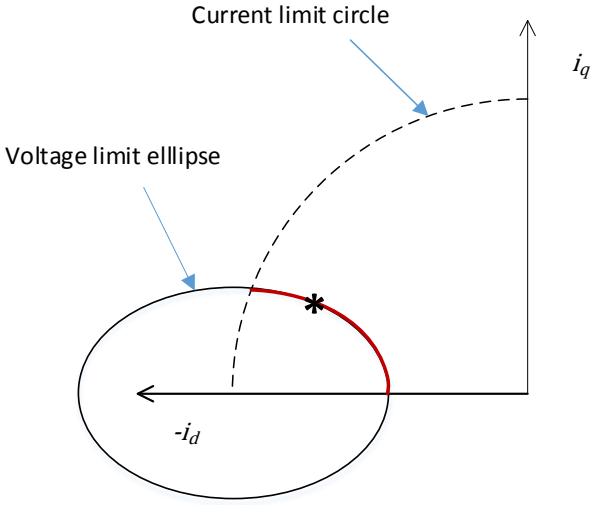

(b)

Figure 17 Field weakening operation of synchronous machine

Constant power speed range (CPSR) and Efficiency-constrained constant power speed range (EC-CPSR)

Inputs:

a) P_{out}

b) λ_{M_2D}

c) $L_{q\_2D}(J_{z\_q})$

d) $L_{d\_2D}(J_{z\_d})$

e) r_s

f) l_{stack}

g) L_{ew}

h) J_z

i) R_{gap}

j) N_p

k) p_h^1

l) p_c^1

m) η* (for EC-CPSR)

Outputs:

a) CPSR / EC-CPSR

b) γ at $\omega_{r,max}$

This function returns an initial guess to estimate the constant power speed range (CPSR) or the efficiency constrained CPSR. CPSR of a motor is defined as the ratio of the maximum achievable speed at rated power to its base speed. Base speed is defined as the maximum speed up to which it is possible to operate the motor by applying rated current excitation at the optimum current angle. From the loss-free model of machine, it is deduced that if normalized PM flux linkage to normalized d- axis inductance, $\lambda_{Mn}/L_{dn}=1$, the CPSR of the machine can be extended to infinity [5]. However, the actual mechanical output of the machine reduces at high speeds due to windage and core losses.

In this context, CPSR is defined based on the actual mechanical output power at the shaft rather than the electromagnetic output torque. The effects of saturation and stator resistance were briefly studied in [6] and are included here analytically by subtracting from the lossless power vs. speed curve.

Additionally, since the machine may operate continuously delivering rated power at ω_{max}, the problem definition may impose a constraint on minimum efficiency at ω_{max}. Thus, CPSR is defined based on power curve obtained after accounting for all machine losses. Additionally, in order to meet the constraint of efficiency at maximum speed, the top speed of the machine ω_{max} is chosen as the speed at which efficiency of the motor at rated power is 90%. This definition of EC-CPSR is depicted for an example motor characteristic in Figure 18. This definition is possible, since it is known that efficiency at rated power will drop at higher speeds due to increase in windage losses. EC-CPSR is the first objective of the optimization problem of this paper.

Two additional considerations may impose a constraint on the maximum speed of operation:

1) Uncontrolled generation (UCG) mode: This applies for designs that operate in FW mode [58]. Maximum normalized speed is limited to $1/\lambda_{Mn}$. Alternatively, the α_{min} which is the lower limit of the bistable UCG zone is chosen to be the maximum speed.
2) Mechanical limit on maximum speed: If the maximum mechanically allowable speed is less than maximum speed calculated based on CPSR or EC-CPSR conditions, the maximum speed is limited based on this constraint.

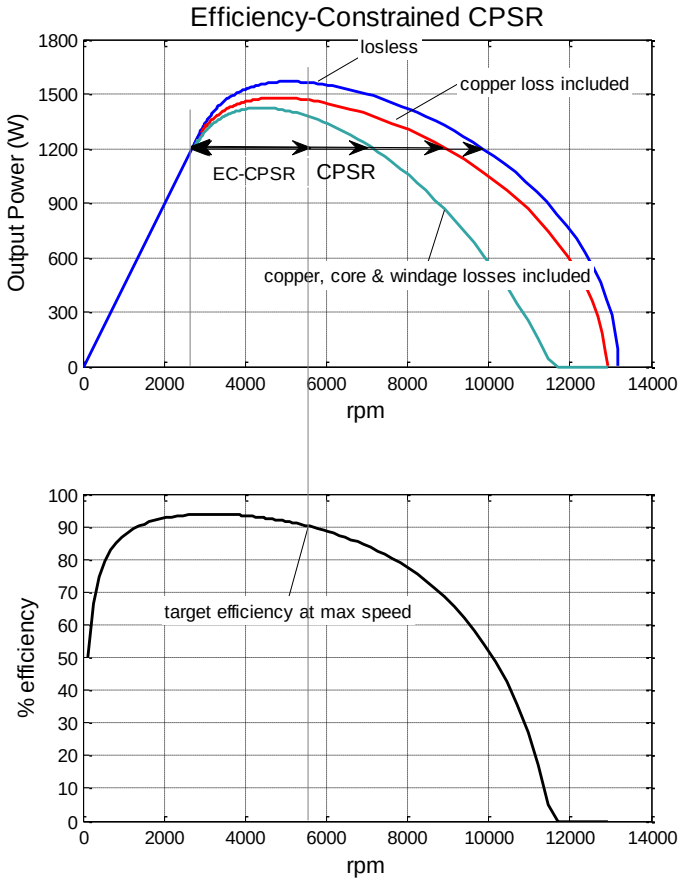

Figure 18 Modified definition of CPSR and definition of EC-CPSR

3.7. Mechanical loadability and losses

3.7.1. Maximum operating speed

The mechanical loadability of the rotor is the maximum speed at which the rotor can operate safely without causing excess vibrations or stresses in the shaft and rotor structure. In principle the operating speed range is limited by three factors:

1) Centrifugal forces in the rotor
2) Torsional vibrations of the coupled shaft-load system
3) Natural resonant frequencies of vibration of the rotor

For higher speed motors, usually the PMs are buried and the maximum stress due to centrifugal forces occurs in the center-posts and bridges. Due to the fairly complicated geometry of the rotor, the maximum safe speed of operation is typically, computed by a 3D FEA (small displacement). The high stress in center-posts of the 2007 Toyota Camry drive motor is computed using 3D mechanical FEA shown in Figure 19. The second and third mechanical limitation can be overcome by using stiff coupling mechanisms and thicker shafts for increasing the natural frequency. However the phenomenon of centrifugal forces is the most important limiting factor for power density of a machine. In this research, centrifugal force limitation is used to determine the maximum operating speed constraint for the machine.

3.7.2. Mechanical losses: friction and windage

The windage loss P_w for a rotating cylinder is calculated from mechanical speed ω_m as [59]

$$P_w = \pi C_d l_{stack} R_{ri}^4 \omega_r^3 \rho_{air} \tag{47}$$

where l_{stack} is the stack length, R_{ri} is rotor inner radius, g is air gap, ρ_{air} is air density, v is kinematic viscosity of medium, and C_d is the drag coefficient which is calculated differently for laminar and turbulent flow field in the air-gap. For laminar flow, it is given by (49), and the empirical relation for turbulent field is given by the implicit relation (48).

$$\frac{1}{\sqrt{C_d}} = 2.04 + 1.768 \ln \left(\frac{\omega_r g R_{ri}}{\nu} \sqrt{C_d}\right) \tag{48}$$

$$C_d = \frac{2}{Re} \tag{49}$$

The two windage loss relation needs to be solved iteratively for turbulent flow.

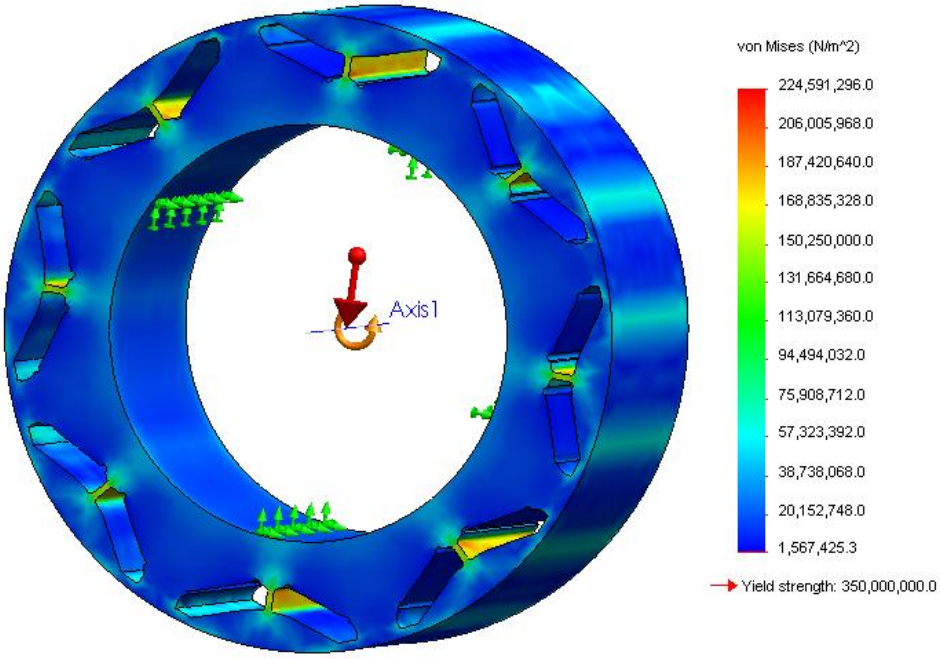

Figure 19 Von Mises stress developed in rotor center-posts of the 2007 Toyota Camry hybrid drive motor [60] due to centrifugal forces at 15000 rpm

3.8. Paradigms of fitness evaluation algorithms using proposed framework

The fitness evaluation process may involve numerical methods and may be iterative. Therefore, the number of evaluations needs to be minimized. One approach to achieve better convergence is to ensure that the optimizer generates only feasible designs. This can be done in several ways: firstly, if the inequality constraints are given in the form of direct equations, input parameters can be encoded so that chosen bounds will automatically satisfy the inequality constraints. The transforms should be designed in a way that does not restrict the search space. A second approach that is suitable for

complex relation between input parameters and inequality constraint is using penalty functions. This approach is indirect because it only decreases the probability of new individuals in the infeasible regions of the parameter space.

A design problem may have equality constraints, some satisfied easily than others. For example, an equality constraint on volume is easily satisfied by making stack length l_{stack} a dependent parameter on outer diameter. On the other hand, a machine that is required to output a desired torque at a given speed is defined by an equality constraint that is not easily met. Another example is a design problem where volume of a machine is to be minimized for a given torque output with no mention of efficiency in the problem definition. This means that unless the current density limit is reached due to demagnetization, all optimum designs will lie on the thermal constraint boundary i.e. the winding temperature will reach the insulation limit. This will impose a soft equality condition that maximum winding temperature should be close to rated insulation temperature.

Equality constraints highly reduce the probability of convergence as can be visualized from Figure 20. The equality constraint could be a hard equality constraint i.e. the point should lie exactly on '$h(\boldsymbol{X}) = 0$' or a soft equality constraint i.e. it could lie in close vicinity of '$h(\boldsymbol{X}) = 0$'. The best method for handling equality constraints is elimination of one input for each equality constraint. This ensures that candidates are generated in the feasible region directly. A naïve approach of discarding infeasible designs may fail to find a single solution on the actual pareto-set [19]. However, in case the constraint is not an explicit function of input variables, elimination cannot be used

and closeness to equality constraint should be made an objective for minimization. To reduce computation time and cost, it is essential to tailor the problem formulation in order to limit the number of evaluations and generate designs only in the feasible parameter space.

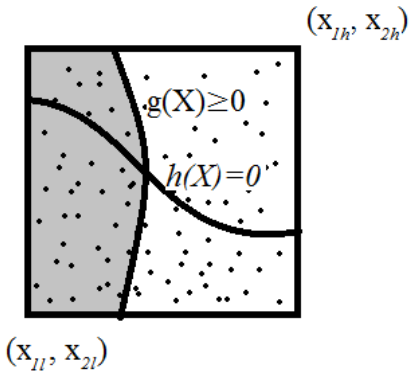

Figure 20 Constraining the search space of a two parameter space with an inequality and an equality constraint

3.8.1. Known size and known operating point(s)

Consider a 'category 3' design problem that defines the overall dimensions of the machine by imposing condition on volume, weight or cost. The GA parameters and this condition completely determine all geometric dimensions of the machine. If the machine is expected to deliver a certain output, let's say a continuous torque T^*_{out} at a fixed shaft speed ω_r, this condition imposes an equality constraint on the current density since that is the only parameter that can be altered to meet the torque condition. However, solving for J_c to achieve a desired torque involves numerically solving the non-linear equation (50).

$$T_{out}^{*} = T_{em}(J_c) - \frac{P_{core}(J_c, \omega_r) + P_{mech}(\omega_r)}{\omega_r} \quad (50)$$

Since the relation between T_{out} and Jc is monotonic, and the derivative is also monotonic, the solution for J_c is very easily obtained by secant method.

This method can be extended by following the same procedure if the input specifies 'n' operating points, each for continuous operation.

3.8.2. Known operating point (continuous duty), minimize volume/weight/cost

Conversely, if a category 1 problem definition does not impose a condition on volume, weight or cost, then l_{stack} is an additional free parameter other than J_c. In this case, we have one equality constraint from torque equation and two free parameters. We choose J_c as a design parameter, and the output torque requirement imposes an equality condition on l_{stack}. The advantage of doing this is that the dependent parameter of stack length l_{stack} is easily determined as the output torque T_{out} varies linearly with l_{stack} as given in equation (51).

$$l_{stack} = \frac{T_{out}^{*}}{\left(T_{em}^{1} - \frac{P_{core}^{1}(\omega_r) + P_{mech}^{1}(\omega_r)}{\omega_r}\right)} \quad (51)$$

where T_{em}^{1}, P_{core}^{1}, P_{mech}^{1} are the electromagnetic torque, core loss and mechanical loss for unit stack length of the machine.

In both the above cases, it should be noted that due to direct coupling of the thermal and electromagnetic models, an iterative process should be adopted till the design parameter (J_c or l_{stack}) and operating temperature, both are converged.

To simultaneously determine the design parameter (J_c or l_{stack}) and operating temperature, two approaches can be adopted. In a first approach, the design variable is determined first and then used in the thermal model to determine the temperature distribution of thermal steady state. Once the temperatures are converged, the design parameter is recalculated for this operating temperature. The two processes are iteratively performed until convergence is reached for both the parameters simultaneously. This is shown graphically in Figure 21(a).

A second approach in which the calculation of design parameter (J_c or l_{stack}) is integrated into the iterative step of the thermal model as shown in Figure 21(b). This second approach is observed to converge faster by virtue of lesser evaluations of the FEA based EM model.

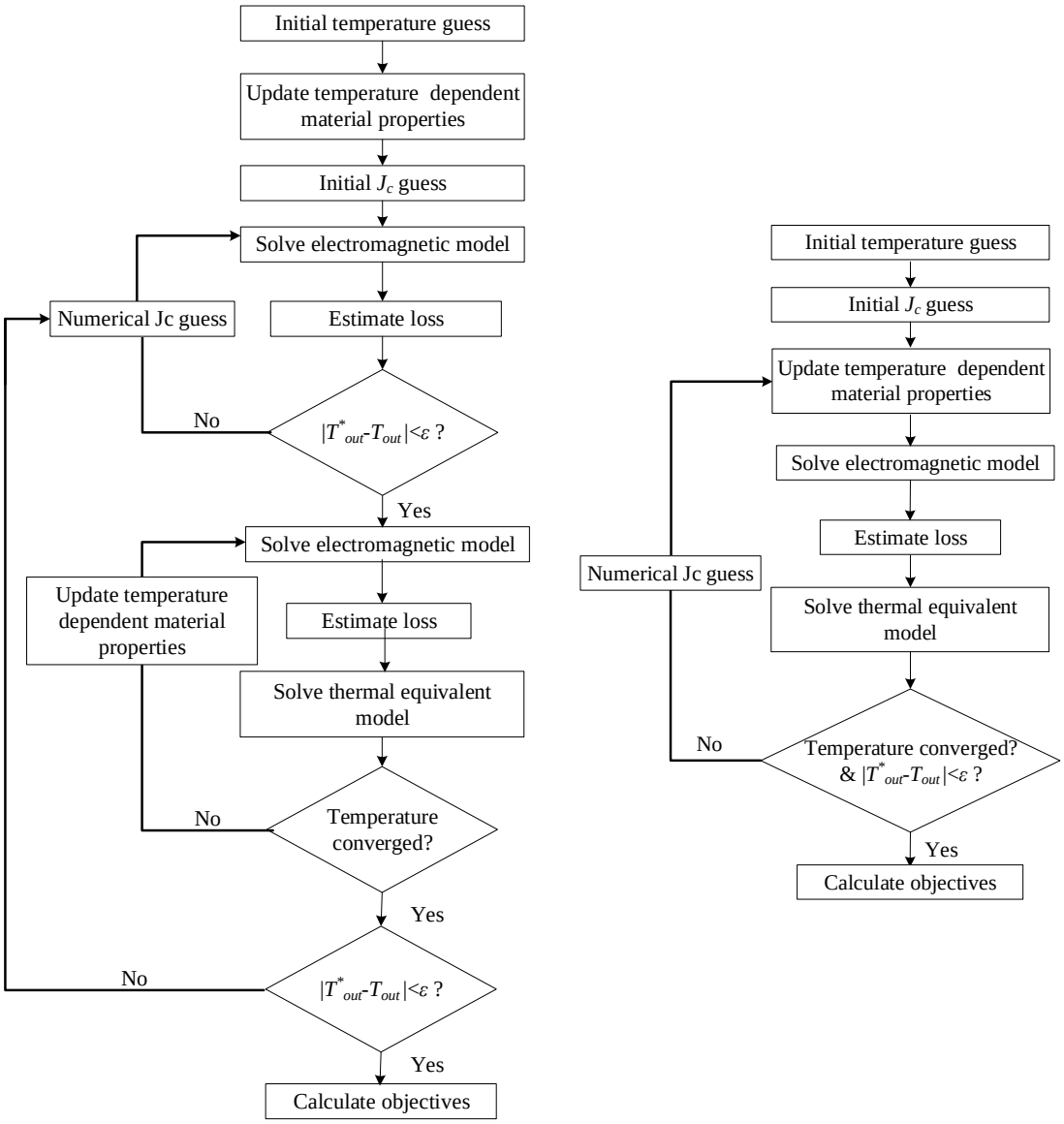

Figure 21 Two approaches to simultaneous EM-thermal solution of a free design parameter

3.8.3. Example : fixed size with combination of continuous drive cycle and short duty operation

Consider a category 2 problem that fixes the outer diameter and the axial length of the motor. The aim is to maximize the short duty capability. At the same time, another

requirement is that the motor should be able to deliver this short duty torque while operating through a repeated drive cycle operation. The drive cycle is short as compared to the thermal time constant of the system and the short duty overload re-occurs only after a long enough time that the effect of the previous overload has disappeared.

Thus, the worst case initial state for short duty overload is when the thermal state of the motor has reached steady state. To determine the steady state for repeated drive cycle operation, it is cumbersome to perform a full analysis for each operating point. Instead, the loss coefficients are extracted for 4-5 current excitation levels and the torque and core loss coefficients are calculated for different operating using a cubic spline interpolation. The full algorithm for fitness evaluation for such an application is given in Figure 22.

3.8.4. Fixed size, maximize CPSR/EC-CPSR

Let us look at a harder problem to solve: a category 3 problem, where the size of the machine is fixed, the output power is specified and CPSR needs to be maximized. However, the speed of operation is unspecified and hence is a design parameter. The machine is required to operate continuously delivering peak power rated speed (with MTPA) and at maximum speed under FW operation.

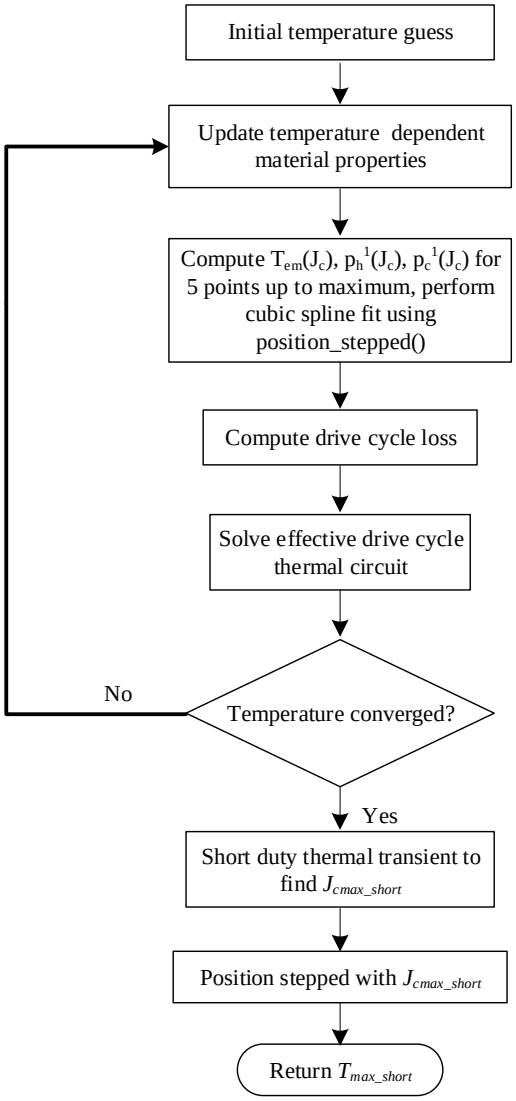

Figure 22 Fitness evaluation for a combined drive cycle and short duty operation

It is well known that a wide CPSR (theoretically infinite for lossless motor) can be achieved if the rated current of the motor is equal to its characteristic current. In a practical motor, the widest CPSR (as defined in sub-section 3.6.8 as based on the actual power output at the shaft) may not be achieved for rated current equal to characteristic current, but possibly within close vicinity of characteristic current. To increase the probability of getting only wide CPSR designs (as random designs may lie anywhere on

the “saliency-flux linkage plan” defined by Soong and Miller [6]), the fundamental current is encoded as a ratio with the fundamental characteristic current specific to the geometry associated with the rest of the gene. Once the current is fixed, the electromagnetic torque and loss coefficients can be computed by position-stepped FEA. The rated speed can be computed by solving the quadratic equation resulting from the relation:

$$\omega_r = \frac{P_{out}}{T_{out}} = \frac{P_{out}}{T_{em} - \left(p_h^1 \frac{N_p}{4\pi} + p_c^1 \frac{N_p^2 \omega_r}{16\pi^2}\right) \cdot l_{stack}} \tag{52}$$

Subsequently, the FW operation is computed and the maximum mechanically limited speed at which rated power is obtainable is computed. The full algorithm is shown in Figure 23.

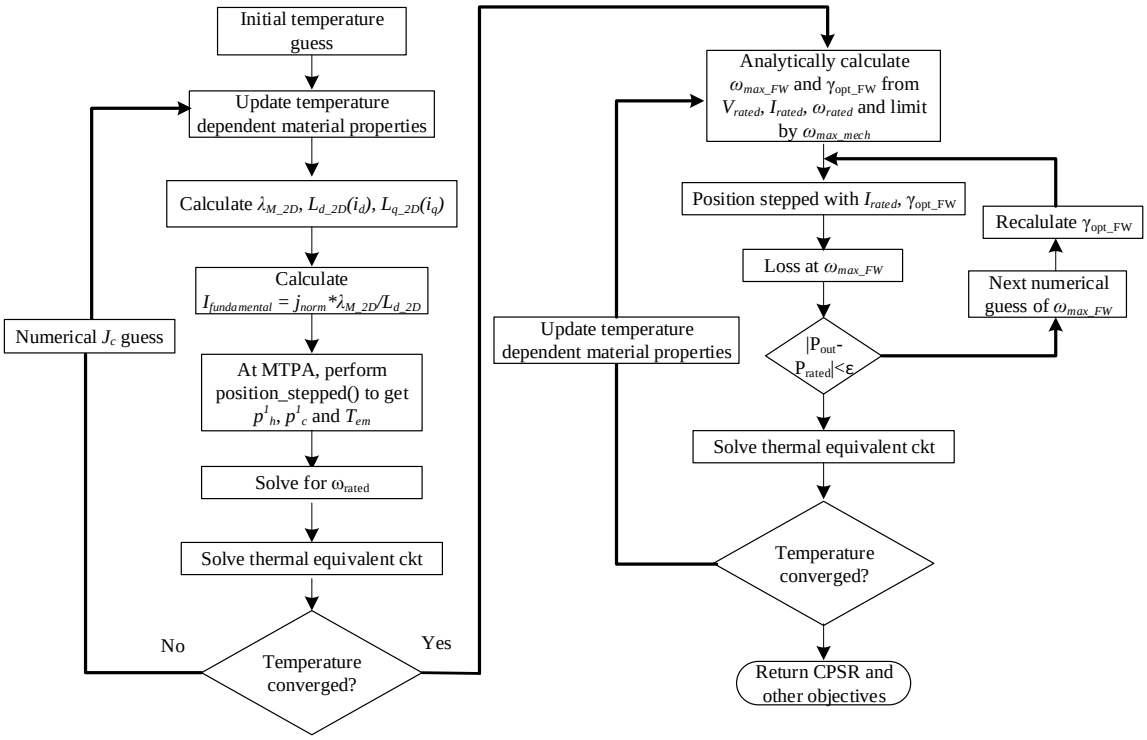

Figure 23 Algorithm for maximizing CPSR for a fixed output power and outer dimensions, but unspecified rated speed

3.9. Conclusion

The architecture of the framework and its components are presented. It is evident from the examples discussed that the framework can be adapted for wide applicability and is agile. The modeling and analysis methods adapted in the current implementation makes use of FEA based modeling that is accurate and widely applicable. To further expand the scope of 'agility', it can be noticed that component methods may have alternative forms aimed at either simplifying the analysis or improving accuracy. Thus, if an analysis method is deemed more suited for a particular design problem or topology, it can be easily amalgamated with the rest of the framework. In certain situations, e.g. the design problem discussed in subsection 3.8.4, certain steps that repeatedly use FEM

may be replaced by analytical formulae if computational resources restrict the evaluation time for an individual.

Having presented the realization of the framework, let us now see what steps are involved in deploying it to solve practical machine design problems. Let us assume that the user has defined the problem based on the black-box approach and it falls within the definition of one of the categories. Let us also assume that the evaluation algorithm is formulated on the lines of examples discussed earlier. The parts of process that are yet not yet defined are:

a) Design choices such as materials, rotor topology, winding construction, cooling method, etc
b) Encoding scheme and parameter bounds
c) Calibrated thermal circuit parameters

A generic method to determine the above design inputs is ruled out due to the high number of possible combinations of choices as well as sensitivity of thermal circuit parameters to scale of the geometry, cooling arrangement, and manufacturing method. This still presents a roadblock to complete automation. Different approaches can be used for determining these factors – simplified models can be used for initial decision making, or data from a previous machine version can be used to decide cooling method and calibrate thermal model. In certain scenarios the design process can be repeated for different choices to compare the effect of such choices.

These aspects of design choices become more salient especially for development of new technology rather than optimization of existing designs. To better understand these

aspects as well as to prove the usefulness of the proposed tool, this dissertation study involved design and implementation of three challenging design problems that are presented in detail in next three chapters of this dissertation.

4. DESIGN STUDY 1: COMPARISON OF RANDOM-WOUND AND BAR-WOUND TOPOLOGIES FOR DIRECT DRIVE SPM*

4.1. Introduction

The torque density of an electrical motor used in automobile application should be as high as possible in order to achieve better vehicle performance while meeting the stringent space and reliability constraints. The design of extremely high torque density (say 12 Nm/kg) motor becomes more challenging as the insulation and magnets are pushed to their thermal limits under peak torque requirement, which can lead to failure under extreme conditions. The wheel mounted vehicle application imposes a constraint that only air cooling can be used and complete sealing of the casing is required to prevent any water entry failures. This further worsens the temperature rise. So a good thermal design is essential for this type of motors. The usage of one rectangular strip conductor instead of many standard conductors in parallel helps in improving thermal stability as the heat capacity and effective thermal conductance of the former case are superior.

This study proposes the use of tooth-wound single slot pitch bar-conductors for improved torque density. Though almost all medium voltage and large (>500kW)

---

*Reprinted with permission from "High Torque Density Single Tooth-Wound Bar-Conductor Permanent Magnet Motor For Electric Two Wheeler Application," Yateendra Deshpande, Hamid A Toliyat, Sreeju S Nair, Jabez Dhinagar, Santhi Immadisetty and Shamsuddeen Nalakath, © 2014 IEEE accepted for publication in the Transactions of Industry Applications. In reference to IEEE copyrighted material which is used with permission in this thesis, the IEEE does not endorse any of Texas A&M University's products or services. Internal or personal use of this material is permitted. If interested in reprinting/republishing IEEE copyrighted material for advertising or promotional purposes or for creating new collective works for resale or redistribution, please go to http://www.ieee.org/publications_standards/publications/rights/rights_link.html to learn how to obtain a license from RightsLink.

machines employ bar conductors and achieve high conductor fill, such a topology is less studied for smaller machines. Comparison of thermal and manufacturing aspects of multi-stranded and solid conductor stators for low voltage generators is studied in [61]. Several recent studies are dedicated to development of high conductor fill windings suited for small (0.5-10kW) and medium (10-500kW) size machines [62-67]. In [62], authors have proposed a novel method to integrate segmented stators suitable for fractional slot concentrated windings (FSCW) with tooth-wound conductors. The advantage of this method is from the use of round conductors, a large range of turns in each coil is possible. However, the decrease in performance due to segmentation and the added manufacturing complexity may not be justified in all cases, especially for large slot numbers. To avoid segmented stator, authors have proposed the use of open slots and form-wound coils in [65]. This achieves close to 60% copper fill and is suited for multi-strand conductors only. The use of open slots with solid conductors may lead to eddy losses in conductors [68]. Other methods proposed are plug-in tooth method [67] or using pre-pressed windings in conjunction with soft magnetic composites (SMC's) [66] for single tooth-wound configurations.

To avoid either the complication of segmentation of stator, assembly of plug-in teeth, use of SMC's or increased eddy losses in conductors due to open slots, a new manufacturing method for semi-closed slots for distributed windings is gaining ground for EV/HEV applications [63, 64]. Bar wound copper conductor windings are fabricated by bending the individual conductors, axially inserting them into the slots, bending them

on the other side, and welding the ends together. The prototype tooth-wound stator with bar conductors is shown in Figure 24.

Figure 24 Photograph of the prototype single layer FSCW stator with 54 slots and 4 conductors per slot

Bar-wound FSCW stators can achieve higher conductor fill compared to stator wound with multi-stranded bundle [63]. The actual conductor fill depends on the slot size and the conductor size. For smaller slots, fraction of area occupied by slot liners is more and results in smaller conductor fill. Similarly, multi-strand conductors result in higher fraction of the available area occupied by wire enamel. Additionally, the inter-strand distance cannot be easily maintained small if the windings are not formed. For the same slot area, a relatively higher conductor fill can be achieved if bar conductors

are used. Formed conductors can overcome the disadvantage of inter-strand distance, however, at an added cost of segmented stator or open slots.

A stator with higher conductor fill means either more copper or shorter tooth height or both. The inherent advantages of bar-wound conductors are:

a) Reduced conduction losses due to high conductor fill for the same slot area or, in case of constant conductor area, reduced core losses due to shorter tooth height.
b) The effective thermal resistance between copper and laminations is reduced due to better contact. Hence lower possibility of localized hot-spots [61]
c) Reduced cost due to easier assembly, lesser insulation cost of copper wire
d) Shorter tooth height for the same conductor area, resulting in increased air-gap radius and hence torque for shaft rotating machines.
e) Ease of increasing separation between turns, thus reducing voltage surges and partial discharge due to PWM switching
f) Smaller unbalance in phase inductance that arises from slot leakage as the relative positions of conductors are fixed for bar-wound configuration. This improves sensorless control and initial position detection [69]

Tooth-wound FSCW machines have proven superior performance in several applications due to smaller and non-overlapping end-windings as well as higher pole counts [32, 70]. In this research usage of bar conductors for single slot pitch winding configuration is investigated. Different conductor arrangements for use of bar conductors with tooth-wound configuration have been proposed and discussion on fabrication is

presented. Thermal model of the stator for studying short duty torque capability is presented.

4.2. Requirements of the in-wheel direct drive motor

The design of direct drive in-wheel motor for two-wheeler presents a challenging design problem due to the stringent space constraint that it should be mountable in the wheel of a given vehicle. The motor should have a high efficiency at rated power to cruise efficiently at top vehicle speed and a high peak torque capability at low speeds to improve the uphill climbing capability and efficiency for the typical city driving cycle (CDC) of Figure 25. Conventionally, high pole-count outer-rotor machines with high energy-product NdFeB magnets are used for this application [32, 70, 71]. Despite the high torque density of such motors, the short duty torque capability is not matched for the continuously variable transmission (CVT) internal combustion engine drive. Though alternative topologies like transverse flux machines [72] present an attractive option for high torque density, the construction of such topologies presents a problem and mandates the use of powdered core since high frequency operation is required in this application.

4.2.1. Specifications for the in-wheel hub motor for electric two wheelers

The specification of the motor is derived from the vehicle requirement data [71]. The fundamental requirement is to improve the stall torque and speed range of the electric vehicle by replacing the existing benchmark motor with an improved one while reducing its size. A peak torque of 85 Nm is capable of starting the vehicle on a 10° gradient with rated payload and an additional braking torque of 10 Nm. In a worst case

scenario, the motor should be capable of delivering this torque for 60 sec continuously at start. Details of the requirement as compared to a conventional multi-stranded 40-pole 36-slot benchmark motor are given in Table 6. The weight of the motor should be minimized in order to avoid excess wear and tear of suspension.

With solid conductors, the voltage level specification cannot be necessarily met due to the low number of turns in each slot. Based on the choice of winding and geometry, the limit on back emf constant (phase-peak), if all coils are series connected, can be expressed as:

$$k_{e\_max} = \left(\frac{2\pi^2 k_w k_C B_g}{N_{ph}}\right)\frac{n_t R_g^2 l_{stk}}{SW} \tag{52}$$

where k_w is winding factor, k_C is Carter's coefficient, N_{ph} is number of phases, B_g is air-gap flux density, n_t is number of conductors in each slot, R_g is air-gap radius, l_{stack} is stack length, SW is slot width.

Table 6 Design specification of the desired motor

Description	Benchmark motor data	Requirement for new motor
Rated Power	800W	1200W
Rated Speed	500 rpm	600 rpm
DC bus voltage	48 V nominal	48 V maximum
Casing outer diameter	180 mm	155 mm
Casing axial length	110 mm	110 mm
Weight	8 kg	7 kg
Peak Torque[a]	54 Nm	85 Nm
Peak Torque density[a]	6.75 Nm/kg	12.14 Nm/kg
Power density	100 W/kg	171W/kg

a Peak torque density for 60 sec

4.2.2. Design methodology

It is not known a-priori whether the short-duty torque specification can be achieved. Based on the vehicle geometry, the dimensional constraint is considered as a hard constraint. Hence the design problem is framed as a category 2 i.e. fixed volume problem. Since weight minimization is another objective for reducing the wear and tear of suspension, weight is set as the second objective. Since a major component of the cost is from relatively expensive NdFeB magnets, cost minimization is set as the third objective for optimization. Test data of the prototype machine is used for validating assumptions and calibrating the thermal model.

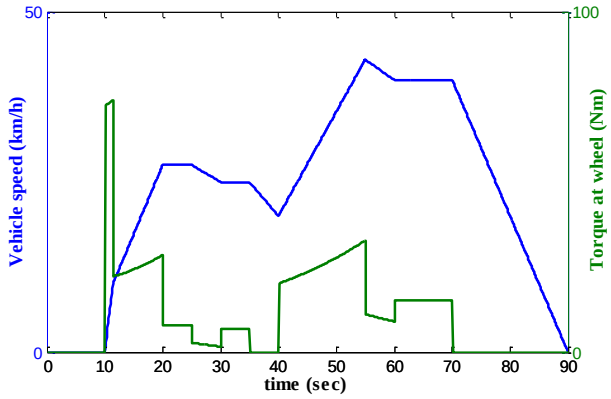

Figure 25 City drive cycle profile considered for the design study

4.3. Construction of the bar-conductor tooth-wound stator

4.3.1. Justification for using semi-closed slots

For machines that operate at low frequencies, bar conductors can be formed into coils and inserted radially through the wide slot openings. However, increase in slot opening of the motor induces eddy currents in stator conductors [68, 73]. It is substantial

if the conductor is not stranded. Some portion of main magnetic flux from the permanent magnet enters the conductor which is at top of the slot.

(a)

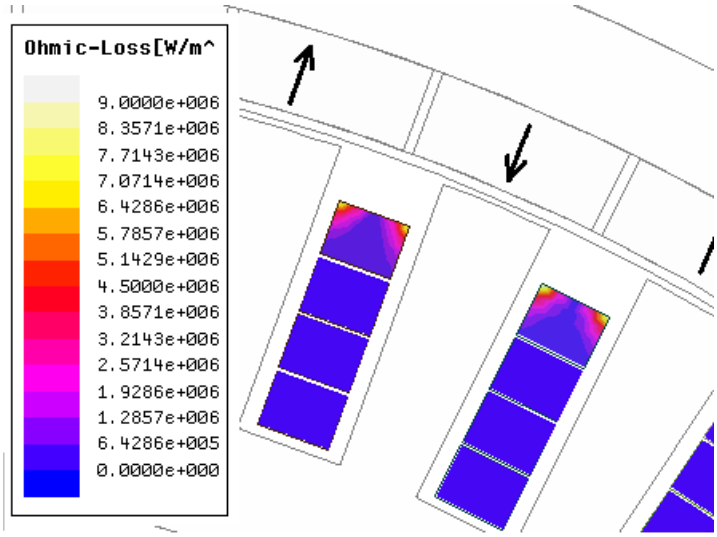

(b)

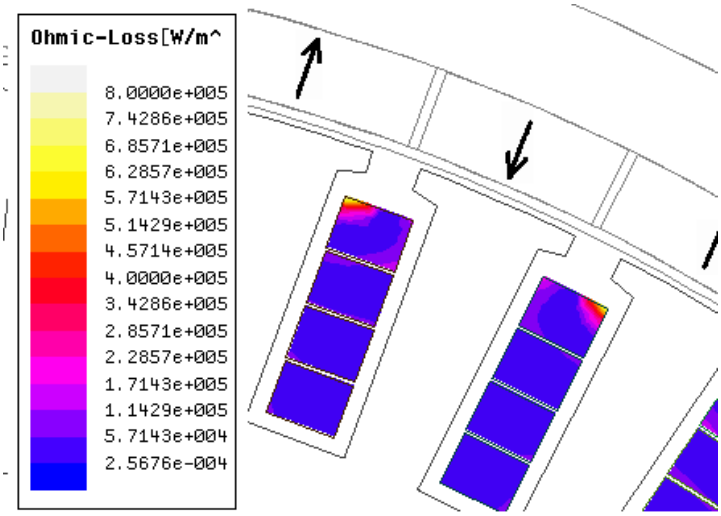

Figure 26 Loss density distribution due to magnet-induced eddy currents in conductors (a) open slot construction and (b) semi-closed slot. Note that the scales are different for the two shaded plots

Figure 26 shows the eddy current density in the rectangular conductors for fully open slot condition while motor is running at rated speed of 600 rpm and a frequency of

300 Hz. Despite a deeper than required slot, the eddy loss is found by transient FEM to be to be significant at 262 W for a motor rated for 1.2 kW and is mainly concentrated in the top conductor. With semi-closed slots, this loss is reduced to 16 W. In addition to reduction of these eddy losses, semi-closed slots will have better Carter coefficient. Fabrication method and construction are described in next two sub-sections.

4.3.2. Fabrication method

The fabrication of such a type of winding has two stages: insertion of conductors, and winding interconnects. These are described here.

Insertion of conductors

As discussed earlier, the idea of this type of winding is to have a semi-closed slot with tooth-wound bar conductors. Since the dimensions of conductors are larger than the slot opening, each individual turn has to be inserted axially through slot ends. Individual conductors are bent to U-shape or hairpin as shown in Figure 27(a) and (b) respectively. The bent conductors are then inserted into the slot from one side of the stack. This side does not have any interconnects as seen in Figure 24. On the other side of the slot, conductors are bent to bring together the ends that should be welded. The biggest challenge in achieving the calculated conductor fill is the geometric tolerance of bending operation. If the bent conductor has kinks or if the bend is elastic and the bar tries to restore its shape after bending, insertion becomes difficult and excess force used or insertion may result in scratching of insulation. Due to such factors, precision bending and insertion are critical.

Winding interconnects

There are two types of connections: inter-turn connects and jumpers for connecting phase belts. A phase belt is a set of adjoining set of slots that contain conductors belonging to a particular phase as shown in Figure 28. The total number of welds (N_{welds}) is equal to the number of conductors. If the next coil in series lies in the same phase-belt, then a jumper is not required. Thus longer phase belts mean smaller number of jumpers (N_{jumper}), but also lower periodicity. For example a double layer (DL) 10-pole 9 slot motor would have single phase belt and hence no jumpers, but an unbalanced force on the rotor, whereas DL 10-pole 12 slot motor would have a periodicity of 2 and hence 2 jumpers for each phase.

$$N_{welds} = \frac{N_s n_t}{2}, \quad N_{jumper} = N_{ph} \cdot (gcd(N_p, N_s) - 1) \tag{53}$$

The natural choice is to select this topology for a design that requires a smaller k_e because increasing k_e comes at the penalty of increased number of welds and connections by increasing n_t or *SW*. At the same time, smaller k_e would mean greater losses in lead wires due to larger supply current. The choice of number of slots is also restricted based on conductor size for ease of bending. Though manual welding process is time consuming, it can be easily automated as weld positions are fixed due to precision shapes of conductors.

(a) (b)

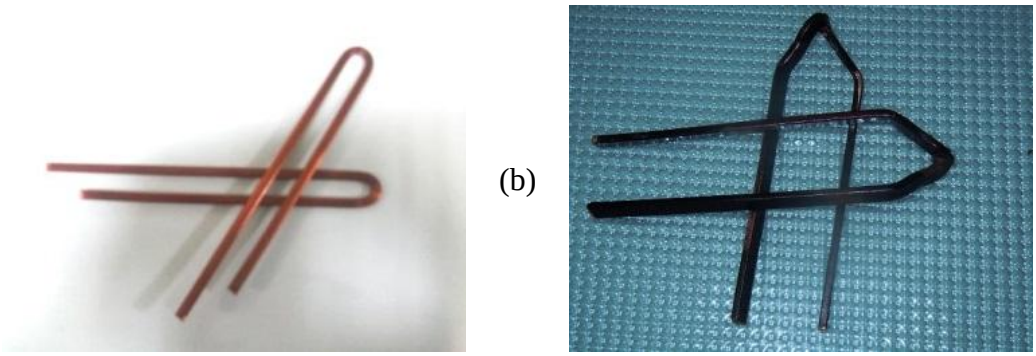

Figure 27 Individual stator conductors formed for axial insertion (a) bend for SL FSCW and (b) hairpin for DL FSCW or distributed arrangement

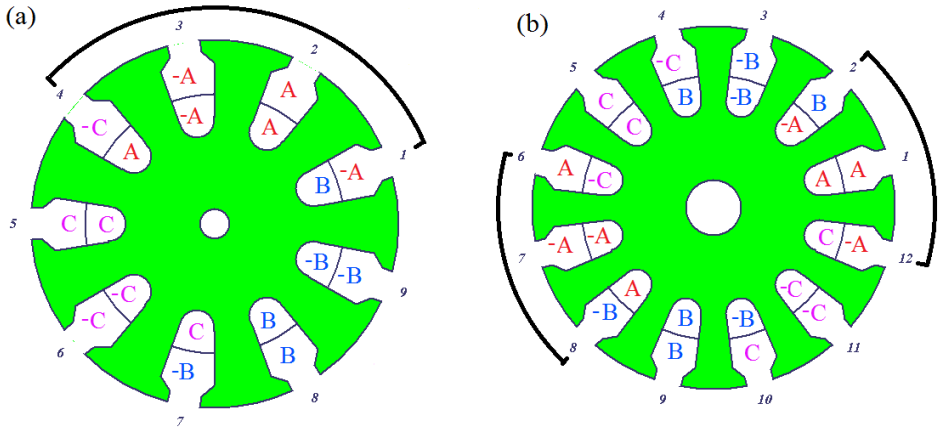

Figure 28 Phase belts for tooth wound windings (a) Single phase belt for 10 pole 9 slot winding, and (b) two phase belts for 10 pole 12 slot double layer winding

4.3.3. Conductor arrangements and geometries

The fabrication process described above allows for several different types of winding constructions and geometries for FSCW arrangements. The advantages and manufacturing details arising out of different choices are discussed here.

Single layer vs. double layer arrangements

Single layer and double layer windings present different types of tradeoffs in terms of space harmonics, leakage and winding factors [74]. The construction aspects of these configurations relevant to bar-wound arrangements are discussed here. For rectangular conductors, stator teeth will be non-parallel and the angle between the two edges of each tooth will be $360°/N_s$.

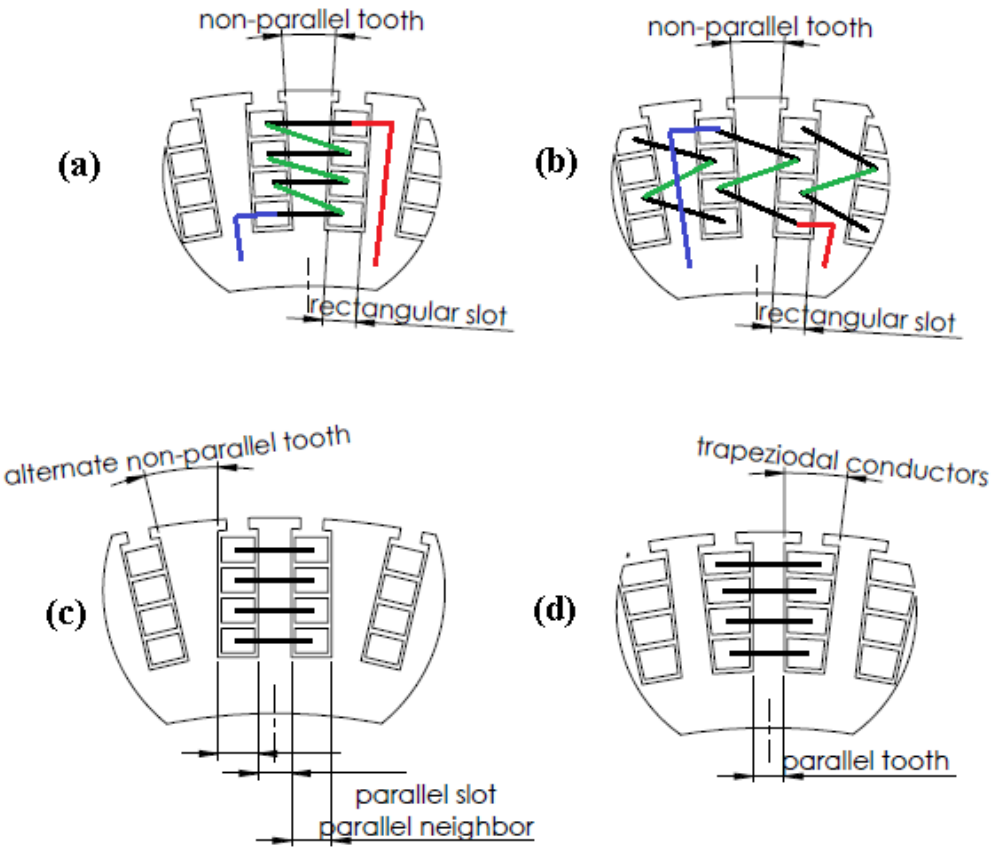

Figure 29 Conductor arrangements, slot shapes and connections for (a) SL parallel slot non-parallel tooth, (b) DL parallel slot non-parallel tooth, (c) SL parallel slot, alternate parallel tooth and (d) SL parallel tooth non-parallel slot

In case of SL windings, all bends in a coil pass through the same two neighboring slots as seen in Figure 29 (a). The end-turn of the bend is shown in black and the weld is indicated in green color. The two ends of each coil are indicated by blue and red, which are connected to the next coil by using jumpers. In this case, each bend is in the shape of a U (Figure 27 (a)) and occupies the same relative position in both slots. Note that it is possible to have odd number of conductors in each slot for a single layer (SL) winding. In DL windings, each bend goes from a bottom position to one position above as shown in Figure 29 (b). This is necessary to avoid overlapping of welds on the other side. The bend appears like a hairpin in this case as can been seen in Figure 27 (b).

Single layer with identical conductor bends

The examples shown in Figure 29 (a) and (b) show the use of same rectangular conductor size for each turn. However, each bend has different dimensions and needs additional effort with separate bending and welding fixtures. Since all the bends belong to the same neighboring slots in SL arrangement, all bends can be made equal by having alternate rectangular teeth. This is the least complex arrangements described in this paper. The prototype motor uses this arrangement of slots and conductors. In this case, however, the edges of non-parallel teeth have a larger angle of $720°/N_s$ and a larger concentration of flux at the bottom of these teeth. This requires careful magnetic design of the stator geometry.

Single layer with different conductor sizes

Since each bend is separate from the next turn during assembly, SL configuration presents an interesting possibility of unequal conductors, i.e. unequal conductor heights

for construction of Figure 29 (a) and (c) or trapezoidal conductors as in Figure 29 (d). It is important to note that manufacturing of such constructions require custom extrusion of bar-conductors for each bend and may be used in applications that justify the additional manufacturing costs.

4.4. Thermal design considerations

The motor requirement in the design specification is based on a typical drive cycle. The motor operates repeatedly through the drive cycle, and under such a scenario, when the motor is already heated up to a certain operating temperature, the vehicle should still be capable of delivering the peak torque for 60 sec. Thus the peak torque capability calculation involves two steps: first to estimate the motor thermal state under repeated drive cycle operation. Under this condition, the PM remnant flux density is weakened due to elevated temperature, copper resistivity is increased and the margin between continuous operating temperature and hotspot temperature is reduced. The second step is to estimate the peak capability such that hot spot temperature in windings does not exceed rated insulation class temperature. These effects are modeled with the help of a simplified equivalent circuit of the motor.

4.4.1. Simplified thermal circuit of the motor

The thermal behavior of the motor is modeled with the help of a detailed lumped parameter thermal circuit as shown in [42, 75]. This detailed circuit can be simplified based on certain assumptions and observations on a prototype motor (details of tests are presented in section 4.8. It is observed that the temperature difference between the annular casing, the side covers and the PMs is less than 1 °F during steady state and

transient thermal conditions. So the entire rotor is considered as a single element in the lumped circuit. The temperature measured at the two ends of the shaft is equal. Therefore, the shaft is treated as one element and an additional symmetry condition is imposed. The elements C^{θ}_{Cu}, C^{θ}_{ir}, C^{θ}_{ca} and C^{θ}_{sh} denote copper, stator core, casing and shaft capacitances.

This simplifies the thermal equivalent circuit to that of Figure 30. Estimation of thermal resistances in Figure 30 relies partially on empirical relations developed in prior publications and on static tests carried out on a prototype motor. These are described in Table 7. The current sources P_{core} and P_{PM} in the circuit are fixed during repeated drive cycle analysis while P_{Cu} is dependent on copper and casing temperatures to account for effect of increased copper resistivity and decreased PM strength.

Since the outer diameter and axial length are fixed for the design problem, the thermal resistances $R^{\theta}_{ca\_am}$, $R^{\theta}_{bearing}$, $R^{\theta}_{ir\_sh}$, and $R^{\theta}_{sh\_am}$ will be exactly same across all designs. The thermal resistance of R^{θ}_{gap} will vary depending on stator outer diameter and stack length. This variation is expected to be within a range of 10% of its mean value. The only thermal resistance sensitive to design is $R^{\theta}_{cu\_ir}$. The calculated and estimated values of these thermal resistances (presented in section 4.8) based on prototype motor are used in fitness function thermal model.

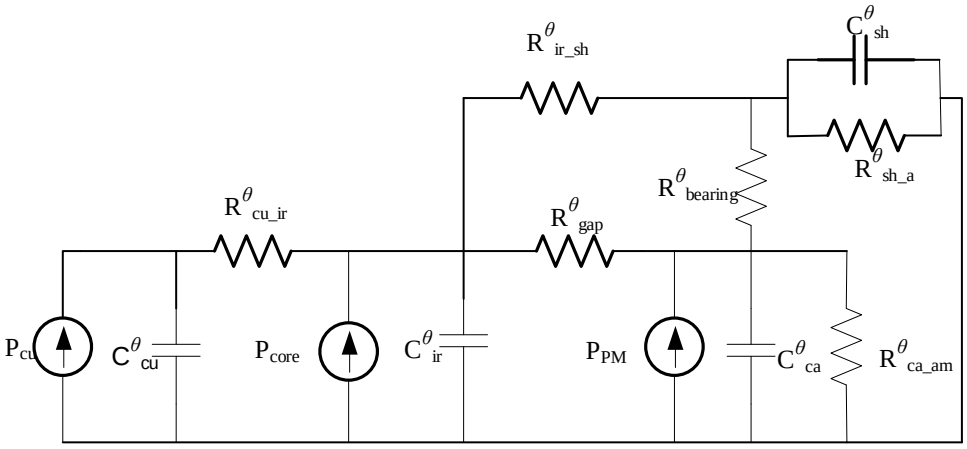

Figure 30 Simplified thermal circuit considered for study of thermal profile

Table 7 Thermal resistances and heat capacities in the simplified thermal circuit of the motor

Symbol	Description	Method of calculation
$R^{\theta}_{cu\_ir}$	Conduction thermal resistance between copper and stator core	Thermal FEA considering 'goodness factor' of impregnation
R^{θ}_{gap}	Heat transfer resistance between stator and rotor through air	Air-gap heat transfer assumed due to conduction only with temperature dependant air conductivity. End-windings to side cover heat transfer through convection.
$<R^{\theta}_{ca\_am}>$	Casing to ambient heat transfer resistance (averaged for heat transfer over a cycle)	Combination of natural and forced convection based on dimensionless laminar flow equations [76], based on (3)
$R^{\theta}_{ir\_sh}$	Thermal resistance between stator core and shaft	Calculation sensitive to interface gap between stator and shaft as well as heat transfer between laminations. Determined by curve fit of experimental test data.
$R^{\theta}_{sh\_am}$	Thermal contact resistance between shaft and mounting chassis	This parameter is sensitive to interface gap of mounting and hence determined by curve fit of experimental test data.

The maximum speed of the machine is 600 rpm and the dimensionless Taylor number in air-gap is well below 40. Therefore it is assumed that air-gap heat transfer is

due to conduction only (radiation heat transfer is found to be negligible). The heat transfer between the rotating casing and ambient is calculated using forced convection correlations [75].

The temperature rise with time for a specimen design is based on a typical CDC for 1.2kW vehicle. The speed profile of CDC and required acceleration is shown in Figure 25. The equations arising from the repeating drive cycle heat transfer at the casing is given in (3). T_{ca} and T_{am} are casing and ambient temperatures, P_{loss} is total loss, t_{cycle} is drive cycle period.

$$T_{ca}=T_{am}+\frac{\int_0^{t_{cycle}} P_{loss}(t)dt}{\int_0^{t_{cycle}} \frac{1}{R^{\theta}_{ca\_am(t)}}dt} \tag{54}$$

4.4.2. Thermal conduction resistance between copper and stator core: bar-wound vs. multi-stranded stators

Numerical computation of thermal conduction resistance between copper and stator core

For a known geometry and well defined material properties, the thermal resistance between winding and stator can be found by a linear thermal FEM [77]. However, the main issue is determining the conductivity of impregnation due to presence of air pockets and incomplete fill of impregnation. Authors have attempted to quantify the thermal contact quality by introducing “goodness factor” of impregnation in [45]. ‘Goodness factor’ is ‘1’ if the slot area (other than winding and slot paper) is filled completely with impregnation and it is ‘0’ if it is filled completely with air. It is found in [45] that the goodness factor of impregnation lies between 0.4 and 0.5 for dip

impregnated multi-strand stators and it improves with conductor fill. In mass production, the mean impregnation goodness factor and its standard deviation will depend on the process adopted for impregnation. To find the thermal resistance between conductors and stator for one slot, the slot geometry is created as shown in Figure 31. Constant temperature boundary is applied to the sides of the slot, thus considering the stator to be a lumped system at uniform temperature. Two definitions of thermal resistance are adopted (55), (56):

$$R^{\theta}_{\mathrm{Cu\_ir\_hotspot}} = \frac{T_{\max}}{\sum \rho_{\mathrm{Cu}} J_c^2 A_c} \tag{55}$$

$$R^{\theta}_{\mathrm{Cu\_ir\_mean}} = \frac{T_{\mathrm{Cmean}}}{\sum \rho_{\mathrm{Cu}} J_c^2 A_c} \tag{56}$$

Here T_{max} and T_{Cmean} is the maximum and mean copper temperature in the slot found by thermal FEM.

$R^{\theta}_{cu\_ir\_mean}$ is used in the lumped parameter thermal circuit to compute the increased phase resistance due to heating in loss calculations. $R^{\theta}_{Cu\_ir\_hotspot}$ is used for computing thermal limit on torque capability.

4.4.3. Comparison of bar and multi-strand windings

This analysis for comparable geometries of bar-wound and multi-strand slots is presented here. The total copper area and the loss are kept same for the two cases and a current density of 12 A/mm2 is applied to the conductors in both cases. The varnish conductivity of 0.13 W/m/°C is used in both cases. Slot liner thickness is assumed to be 0.25mm with a thermal conductivity of 0.1 W/m/°C and wire insulation is assumed to be NEMA single build of 40µm with a thermal conductivity of 0.26 W/m/°C.

In this analysis, the goodness factor is swept between 0 and 1 for the cases of bar-wound and multi-stranded conductors. The variation of contact resistance with goodness factor is studied by thermal FEM for the two cases and as can be seen in Figure 32. Though statistical evidence of impregnation goodness factor for the two cases is not available, clearly bar-wound arrangement has lower contact resistance.

Additionally, multi-stranded conductor stators have more impregnation area in the slot owing to low conductor fill. The impacts of high conductor fill and better impregnation goodness can be seen by significant reduction in hot-spot temperature of windings in the slot. This is illustrated by a thermal FEA temperature shaded plot of Figure 31. The ratio $R^{\theta}_{Cu\_ir\_hotspot}$ and $R^{\theta}_{Cu\_ir\_mean}$ is higher for multi-strand case at 1.39 as compared to bar-wound which is1.14. For the application of interest in this paper, short duty torque overload happens at low speeds. However, if overload at high speed (high frequency) operation is of interest, then ac loss in case of bar-wound geometry should be applied in this analysis for fair comparison between the two conductor types.

This method of computing $R^{\theta}_{Cu\_ir}$ is sensitive to conductor placement in slot. Conductors are placed equidistant from both slot edges in Figure 31(b), which is the worst case scenario for computing $R^{\theta}_{Cu\_ir}$. For any other horizontal position of conductors, $R^{\theta}_{Cu\_ir}$ would be smaller. For multi-strand case of Figure 31(a), the worst case conductor placement is when all conductors are crowded in the center of the slot.

4.4.4. Impact of $R^{\theta}_{Cu\_ir\_hotspot}$ on short duty overload capability

During the short duty 60 sec peak overload, windings of the motor experience 10-20 times the nominal (average of drive cycle) copper loss. The time interval of 60 sec

is such that it is comparable to the time constant $R^{\theta}_{Cu\_ir}C^{\theta}_{ir}$, but much smaller than the time constant of $R^{\theta}_{gap}C^{\theta}_{ca}$ or $R^{\theta}_{ir\_sh}C^{\theta}_{sh}$. For a typical design, out of the additional 150 kJ of heat generated during overload, 70 kJ is transferred to stator and only 5 kJ is transferred to shaft and casing. Thus the overload capability strongly depends on $R^{\theta}_{cu\_ir\_hotspot}$, C^{θ}_{Cu}, C^{θ}_{ir}.

The contact resistance $R^{\theta}_{Cu\_ir\_hotspot}$ (hence hot-spot temperature) can increase drastically in case of a bad sample with low goodness factor multi-strand winding and will be still under acceptable limits for the high conductor fill bar wound stator as seen in Figure 33. The torque constant (phase-peak) is assumed to be 0.24 Nm/A for both cases, and the motor is delivering 70 Nm torque. The conductor area is same for the two cases while the weight of stator core is increased in case of multi-stranded winding due to requirement of deeper slots.

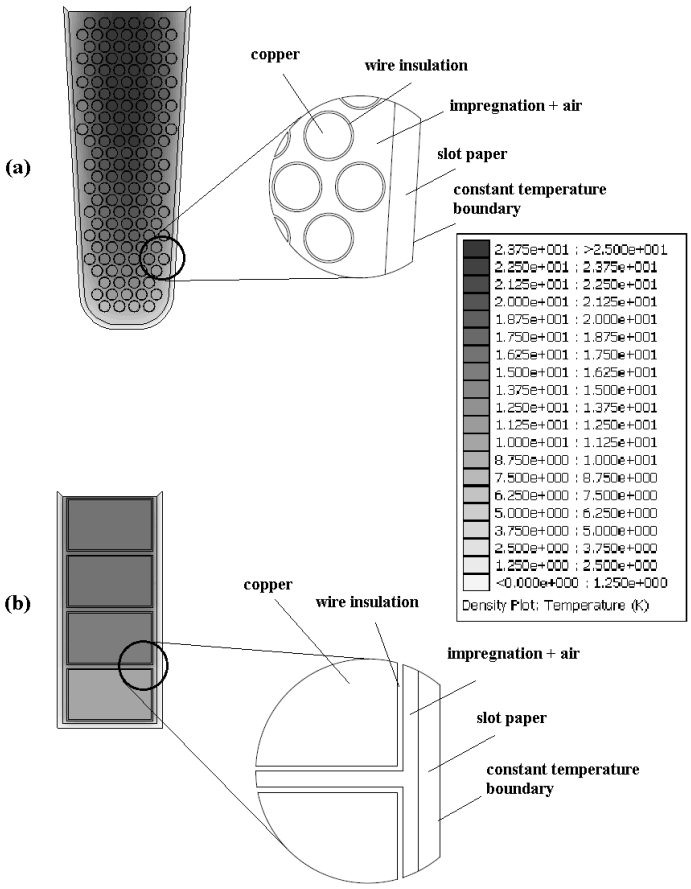

Figure 31 Thermal FEA to determine the hot-spot temperature rise in slot for (a) multi-strand bundle wound slot and (b) bar-wound slot. The copper area and current density are same in both cases

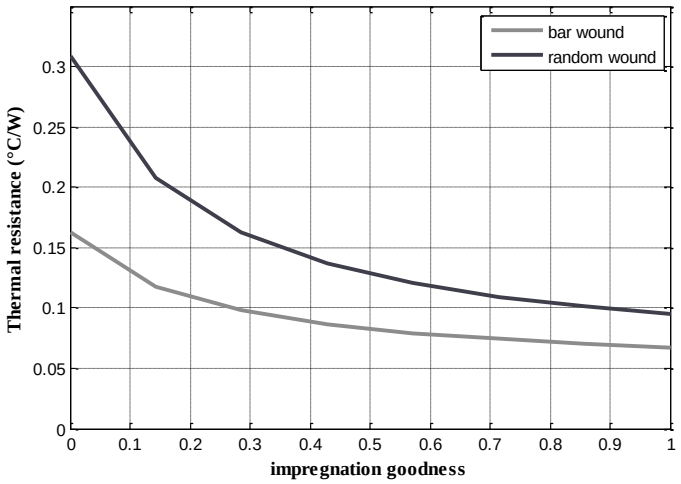

Figure 32 Variation of hotspot thermal contact resistance for the two slots with impregnation goodness for the same copper area

It can be argued that for normal operating condition, if the same copper area is achieved using multi-strand conductors by increasing the slot dimensions, the resultant temperature rise may not be significantly higher than bar windings for continuous operating case. However, the gains in terms of short duty peak capability are significant. Due to the more tightly packed slot, higher copper area in slot can be achieved, compounded by increased copper thermal capacity would result in much higher short duty torque capability for bar-wound conductor designs. This is studied in next section

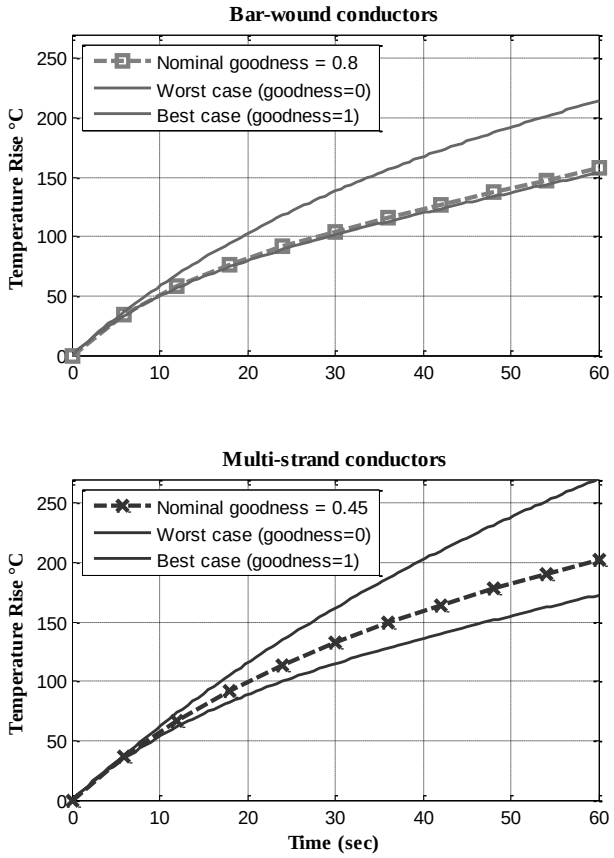

Figure 33 Comparison of winding hotspot temperature response to an overload torque under identical copper area and torque constant and different winding contact resistance

4.5. Multi-objective optimization

4.5.1. Design problem formulation & geometry description

Based on the specification presented in section 4.2, the design optimization problem is formulated. The objectives, constraints and design parameters of the optimization are given in Table 8. Identical problem formulations and materials are used for bar-wound case and multi-stranded case. The set of parameters for description of slot

geometry is the only difference for the two cases. Some of the geometric parameters are depicted in Figure 34.

A wide range of pole-slot combinations are included in the search space. All valid combinations with slot numbers between 24 and 84 that are multiples of 6 and pole count that yield winding factor greater than 0.9 are included. Choice of slot-pole combination is encoded as a discrete design parameter. Other geometric parameters are encoded so that no invalid designs are generated while ensuring that the search space spans most feasible designs. Materials chosen for the design are: M19 grade silicon steel and N35SH grade NdFeB PM's with a remnant flux density of 1.15T and relative permeability of 1.06 at 20°C.

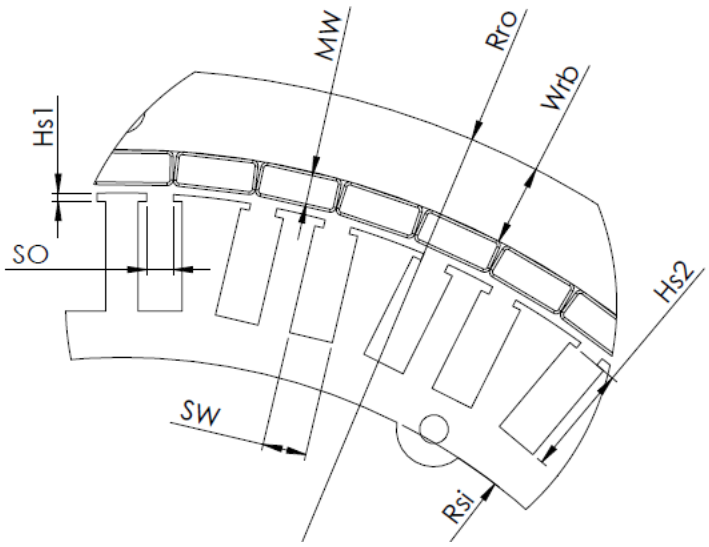

Figure 34 Description of some of the geometric design parameters of the motor

Table 8 Formulation of the Design Optimization Problem

Objectives		
Cost of active materials (minimize) Mass of active materials (minimize) Short duty torque capability (maximize)		
Constraints		
Symbol	Description	Limits
R_{ro}	Rotor outer radius	R_{ro}=75 mm
l_{ax}	Total stator length (including end-windings)	l_{ax}=85mm
T_{ins}	Maximum Insulation temperature	T_{ins}<220°C
W_{sb}	Stator back-iron width	$W_{sb}\geq$4 mm
Design parameters		
(Ns, Np)	Slot-pole combination	$30\leq N_p\leq 76$ $24\leq N_s\leq 84$, N_s is a multiple of 6
h_M	Magnet thickness	$2\text{mm}\leq h_M\leq 4\text{mm}$
W_{rb}	Rotor back-iron thickness	$3\text{mm}\leq W_{rb}\leq 8\text{mm}$
SW/TW	Slot width (for parallel slot), tooth width (for parallel tooth configuration)	$3\text{mm}\leq TW\leq\frac{\pi(R_{so}-H_{so}-H_{s1})}{N_p}$
SO	Slot opening	*SO*=3mm for multi-stranded $1\text{mm}\leq SO\leq SW/2$
Hs0	Tooth tip height	$0.5\text{mm}\leq Hs0\leq 2\text{mm}$
Hs1	Tooth wedge height	$0.5\text{mm}\leq Hs1\leq 1.5\text{mm}$
Hs2	Slot Depth	$5\text{mm}\leq Hs2\leq Hs2\_max$
layers	Winding layers	Single, Double

4.5.2. Design optimization

The optimization is performed by multi-objective Genetic Algorithm (GA). The GA is programmed to optimize using a population size of 200 over a fixed number of 20 generations

4.5.3. Fitness function

The problem formulation is a combined category 2 and category 3 problem discussed in section 3.8.3 and the evaluation algorithm of Figure 22 is followed for both the cases of multi-stranded and bar-wound configurations. The short duty and

continuous operation thermal phenomena are modeled as described in previous section along with calibrated prototype data of section 4.6.

For calculating the active material cost, the following formula is used:

$$cost = 9.6 * m_{wire} + 2.42 * 4k_{stk}R_{ro}^2 l_{stack}\rho_{Fe} + 78 * m_{PM} \quad (57)$$

where m_{wire} is the mass of copper in kg, k_{stk} is the stacking factor, ρ_{Fe} is the density of silicon steel, and m_{PM} is the mass of chosen grade of NdFeB magnets in kg.

The conductor fill for the multi-stranded stator is found to be 42% from an in-production sample. The inter-strand distance is computed for a hexagonal packing of strands from the dimensions of the sample and the conductor fill for each candidate design is computed by populating the slot with the same strand size and strand spacing.

4.5.4. Optimization results

The pareto-optimal sets for the 3-objective optimization for each case of bar-wound FSCW and multi-stranded stators are plotted in Figure 35. Bar-wound designs show a significant improvement in torque capability for the same weight or same cost as compared to the designs with multi-strand windings. Lower weight designs are possible due to less core material owing to shallow slots for the same copper. The biggest cost component in this design is the permanent magnets, which is not a part of the stator. Despite this fact, lower cost of bar-wound construction is possible due to higher loading or better utilization of the magnets. It is observed that the PM's are well within safe limits of demagnetization in spite of the high overload current. The maximum magnet thickness h_M is less than 2.64 mm for bar-wound and 2.43 mm for multi-stranded designs, though the upper bound on the h_M search space is 4 mm. Several designs with

h_M = 2mm are in the pareto-sets. This means despite the high short duty capability of the designs, the PMs are still far from demagnetization limit and under-utilized.

The slot number of each design in the Pareto-sets is shown by a greyscale shade. It can be observed that the distribution of slot-number in the two sets is different. Higher torque designs can be achieved using higher slot numbers (54-60) in bar-wound designs whereas slot number of 48 is favored most for multi-stranded designs. It can also be observed that low slot-number designs (30-36) offer a small cost advantage over higher slot-number designs, but at a huge weight penalty for both constructions. Thus the conflicting nature of objectives is verified.

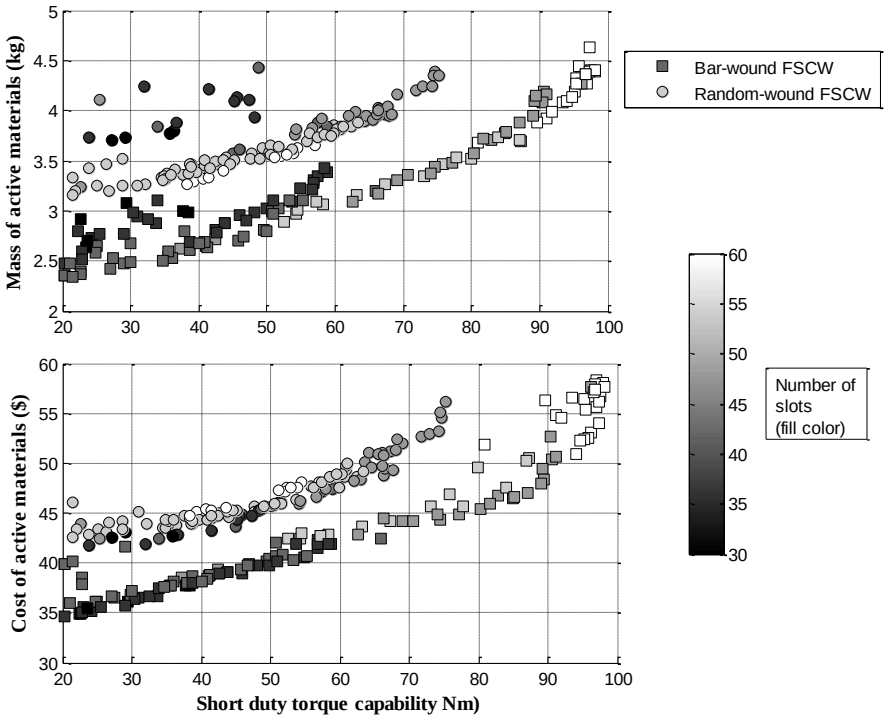

Figure 35 Comparison of the Pareto-optimal sets derived for the two cases of bar-wound FSCW and stranded FSCW stators

4.6. Prototype construction and tests

A prototype motor is built for understanding the fabrication aspects and for validation of the proposed construction. The details of the 54 slot 60 pole motor are given in Table 9. The prototype motor is experimentally evaluated for no load losses, dc- and ac- resistance, thermal contact resistance test, and efficiency under different load conditions.

4.6.1. Design details of the prototype motor

In addition to the fixed parameters, constants and constraints described in Table 8, the details of the prototype motor can be derived from the parameters of Table 9.

Table 9 Prototype design data

Prototype design parameters		
(Ns, Np)	Slot-pole combination	*Np*=60 *Ns*=54
h_M	Magnet thickness	h_M=3mm
Wrb	Rotor back-iron thickness	*Wrb*=4mm
SW	Slot width	*SW*=3.6mm
SO	Slot opening	*SO*=2.3mm
Hs0	Tooth tip height	*Hs0*=1mm
Hs1	Tooth wedge height	*Hs2*=0mm
Hs2	Slot Depth	*Hs2*=8.6mm
layers	Winding layers	Single layer with alternate non-parallel tooth and parallel slots

4.6.2. Preliminary tests

Back-emf constant, dc resistance and no-load loss

The phase-peak back-emf constant is found to be 0.24 Vs/rad, which is very close to value of 0.25 Vs/rad computed by FEM. The calculated phase dc resistance is

25.4 mΩ and the measured resistance is 27.2 mΩ. Therefore it is concluded that 36 welds and 18 bends in each phase do not affect phase resistance significantly. The no-load test gave a resistance torque (bearing friction + hysteresis) of 0.7 Nm at low speed and an eddy current loss of 15 W at rated speed. Thus the total no load loss was 59 W at 600 rpm. This measurement was performed without the gear assembly of Figure 39.

Measurement of ac resistance

The ac-resistance of windings is caused purely by slot leakage fluxes due to winding currents. Hence, the rotor is removed while performing this test to accurately measure ac loss without the need to estimate other loss components such as mechanical losses or eddy losses in magnets. A smooth sine current is applied to a pair of windings for different frequencies and ac-resistance is calculated based on the total loss in windings. The input power for the windings is measured using a power analyzer and ac-resistance is calculated based on the power dissipated for each frequency. The measured and calculated ac-resistance coefficients are plotted in Figure 36. Since the analytical formula for this calculation is an exact solution, the experimentally found and calculated values match closely except for measurement errors.

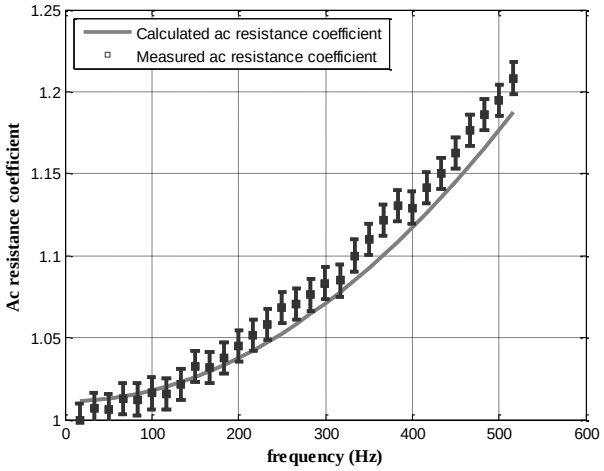

Figure 36 Experimental verification of eddy effect model for the prototype motor

4.6.3. Thermal tests

Short time static test for measurement of $R^{\theta}_{Cu\_ir\_mean}$

To determine the goodness factor of impregnation for bar-wound machines, a static experiment is performed on the prototype motor to measure the thermal contact resistance. By injecting a constant current for 60 sec in two of the phases, temperature rise in copper is measured indirectly by measuring the terminal voltage. The thermal capacity of copper and stator core is known from the measured weights of these components and the thermal resistance value that best fits the temperature rise is calculated as shown in Figure 37. from recorded data for the prototype motor.

The measured thermal resistance is 0.075 °C/W which corresponds to a hotspot thermal resistance of 0.085 °C/W. The goodness factor for this $R^{\theta}_{Cu\_ir\_hotspot}$ is approximately 0.6. The high goodness factor of impregnation in bar-wound was achieved by conventional dip impregnation process. Additionally, since bar windings are

precision formed, achieving better $R^{\theta}_{Cu\_ir}$ consistently is possible thereby increasing the reliability of such windings

Low speed constant current test

It is important to understand if the rest of the equivalent circuit has any impact on the short duty torque. Also, for determining the efficiency of the machine, thermal equilibrium condition needs to be computed. A constant sine current of 25 Arms is injected at a frequency of 2 Hz in the three phases of the machine. The rotor rotates at a low speed of 4 rpm. Casing temperature is recorded using an IR temperature sensor. The IR temperature sensor is calibrated against a K-type thermocouple to ensure accuracy. The stator windings are disconnected for 5 sec in every 10 mins to measure phase resistance to measure T_{Cumean} through phase resistance. Shaft temperature is measured using a K-type thermocouple.

The cooling of the casing is only due to natural convection at this low speed. The calculated convection coefficient is 10.2 W/m2/°C that yields an $R^{\theta}_{ca\_am}$ of 1.12 °C/W. The convection coefficient for winding to side-cover convection is found to be in the range of 20-40 W/m2/°C in several studies [76]. Assuming a convection coefficient of 30 W/m2/°C, and accounting for the air-gap heat exchange due to conduction yield an effective stator to casing thermal resistance R^{θ}_{gap} of 0.424 °C/W is obtained. $R^{\theta}_{bearing}$ is calculated to be 2.72 °C/W. $R^{\theta}_{ir\_sh}$ and $R^{\theta}_{sh\_am}$ are determined by curve fitting the temperature response recorded experimentally (as shown in Figure 38) to be 3.1 °C/W and 0.32 °C/W respectively. The shaft is relatively cooler and reaches a temperature of only 32.8 °C. The estimated values of interface gap between stator core and shaft is close

to 50 µm and between shaft and chassis mounting is close to 5 µm based on curve-fitted values of $R^{\theta}_{ir\_sh}$ and $R^{\theta}_{sh\_am}$. The equivalent circuit thermal resistances thus estimated were used for analysis in the fitness function.

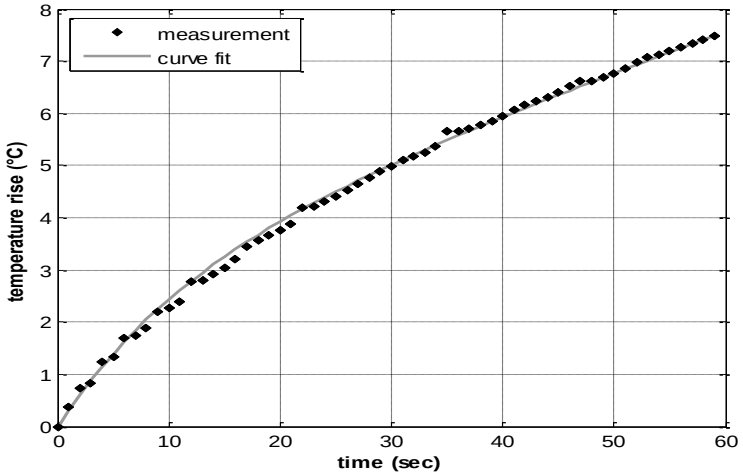

Figure 37 Short duration static test with 1 sec sampling time used to curve fit for $R^{\theta}_{cu\_ir\_mean}$

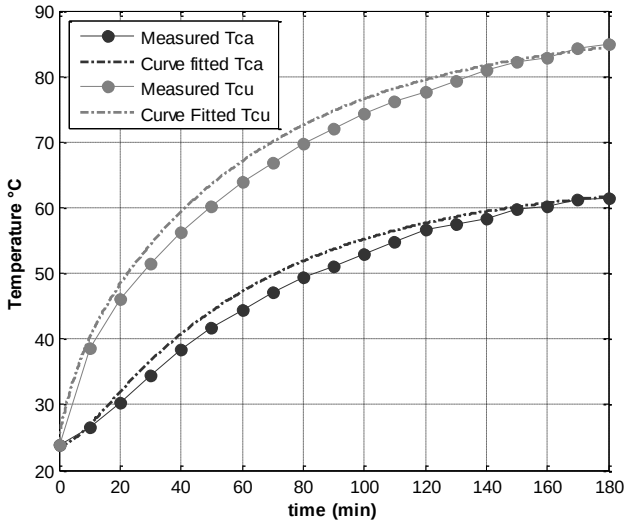

Figure 38 Measured and curve-fitted T_{Cu} and T_{Ca} for low speed constant current test

4.6.4. Load test

The test setup used for performing the load test is shown in Figure 39. The motor is coupled to the hysteresis brake by means of a helical gear. Load test is performed for the motor for a speed range of 100-420 rpm and torque range of 4-16 Nm. The modeled and measured efficiency plot is presented in Figure 40. Eddy current losses in PMs were modeled as proportional to $I_s^2\omega_r^2$. PM eddy losses computed by 2D FEA were 120 W against the separation of losses estimate of 30 W. Clearly, 3D FEA or advanced modeling techniques [56] are required to accurately account for end effects. The test set up uses 10:3 ratio helical gear arrangement to couple the test motor to load. The bearing and gear friction at no load measured 0.08 Nm on the high speed shaft, which was accounted for in efficiency measurement. However, helical gears are characterized by an axial thrust on bearings that is proportional to transmitted torque. This leads to additional losses at high torque regions of efficiency plot. Note that the load test is not performed under thermal equilibrium condition of the motor. Actual motor performance on a vehicle will be sensitive to its thermal state and environmental temperature.

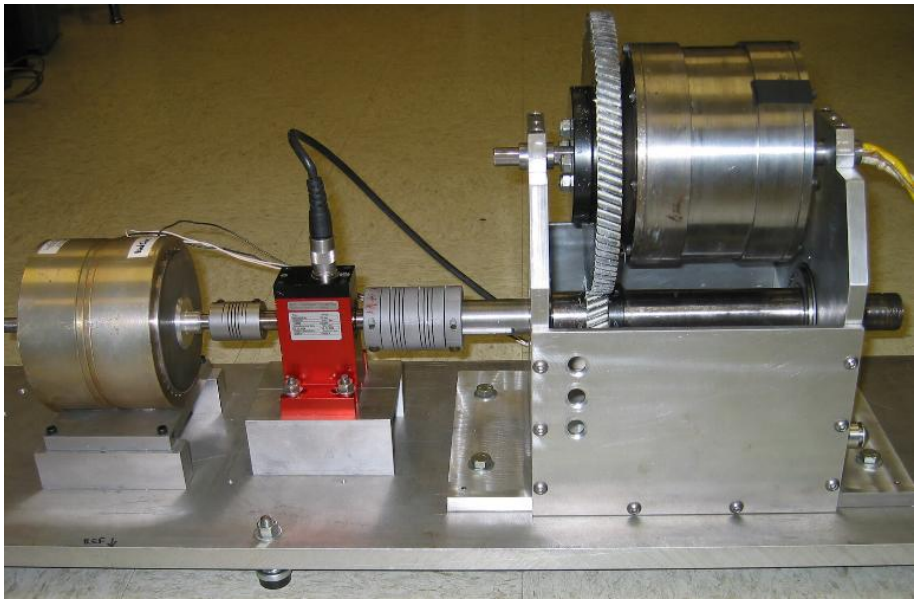

Figure 39 The test setup used to perform load test on the motor

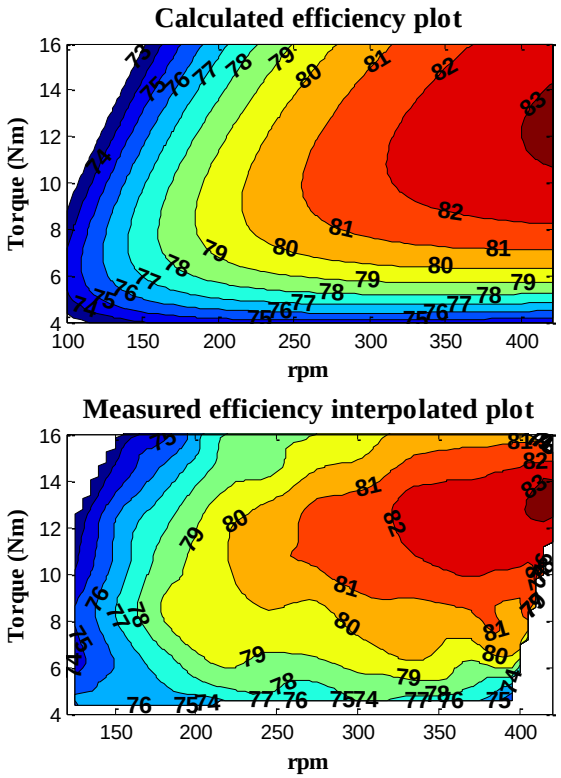

Figure 40 Calculated and measured percentage efficiency plots of the prototype bar-wound FSCW Motor

4.7. Conclusion

The use of solid conductor bar windings with application to single tooth-wound construction is studied for the first time to the best of authors' knowledge. Different types of winding constructions are presented for tooth-wound bar conductors with discussion on fabrication details. Analysis method is presented to determine the short duty torque capability of a machine and it is observed that this is highly dependent on thermal resistance between copper and stator and heat capacity of windings and stator. It is demonstrated from the analysis that bar-wound conductors are able to achieve a better thermal resistance between copper and stator iron as compared to multi-strand windings. Also this thermal resistance is less sensitive to quality of slot impregnation fill. This particularly helps in improving the short duty capability of the machine.

A detailed design optimization study is performed that assesses each design for temperature rise due to intended drive-cycle operation as well as short duty peak overload. It is observed that significant cost and weight benefits can be achieved by use of bar-wound FSCW stators as compared to conventional low conductor-fill multi-strand windings. Also, much higher torque capabilities can be achieved for the same volume.

5. DESIGN STUDY 2: OPTIMIZATION OF A NOVEL OUTER-SALIENT-ROTOR TOPOLOGY FOR GEARED DRIVE*

Electric motors are vital components of powertrains of electric and hybrid electric two-wheelers. The design of motor for this application is extremely challenging due to tight space and cost constraints. Three popularly used configurations of electric machines in mild hybrid two wheelers are shown in Figure 41. The IC engine crankshaft mounted configuration [78] is shown in Figure 41(a). The motor is designed for operation matched to the engine speeds (1-6 krpm) due to direct mounting. In another popular configuration of the in-wheel direct drive Surface-mounted Permanent Magnet (SPM) motor [32, 71] shown in Figure 41(b), the motor characteristic is matched to torque and speed requirements at the wheel (typically 300-1000 rpm). A third possibility is to use the mechanical arrangement of a geared in-wheel outer-rotor machine as shown in Figure 41(c), where the motor is designed to rotate at medium speeds (1-10 krpm) and a gear ratio is chosen to match the speed requirement at the wheel. In all these applications, the outer-rotor topology is preferred for cost reduction or ease of assembly, or for meeting a stringent space constraint. Other examples of applications where outer-rotor may be preferred topology are compressors, fans, etc.

For mechanical configuration of Figure 41(b), high pole count (28-60) outer rotor motors with high energy density surface permanent magnets [70, 71] are widely used for small (0.25 kW to 1.5kW) electric two wheelers. Rare-earth magnets are central to achieving such high torque densities. However, due to the uncertainty in prices of rare earth metals used in high energy density magnets, ferrite magnet based machines are preferred [79] for high volume cost-sensitive applications. This paper explores the design of Fa-SynRM medium speed motor for the same power capability as discussed in previous chapter that can be easily packaged along with a planetary gearbox (Figure 41(c)) in the same space as the in-wheel motor specification given in previous chapter. This paper proposes an inside-out two layer buried magnet rotor topology and presents a preliminary design study of the proposed outer-rotor Fa-SynRM for a practical application along with experiments on a prototype machine.

Study of rotor structures for buried magnet rotors has been of immense interest recently [34, 80, 81] with focus on improving torque and power densities as well as torque ripple reduction. In [79, 82], authors have studied IPM structures that are more suited for ferrite PMs to mitigate demagnetization under high current. It is evident that ferrite PM machines rely on achieving high saliency ratio for improvement in torque density. For low (<1krpm) and medium (1-10krpm) speed machines, torque density is further improved by using high pole count. For inner rotor structures, the notion of increased saliency ratio and higher pole count are conflicting and hence pole numbers only up to 8 are found in literature for buried ferrite machines. The aim of this paper is to show that by using two barrier outer rotor buried magnet structure, not only can

higher saliency ratios be achieved for higher pole numbers, but also that a good normalized magnet flux linkage to normalized d-axis inductance ratio (λ_{Mn}/L_{dn}) [5] (in the vicinity of 1) can be achieved despite using low power density ferrite magnets.

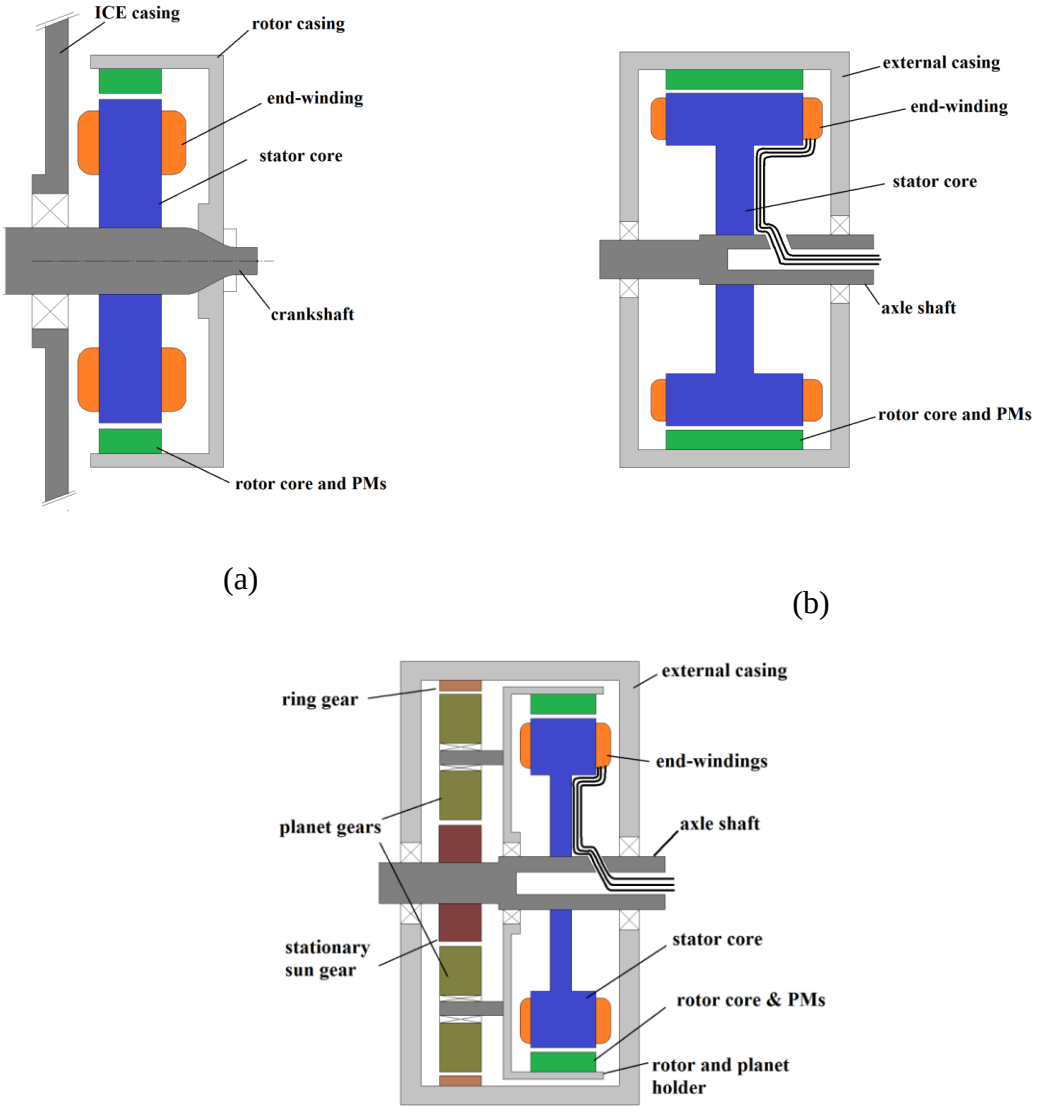

Figure 41 The mechanical arrangement for motors used in two-wheeler applications: (a) ICE crankshaft mounted, (b) in-wheel direct drive, and (c) in-wheel geared drive

Another advantage of outer-rotor IPMs is less PM flux leakage due to thinner bridges. In case of outer-rotor structures, the centrifugal forces generated by PMs are not transmitted by the bridges, but are exerted directly on the thicker core sections between barriers. Thus the bridge thickness can be minimum allowable based on manufacturing constraints. Additionally, higher efficiencies can be achieved due to absence of eddy current losses in ferrite PMs.

Specifications of the design problem and design objectives are described in 5.2. Structure of the outer-rotor buried magnet topology is presented in section 5.3. Section 5.4 presents the problem formulation and evaluation algorithm. Section 5.5 presents optimization results and details of four candidate designs. Section 5.6 presents details of the prototype motor and preliminary test results followed by conclusion

5.1. Definition of design problem based on vehicle requirement

In this paper, an outer rotating Fa-SynRM is designed for a 1.2 kW geared in-wheel drive as shown in Figure 41(c). The specifications for the target Fa-SynRM with planetary gear system are derived from key performance parameters of the vehicle and are given in Table 10 along with actual ratings of the benchmark direct drive motor. The Fa-SynRM is designed to achieve the rated power over the entire speed range, without specifying the actual speed of the rotor. The gear ratio is chosen so that the maximum speed of motor at rated power under field weakening ω_{max_motor} translates to maximum vehicle cruising speed. Thus the gear ratio is given by:

$$G = \frac{\omega_{\max\_motor}}{\omega_{\max\_wheel}}, \mathrm{G} < 10 \qquad (58)$$

The maximum gear ratio is constrained to 10 based on physical dimensions of the shaft and casing size. The continuous inverter capability of the benchmark SPM is decided based on rated power of 1.2kW at 600 rpm. This means that the continuous torque at all speeds is fixed to rated torque of 19.1Nm. A wide CPSR of the geared drive can, however achieve a larger continuous torque for the same inverter continuous rating. Thus, the maximum continuous torque at low speed is:

$$T_{max,cont} = G\frac{P_{rated}}{\omega_{\min\_motor}} = \left(\frac{P_{rated}}{\omega_{\max\_wheel}}\right) CPSR \qquad (59)$$

Since the quantity in the parenthesis is constant, the continuous torque capability at low speed is proportional to CPSR and hence CPSR is one of the design objectives. The multi-objective design optimization problem is defined to:

- Maximize Efficiency-Constrained CPSR (EC-CPSR) such that efficiency = 90% at ω_{max_motor}
- Maximize the average of motor efficiencies between ω_{min_motor} and ω_{max_motor} at rated power
- Maximize 60 sec peak torque capability at wheel (motor torque capability times gear ratio)

The external dimensions of the rotor stack are fixed and are given in Table 10. There is an additional constraint that the cogging torque < 0.2 Nm at the wheel. This is achieved by introducing an appropriate skew in stator. The dc-bus voltage is fixed at 48 V. The continuous peak output current rating of each phase is 32.7 A so that the inverter volt-ampere is rated at 1.5 kVA assuming a power factor of 0.8, but can be increased to achieve rated power. The switches have to be rated for the short-time peak current to match the motor's peak capability. The motor should produce required power at all

speeds within the CPSR without demagnetization of the magnets under peak torque operation for temperatures between -20°C to 100ºC.

Table 10 Design specifications for design studies 1 & 2

	Benchmark NdFeB SPM direct drive	Target: NdFeB SPM direct drive	Target Fa-SynRM geared drive
Outer Diameter	180 mm	150 mm	145 mm (Fixed)
Stack Length	50 mm	55 mm	30 mm (Fixed)
Rated Power	800 W at 500 rpm	1.2 kW at 600 rpm	1.2 kW at peak speed
Efficiency at max speed	80% at 800 W, 500 rpm	80% at 1.2 kW, 600 rpm	90% at max speed, rated power (constraint)
Conductor fill factor (bare conductor/bare slot area)	38%	>70% with rectangular conductors	45% with conventional winding
Continuous climbing capability	15.3 Nm	19.1 Nm (No Field Weakening)	19.1 Nm*CPSR (Objective 1)
Peak Torque (for 1 min)	54 Nm	Up to 100 Nm	120 Nm (Objective 2)
Average efficiency at rated power for speed range	67%	< 70%, not capable of producing rated power continuously below rated speed	>90% (Objective 3)

5.2. Outer rotor Fa-SynRM structure

Half pole of the proposed outer rotor structure with two-barrier geometry is shown in Figure 42. The outer rotor design proposed in this paper can be described as inverted (inside-out) version of the one presented in [80] but with barrier edges as arcs instead of straight lines. The outer layer can have magnet in the center arc as well as the fillet arc whereas the inner arc has magnet only in the center arc. The factors that affect the choice of number of barriers in the rotor structure are: size of the machine and limitation on the minimum thicknesses of PMs and core sections that can be manufactured. In this paper, two layer topology is chosen based on conclusion in [83]

that increasing the number of layers beyond two does not improve saturated saliency of the rotor.

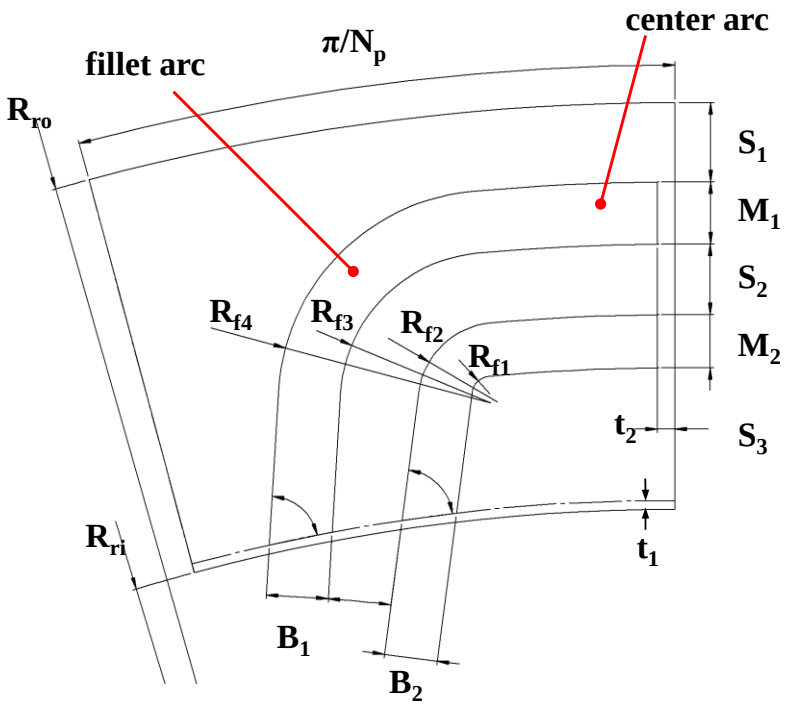

Figure 42 Half pole geometry of the rotor showing dimensions that completely define the half pole geometry

The geometry of the proposed rotor structure shown in Figure 42 is described by the parameters defined in Table 11. The design parameters used to define the geometry are chosen in a way that only valid designs are created for each combination of inputs. The construction of the geometry is based on certain relations and assumptions. The first assumption is that the gap between two adjacent poles is equal to 2S1 so that q-axis flux saturates evenly in the two bottlenecks. The second assumption is that the barrier width is constant i.e. B1=M1 and B2=M2. This is based on the observation in [84] that uniform

barrier width provides better protection against demagnetization of ferrite magnets. This also reduces the number of parameters and complexity for the optimization algorithm. The rotor inner to outer radius split ratio (SR) is chosen between limits:

$$SR_{min} = \frac{1}{1+\frac{\pi}{N_p}}, \qquad SR_{min} = 1 - \frac{2(M_{min} + S_{min})}{R_{ro}} \tag{60}$$

where M_{min} and S_{min} are the minimum barrier and core section widths.

For the purpose of optimization, the geometric dimensions shown in Figure 42 are derived by transforming parameter space based on relations of Table 11. The bridge thicknesses M1 & M2, and core section thicknesses S1, S2, and S3 are greater than 2.5 mm for manufacturability and mechanical strength. Figure 45 shows the rotor stack of the prototype motor. The nine parameters used for defining the geometry are given in Table 11. The fillet radii are chosen such that $k_{fil} = 1$ gives the maximum possible fillet radius for the chosen geometry for the outer edge of the outermost barrier and consequently *Rf3=Rf4-M1, Rf2 = Rf3-S2*, and *Rf1=Rf2-M2*. The bridge thickness (t_1) is chosen equal to the lamination thickness (0.35 mm) for manufacturability. The maximum speed of the Fa-SynRM is limited to 6 krpm, and hence the centerposts are not required due to relatively small centrifugal force.

5.3. Multi-objective optimization

Multi-objective Genetic Algorithm is used to optimize the FaRynRM to achieve the objectives defined in Section 5.2. This is again a combined category 2 and category 3 problem, however, differs from design study 1 because the operating speed of the machine is unspecified in the problem definition. An evaluation function that is very similar to Figure 23 is used with a slight modification in order to ensure that the

efficiency at maximum operating speed is met. In order to run it on a modest computation facility, the second iterative loop of the algorithm uses analytical calculations for estimating the maximum operating speed under field weakening. An additional step is included at the end to determine the maximum short duty torque for each design. It is observed that for this construction, the maximum current is limited by demagnetization constraint rather than thermal limit.

Optimization is carried out separately for different pole numbers using a population size of 80 over 20 generations for each case. Pole numbers from 10 to 16 are considered. Slot numbers that are multiples of 6 between 12 and 72 are considered. Both single and double layered windings are considered. Combinations of slot-pole and coil pitch that yield winding factor less than 0.9 are discarded. Only slot-pole & winding combinations with even greatest common divisor (gcd) are chosen so that unbalanced forces or unbalanced back-emf's are mitigated. Combinations of selected slot-pole and coil pitch are encoded into a discrete gene. The nine rotor parameters as described in Table 11 and three stator geometry parameters (slot opening, tooth tip height, and tooth width) are also included as design inputs for the optimization. The stator inner radius is assumed to be constant at 32 mm.

Since the design mandates that the cogging torque be extremely small, stators are skewed for all pole-slot combinations to eliminate cogging torque.

Table 11 Parameters used to define rotor geometry and parameter bounds used for design optimization

Symbol	Parameter description	Min value	Max value
SR	Split ratio = (Rri/Rro)	SR_{min}	SR_{max}
k_{ins}	Insulation ratio $(M_1+M_2)/(S_1+S_2+S_3)$	0.3	0.65
k_{M21}	Ratio of magnet thicknesses in the two barriers ($=M_2/M_1$)	0.6	1
k_{S21}	Ratio of core thicknesses in the two barriers ($=S_2/S_1$)	0.5	1
k_{S31}	Ratio of core thicknesses in the two barriers ($=S_3/S_1$)	0.4	1
k_{fil}	Fillet radius ratio (0= no fillet, 1=maximum geometrically allowable fillet radius)	0	1
α_{bar}	Angle between radial segment of the barrier and circumferential direction as shown in Figure 42	$\pi/4$	$\pi/2$
D	Decides if magnets are present in the fillet part of outer barrier	0	1

5.4. Multi-objective optimization results

The models proposed above are used to evaluate the fitness for maximizing the three objectives. Sets of non-dominated solutions for each pole count are presented in Figure 43. Basic performance metrics and characteristics of 4 candidate designs for 10, 12, 14 and 16 poles are presented in Table 12. These designs are selected from different regions of the final Pareto set.

Since this is the first of its kind study of outer-rotor PMaSynRM, several interesting conclusions can be drawn based on derived results. Relatively large saliency ratios (up to 3.2 for 12-pole) can be obtained for a higher pole number with two barriers in the proposed outer rotor topology. This topology can be employed for an outer rotor SynRM as well. Most designs in pareto set use 20-50% reluctance torque. Also, the λ_{Mn}/L_{dn} ratio of close to 1 or greater is achieved as seen from data of Table 12.

(a)

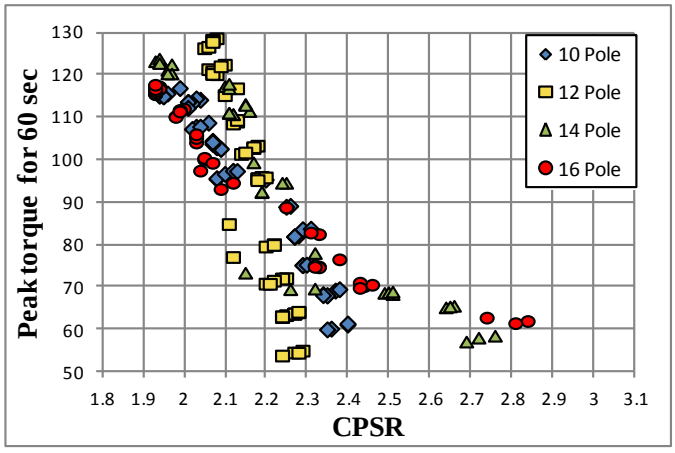

(b)

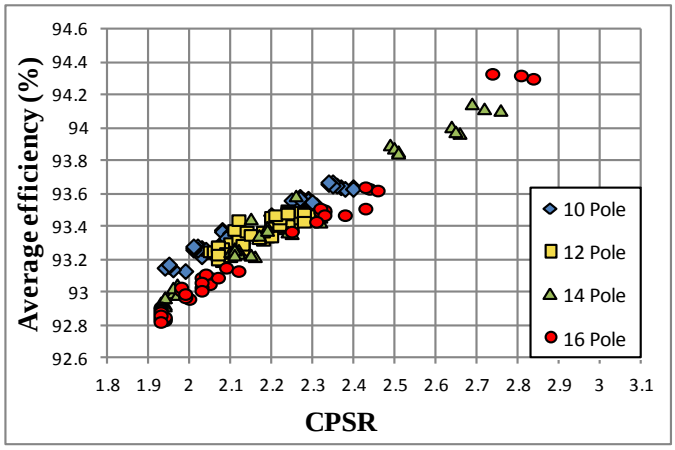

Figure 43 Non-dominated designs for different pole numbers after 20 generations for a population size of 80 for each set

It is observed that despite taking end-windings into account, for the selected objectives, there is no clear winner between distributed windings and single slot pitch concentrated windings. Distributed windings dominate due to their higher peak torque capability and resilience to demagnetization whereas single slot pitch winding motors showed larger EC-CPSR and better efficiencies for the chosen aspect ratio ($2R_{ro}/l_{stack}$) of the motor.

Table 12 Attributes of four specimen designs from the pareto-optimal sets

	Design 1 (proto)	Design 2	Design 3	Design 4
Configuration	10 pole, 48 slot	12 Pole 54 slot	14 pole, 30 slot	16 pole, 18 slot
Coil pitch	4 slots	4 slots	2 slots	1 slot
r_{sn} (p.u.)	0.0370	0.0340	0.0334	0.0345
ψ_{mn} (p.u.)	0.506	0.510	0.511	0.617
L_{dn} (p.u.)	0.355	0.358	0.528	0.605
L_{qn} (at $\omega_{rated,}$ P_{rated} in p.u.)	1.156	1.155	1.148	1.044
% reluctance torque (at $\omega_{rated,}$ P_{rated})	47.3%	46.9%	39.2%	23.9%
Rated current density	4.04 A/mm^2	4.09 A/mm^2	4.23 A/mm^2	4.46 A/mm^2
pf (at $\omega_{rated,}$ P_{rated})	73.7%	73.8%	66.1%	68.35%
EC-CPSR	1.96	2.13	2.25	2.84
Continuous torque at wheel	37.4 Nm	40.7 Nm	43 Nm	54.2 Nm
Peak torque at wheel	114 Nm	130 Nm	92 Nm	62 Nm
G	8.93	9.28	9.24	9.27
Average efficiency	93.3%	93.24%	93.4%	94.2%

Combinations with integral slot per pole per phase did not dominate due to the additional deleterious effect of skewing on phase resistance. The effect of skew on Designs 1, 3 and 4 are found to be negligible. Design 2 has an spp of 1.5 and a mechanical skew angle of 3.33° (or 20° electrical).

Demagnetization characteristics of the four designs determined by FEA are shown in Figure 44. Design 2 is the only design that exceeds the peak torque requirement of the vehicle and is resilient to demagnetization up to 3 times the rated current as seen from Figure 44. The maximum current in most designs in pareto sets is limited by demagnetization rather than heating.

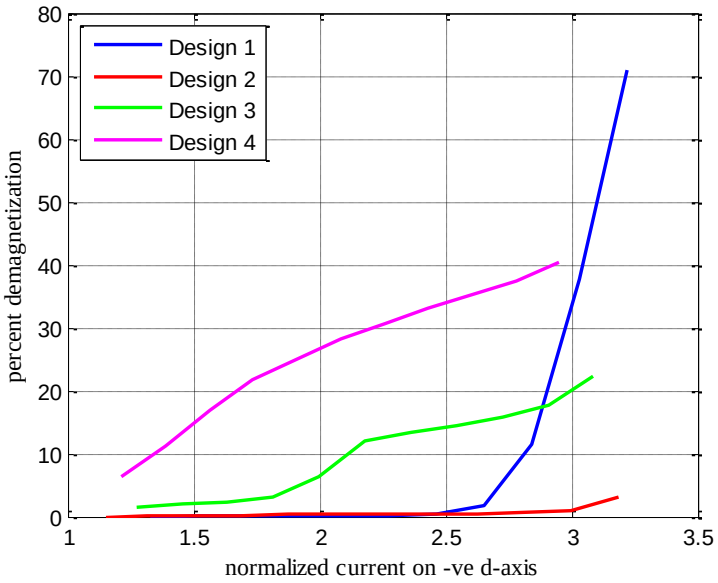

Figure 44 Demagnetization characteristics of the four sample designs at -20°C determined by FEA

5.5. Experimental results

Preliminary test results on a prototype motor close to dimensions of Design 1 of Table 12 are presented in this section.

5.5.1. The prototype motor and experimental setup

A prototype motor based on Design 1 was built for validation of results. The rotor bridge thickness is increased to 0.75 mm for ease of laser cutting, and the air-gap width is increased to 0.6 mm to accommodate excess geometric tolerance stack-up on the test setup. Laminations are laser cut and stacked using a bonding epoxy. A relatively low stacking factor of 92% is achieved due to the process used. Also, the shape of magnets in each barrier is approximated to closest block magnet shape. The magnet widths M_1 and M_2 are 3.0 mm and 2.75 mm respectively.

A picture of the prototype rotor is shown in Figure 45 and the test setup is shown in Figure 46. Key details of the prototype motor are given in Table 13. The motor is mounted on the test bench and coupled with a Kistler 4502A torque sensor with a full range of 20 Nm. A hysteresis brake is used as a load. The motor is controlled in closed speed loop using a TI Piccolo 28035 DSP.

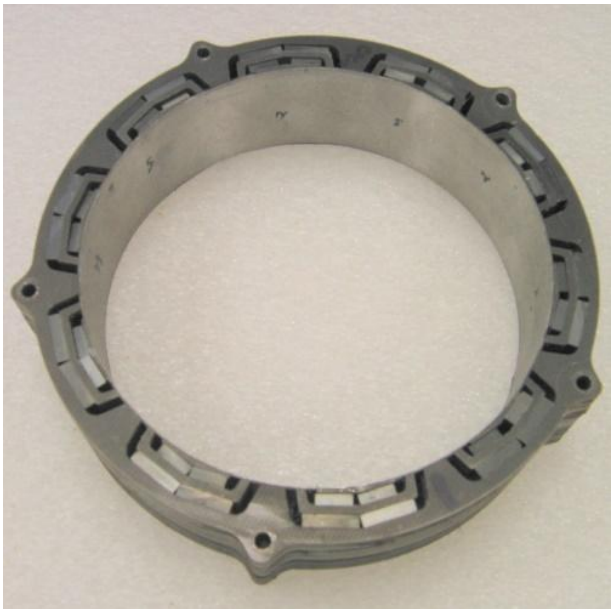

Figure 45 The rotor stack for prototype motor

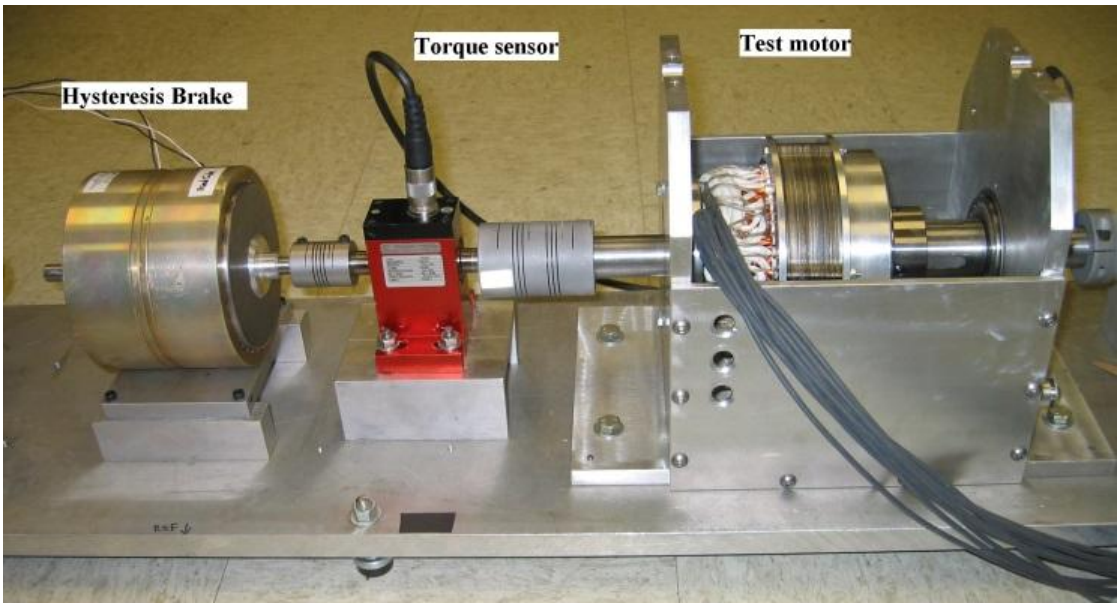

Figure 46 Picture of the experimental setup used to test the prototype motor

Table 13 Details of the prototype motor

Parameter	Value
Rri	67.5 mm
L_{stk}	30 mm
K_{ins}	45%
K_{fil}	38%
D	0 (no magnets in fillet arc)
PM weight	0.19kg
Copper weight	0.7 kg
Rotor core	0.9 kg
Stator core weight	1.2 kg
Calculated r_{phase}	45.5 mΩ
Measured r_{ph}	54.0 mΩ
λ_M estimated from torque measurement	0.011 Vs/rad (phase, peak)

5.5.2. Torque measurement results

The prototype is tested under constant speed command of 600 rpm for different torque loads to verify the FEA based model for torque. The current angle γ (tan-1 –id/iq)

was varied within a range that contains the optimum γ for maximum torque per ampere (MTPA) control to determine γ_{MTPA} experimentally to match it with FEA. Experimentally determined constant torque hyperbolae are plotted in Figure 47. The torque computed by FEA is plotted against measured torque (plus bearing friction) while operating at MTPA for different currents in Figure 48.It is observed that the ratio between measured torque to FEA computed torque is almost constant at 0.92, which is equal to the stacking factor of the stator and rotor core-stacks. The prototype needs further testing to investigate cores loss and windage loss calculations.

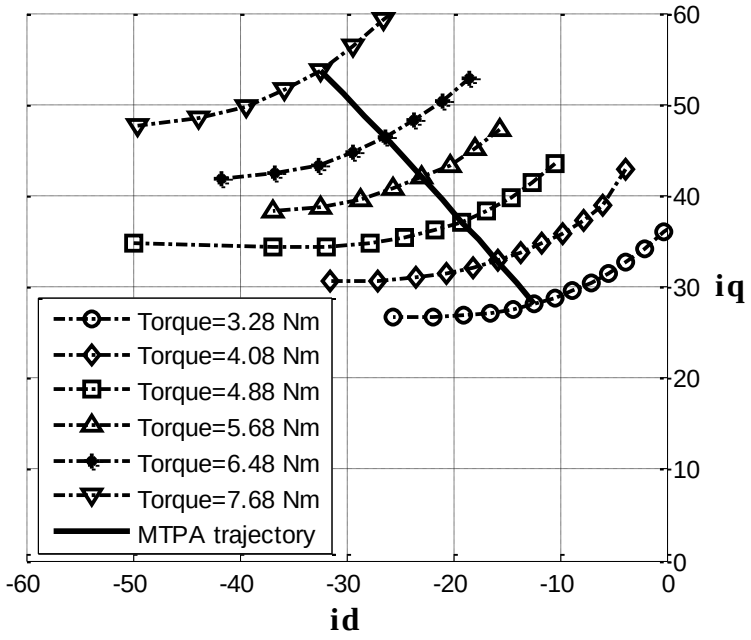

Figure 47 Experimentally measured constant torque hyperbolas and MTPA trajectory of the prototype machine

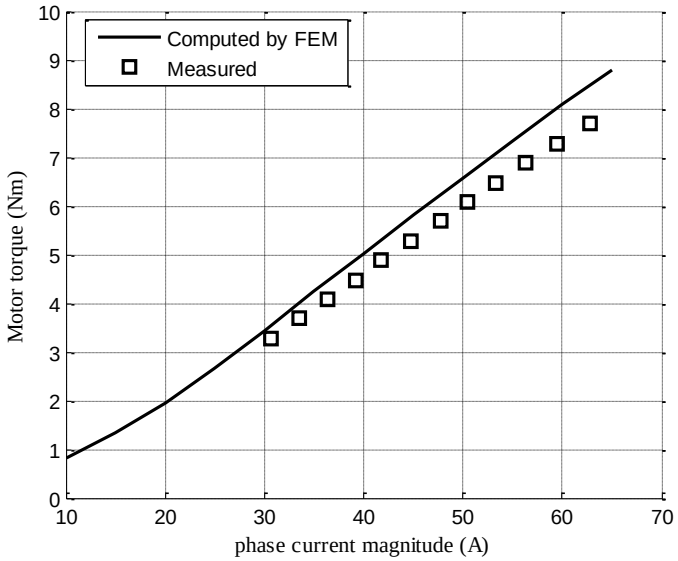

Figure 48 FEA calculated and measured torque vs. current along the MTPA trajectory

5.6. Conclusions

A new rotor topology for outer rotor buried magnet Fa-SynRM is proposed and the geometric parametrization for it is presented. This configuration is useful for the mechanical arrangement of in-wheel geared drive of electric two-wheeler. Thus, a motor designed with this philosophy should be able to operate over the entire speed range with full rated power capability at high efficiency. However, core and windage loss models need to be validated and calibrated for the motor. The proposed topology is optimized and characteristics of candidate designs prove that relatively high saliency ratios can be achieved for two-barrier high pole outer-rotor geometries. Also, the structure provides good flux concentration yielding λ_{Mn}/L_{dn} in the vicinity of 1 for achieving wide EC-CPSR despite the use of low power density PMs. The prototype motor shows close correlation of the FEA based model for torque production and optimum current angle.

6. DESIGN STUDY 3: ULTRA LOW-COST LOW-WEIGHT MOTOR WITH ALUMINUM CONDUCTORS

6.1. Introduction

Energy efficiency is a topic of rapidly increasing significance, and has motivated the development of numerous sets of regulations, both in the United States [85] and internationally, due to a plethora of economic, environmental, and national security factors. Although these increases in efficiency standards promise significant electrical and financial savings over the motor's life-cycle for the end user and the world as a whole, they also drive up the manufacturing cost. As illustrated by the deflated cost trend in Figure 49, high efficiency motors generally require increased quantities of better quality materials (especially copper, electrical steel, and rare earth magnets) and as a result are heavier and more expensive. In light of these considerations, it is clear that motor manufacturers must simultaneously pursue both high efficiency technologies and methods for minimizing the requisite amounts of key cost sensitive materials and processes in order to adapt and produce competitive products in this evolving market place. While new designs and processes are explored, it important that they only require standardized materials to allow for practical implementation and risk-free commercialization. This design study proposes the development and optimization of design geometries which use light weight and inexpensive aluminum conductors in the stator and hard ferrite magnets that are less supply sensitive.

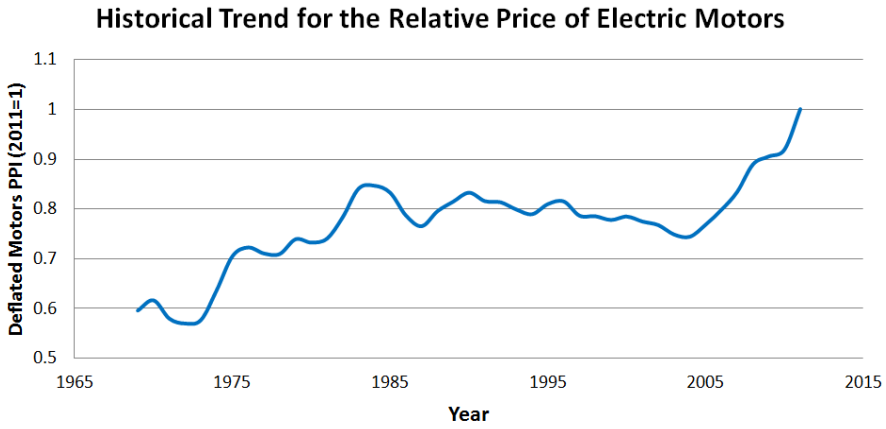

Figure 49 Normalized Historical Trend of Deflated Relative Electric Motor Prices (Source of data: US Bureau of Labor Statistics)

6.2. Target specification

Performance measures of the target power rating of 1kW that was provided in the Electric Motor Education and Research Foundation (EMERF) invitation for proposals is given in Table 14. The given design specifications are particularly challenging; therefore, it is not possible to pre-determine if all of the given performance and cost parameters can be simultaneously achieved. Since cost and efficiency are conflicting objectives, the natural approach is to find the tradeoff between the two. This will be achieved by performing a series of design iterations, in which the efficiency and rated torque are fixed while the cost (and weight) is (are) minimized. This procedure will be repeated for different material selections, as well as slot, pole, and winding combinations. The proposed motor is intended for use in conjunction with a 3-leg six switch inverter with a standard sensorless vector control algorithm.

Table 14 Design specification for ultra low-cost, low-weight motor

Power Output	1kW
Efficiency	95.0% including controller losses
Speed	3,200 rpm
Torque	26.1 lb/in (2.9 Nm)
Voltage	36 volts
Temperature	Class H (automotive)
Rotor Position Detection	Sensorless
Power Density	1000 watts per kg
Volume	320 cubic inches
Cost	$160.00 US (includes controller)
Torque Density	0.3 Nm/kg

6.3. Initial approach, assumptions and choices

The initial approach for this project was developed based on tear-down analysis of a 5hp motor presented in the technical support document of the recently proposed energy efficiency regulation, published by Department of Energy (DOE). The 5-hp induction machine data, given in Table 15, details the costs associated with the various raw materials and the labor. These are the design dependent cost considerations which will serve as weighting factors when determining the relative emphasis to place on minimizing the use of a given material or process. The costs of other motor components such as shafts, casings, varnish, etc. are not significantly impacted by the design and are considered constant. The biggest potential for cost reduction involves replacing copper with aluminum in the stator, a substitution which also significantly reduces the motor's weight. Similar cost reductions are expected to apply for the 1kW design specifications.

Table 15: Design dependent material and labor costs for a 5 hp induction motor. Source: [85]

Component	Weight	Cost
Stator + Rotor Steel Laminations	33.5 lb	0.73 $/lb for M56, 50% yield; total $48.91
Copper Wire	10.1 lb	4.35 $/lb for insulated wire; total $43.93
Aluminum (cast or extruded)	2.9 lb	1.39 $/lb; total $3.77
Labor		$33.46/hr; total $41.83

An optimum design for an entirely different technology cannot be found by merely substituting components of existing design. The entire design process needs to be performed from scratch by exploring different possible options of geometry, slot-pole and winding configurations. The purpose of this research study is to investigate the use of Aluminum conductors in stator and Ceramic grade PMs in the rotor of a salient pole synchronous motor.

It is assumed that the motor will be controlled using a standard (~20 kHz) switching inverter in conjunction with a standard sensorless vector control algorithm. The term "efficiency" used in this chapter accounts only for winding conduction and lamination core losses in the motor. Though it is important to account for additional loss components such as bearing friction and windage, accurate models for such losses are not available at this point and need to be calibrated with actual prototypes. For calculating the cost and weight of the machine, only the active materials are considered. An important cost component of labor cost of winding is treated subjectively and the choice of design based on that is left open as this depends largely on the manufacturing

process, volume, etc. The results for different choices of winding construction are compared from efficiency, material weight and cost perspective.

6.3.1. Conducting material: aluminum vs. copper

Since the main objectives of the design are weight and cost, aluminum should be given due consideration for use in stator windings. Comparison of key characteristics of copper and aluminum are given in Table 16. Though the resistivity of aluminum is higher than copper, the resistivity-mass density product is much lower (72 $n\Omega \cdot m \cdot g/cm^3$ as compared to 150 $n\Omega \cdot m \cdot g/cm^3$ of copper), and the resistivity-mass density-price ratio of copper is 7.5 times that of aluminum. In the case of an electric machine, the impact of these properties on the overall weight and cost of the machine needs to be studied. In order to establish a fair comparison of weight and cost, the efficiency of the two machines should be equal.

Table 16 Comparison of characteristics of copper and aluminum

	Copper	Aluminum
Conductivity (Mho/m) @ 20° C	5.96E7	3.77E7
Density (g/cc)	8.9	2.7
Spot Price ($/lb)*	3.18	0.93
Temperature Coefficient of Resistivity (%/K)	0.39	0.393
Volumetric heat capacity (J/cc/K)	3.45	2.42

*Source: Infomine.com

In addition to use of a different conducting material, construction of the winding is of prime importance. High slot fill can be achieved by use of bar-wound conductors. For the same motor geometry, if by substituting multi-strand copper winding with a higher slot-fill aluminum bar-winding, if the same ohmic loss at rated operation can be achieved, then the design with aluminum winding is obviously lighter and has lower material cost. However, high power density machines typically operate at high frequencies (>200 Hz), and hence the ac-resistance of bar-windings would increase due to skin and proximity effects, which are negligible in multi-strand conductors. The question arises, whether these effects would deteriorate the performance to a degree that multi-strand copper emerges as a better choice. Another question is whether designs with bar-wound copper would out-perform the other two aforementioned choices. These questions can be answered only by conducting the full design process as will be seen in this design study

It is certainly very interesting to note that the ac-resistance coefficient affects aluminum and copper conductors differently for the same frequency and dimension of conductor (Figure 50). Thus it is feasible to use bigger aluminum bar conductors than it is to use copper bar conductors. The ultimate effect of this on motor performance is compared by running the full optimization for the two cases and is discussed in sub-section 4.

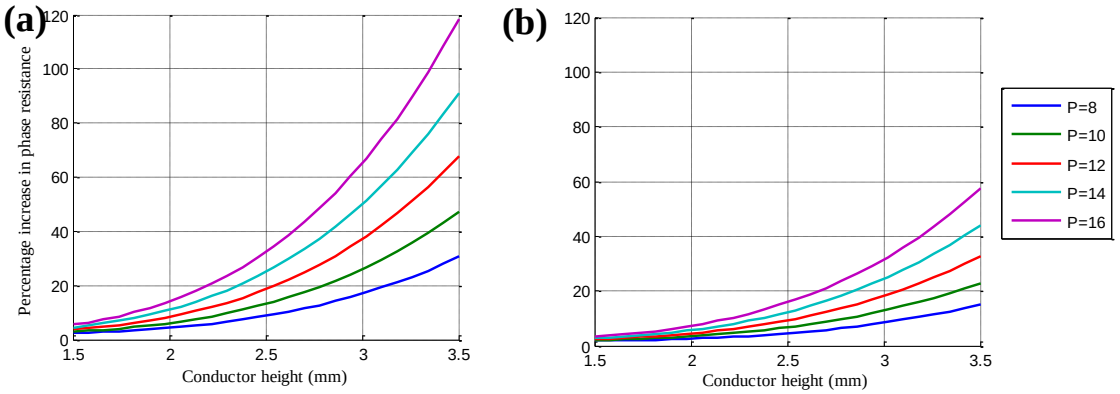

Figure 50 Increase in ac resistance of rectangular conductors (4 per slot) at 3200 rpm for different pole numbers (a) copper conductors and (b) aluminum conductors

6.3.2. Bar-wound construction for improved conductor fill

Bar-wound stators can achieve higher conductor fill compared to stator wound with multi-stranded bundle. The actual conductor fill depends on the slot size and the conductor size. For smaller slots, fraction of area occupied by slot liners is more and results in smaller conductor fill. Similarly, multi-strand conductors result in higher fraction of the available area occupied by wire enamel. Additionally, the inter-strand distance cannot be easily maintained small if the windings are not formed. For the same slot area, a relatively higher conductor fill can be achieved if bar conductors are used. Another alternative to achieve high conductor fill is the use of pre-formed compressed coils. However, insertion of pre-formed coils requires a segmented stator structure or open slot construction.

Examples of bar windings

Certain cost-sensitive high performance applications have recently started using such a bar-wound construction for small motors. The GM Extended Range Electric

Vehicle (EREV) [63] motor uses an 8-pole 48 slot arrangement. A laboratory prototype of a 12-pole 36-slot bar-wound stator with 2 conductors per slot is shown in Figure 51(a). This arrangement is also used in commercially available car alternators as shown in Figure 51(b).

Restrictions on design due to use of bar-windings

Number of turns in each slot can be 1, 2, or 3 for double layer and 1-6 for single layer topologies. This would highly restrict the voltage rating of the machine. For ease of welding and bending, the aspect ratio of the cross section of conductor (height/width) should be limited i.e. a strip or foil conductor may be difficult/infeasible to manufacture with such a motor topology. This should limit the split ratio (R_{ro}/R_{so}) of the motor and slot depth. For deeper slots, skin and proximity effects become prevalent resulting in increased ac resistance at the fundamental frequency of operation. The increased ac resistance may defeat the purpose of using bar-conductors in certain cases.

(a)

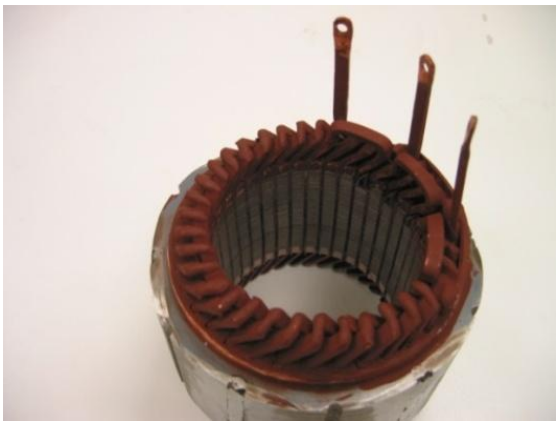

(b)

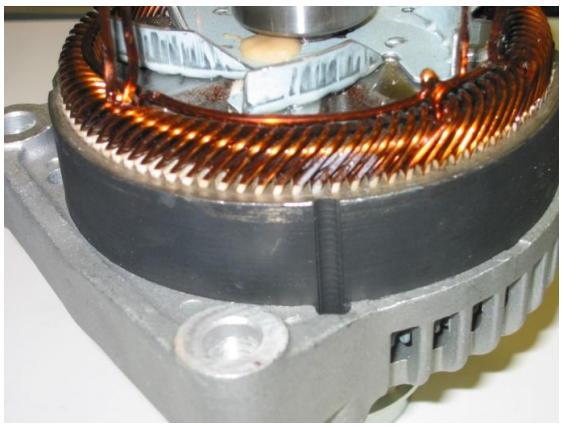

Figure 51 Example bar-wound stators

6.3.3. Pre-compressed single slot-pitch windings

Another approach to improved slot-fill is the use of pre-compressed coils [65, 66, 86]. This method applies to single slot-pitch combinations and requires either plug-in tooth method, or open slots for insertion of the pre-compressed winding. Slot fill factors ranging from 60% to 75% have been reported in literature for this construction. The actual slot fill will depend on wire diameter, slot dimensions and the compression pressure.

6.3.4. Ferrite PM material and rotor structure

Ceramic Ferrite magnets are used in rotors of automotive and industrial applications. This class of magnets is represented by the general formula MO.6Fe2O3 (where M could be Strontium or Barium). This type of magnet is the only readily available alternative to rare-earth magnets that has good energy density and shows resilience to demagnetization. An added advantage of ferrite PMs do not suffer from eddy effect solid loss since they are non-conducting. In order to achieve good torque density, ferrite PMs need to be used in conjunction with rotor structures that allow maximum flux concentration. The application of interest requires a very torque dense (Nm/kg) motor with a high efficiency. Weight reduction can be achieved by using higher pole number machines. However, a significant fraction of PM flux leaks though bridges that characterize buried magnet rotor topologies. This fraction of leakage increases with higher pole number. Thus there is a conflicting requirement of increased pole count and decreased leakage for achieving high efficiency light weight machines.

For the purpose of this study, the spoke rotor topology is chosen since it has only one bridge per pole as shown in Figure 52. The thickness of this bridge is kept to a minimum manufacturable width of 0.5mm. As can be seen from Figure 52(b), a 1 mm bridge leads to almost 25-30% PM flux leakage for this size of rotor. It should be noted that such a rotor needs to be assembled by special manufacturing method in order that the shaft does not lead to more flux leakage, but holds each pole of the rotor to avoid plastic deformation of the bridges. The AC-12 grade of ceramic ferrite is chosen.

Characteristics are taken from the material datasheet published by Arnold Magnetics [40]

In addition to the benefit of having only one bridge per pole, the spoke rotor topology can be modified by introducing ‘voids’ in the rotor for further weight reduction of the motor. As an example, a magnetic field plot of 6-pole Ferrite PM rotor structure with ‘voids’ is shown in Figure 53. The presence of such voids (if correctly designed), does not lead to any significant reduction in motor performance or mechanical strength of the rotor.

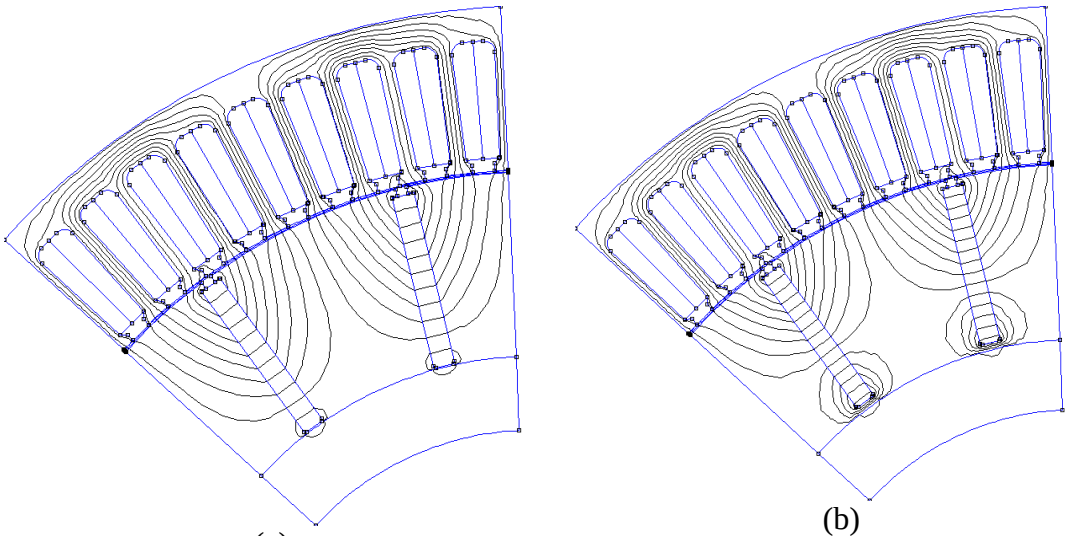

(a) (b)

Figure 52 Leakage of PM flux through bridge (a) bridge thickness = 0.5 mm and (b) bridge thickness = 1 mm

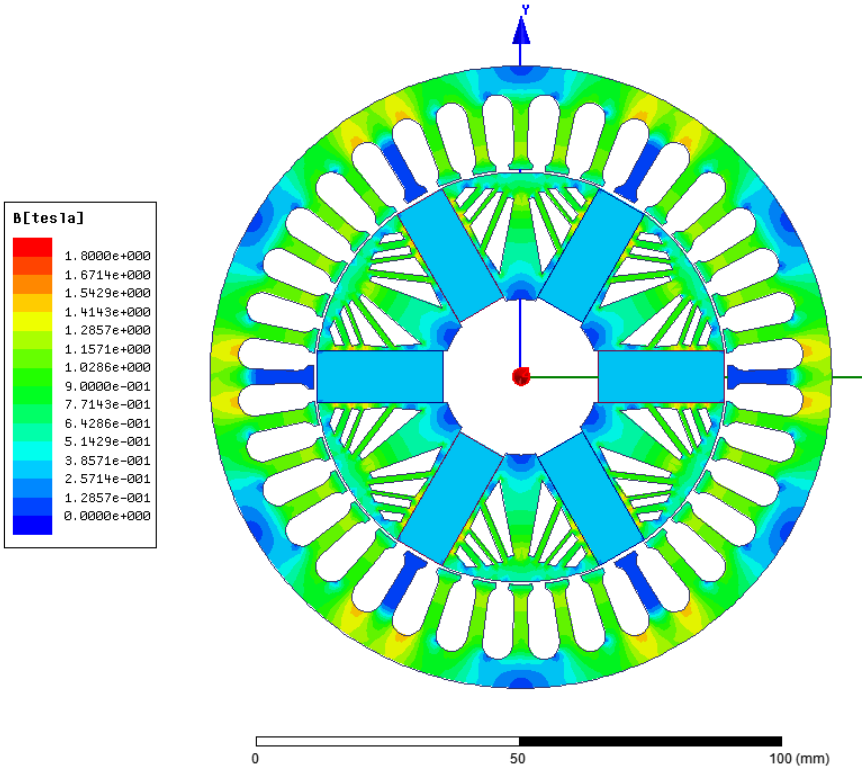

Figure 53 Additional voids in rotor core for weight reduction

6.3.5. Slot-pole combinations

Slot-pole combination and winding slot pitch are important design parameters that influence winding pattern, and winding labor cost. If the spp of a three phase machine is expressed as $a + \frac{b}{c}$ as given in eq. (7), it can be deduced that if a=0, the winding pitch will be one or two slots. The one slot combination would result in a non-overlapping winding. For a≠0, and b=0, it is a integral slot distributed winding and for a≠0 and b≠0, it is called a fractional slot concentrated (FSDW) winding.

Distributed

The distributed winding [64] would need only 3 jumpers if b/c is 0 or 0.5. In all other cases, the windings will take more labor due to increased number of end

connections. Spp=1 designs are avoided due to the large cogging torque and torque ripple. Higher pole numbers are desirable in order to reduce machine weight. Also, slot numbers greater than 72 are avoided to reduce the number of operations. With these criterion, the slot-pole combinations for different coil pitch that result in a winding factor ($k_d.k_p$) of 0.9 or more are given in Table 17.

Single slot pitch (tooth-wound)

For the same pole numbers as the distributed winding combinations, the available single slot pitch combinations with even slot numbers and a winding factor (pitch and distribution) greater than 0.9 are considered. The main advantage of this type of windings is the tight non-overlapping end-windings. For the design specification of this research, these combinations are unfeasible be used in conjunction with bar windings. Due to restrictions on conductor width for bar-wound stators, fewer than 36 slot stators would result in a very small air-gap radius (less than 30 mm). For this dimension, it is difficult to achieve good flux concentration using ceramic magnets. Additionally, the properties of the PMs would deteriorate for small sizes. Therefore, this set of pole-slot combinations are used only with multi-stranded windings or with pre-compressed windings with open slots.

Table 17 Slot-pole and pitch combinations considered for distributed winding configurations

Number of slots (N_s)	Number of poles (N_p)	spp	Winding factor	Coil pitch
36	8	1.5	0.945214	4
36	8	1.5	0.945214	5
48	8	2	0.933013	5
48	8	2	0.965926	6
54	12	1.5	0.945214	4
54	12	1.5	0.945214	5
60	8	2.5	0.909854	6
60	8	2.5	0.951436	7
60	8	2.5	0.951436	8
60	10	2	0.933013	5
60	10	2	0.965926	6
72	12	2	0.933013	5
72	12	2	0.965926	6
72	16	1.5	0.945214	4
72	16	1.5	0.945214	5

Table 18 Slot-pole combinations with single tooth coil pitch considered

Number of slots (N_s)	Number of poles (N_p)	spp	Winding factor	Coil pitch
12	10	2/5	0.933013	1
12	14	2/7	0.933013	1
18	14	3/7	0.901912	1
18	16	3/8	0.945214	1

6.3.6. Assumptions

The following assumptions were made for this design study

1) It is assumed that there is no restriction on the dimensions of the motor. The optimum designs obtained with this approach is expected to be the global – unconstrained optimal geometries.

2) Thermal model: It is assumed that a cooling fan on the shaft maintains a steady flow of 5 m/s on the periphery of the frame that is equipped with fins in the axial direction. The ambient temperature is assumed to be 40 C

3) The price of laminations is calculated assuming that the round stampings are packed in a square arrangement on a large lamination sheet. The wastage at the edge of the sheet is neglected. The price of ArcelorMittalM235-35a grade 0.35 mm thickness steel is assumed to be $1.02 per lb. The yield is observed to be between 35-50% of the used area of sheet. In practice, this can be improved by using hexagonal packing between stampings. The price of the PM's is assumed to be $4.5 per lb for mass production.

4) The controller loss comprises of switching and conduction losses in devices, gate drive, passive components, sensing and microcontroller. In general, the efficiency of the controller is expected to be higher than motor efficiency. As documented in [87], a single stage converter can yield an efficiency of 98% using conventional IGBTs or an efficiency of 99.3% using wide band-gap devices [88] for this rating. The actual efficiency will depend on the type of source (dc, 1ph or 3 ph ac) and source voltage, the choice of filter and passive components.

5) The air-gap width is assumed to be 0.35 mm.

6) The motor can be started using an open-loop startup so that a well-tested sliding mode flux observer can be used for sensorless control of the motor when it crosses a minimum speed threshold.

6.4. Design optimization

This design problem is a typical category 1 problem the same as the case discussed in section 3.8.2.In this case, current density J_c is a design parameter for which the bounds are selected between 2 A/mm^2 and 8 A/mm^2. The rotor outer radius R_{ro} is treated as the base dimension with bounds between 30 mm and 75 mm. It is checked back after optimization that all designs in the pareto set lie well within the bounds chosen for this parameter. The optimization is performed these different cases:

1. Distributed, copper, multi-strand: all pole-slot combinations of Table 17 (separately for each pole count)
2. Concentrated single slot-pitch multi-strand copper: all pole-slot combinations of Table 18 (all combinations together)
3. Distributed aluminum, bar-wound: all pole-slot combinations of Table 17 (separately for each pole-count) except 6 pole
4. Distributed copper, bar-wound only 10 pole 60 slot with coil pitch of 5 and 6 slots
5. Open slot concentrated single slot-pitch multi-strand aluminum pre-compressed coils: all pole-slot combinations of Table 18 (all combinations together)
6. Additionally, multi-stranded copper conductors of case 2 are substituted with multi-strand aluminum conductors and re-evaluated.

A population size of 200 it used to optimize over 20 generations in each case. Geometric parameters used to describe the 2D geometry are shown in Figure 54.

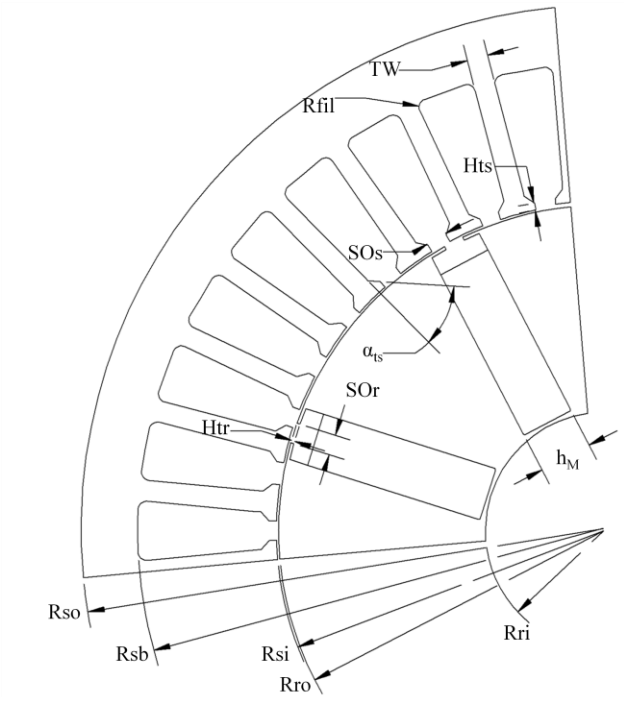

Figure 54 Geometric parameters needed for description of the proposed motor

6.5. Optimization results

6.5.1. Comparison of different configurations

Figure 55-Figure 58 show comparisons of pareto-optimal sets of designs that employ different types of windings. Each set is optimized by the process described in previous section. Several interesting observations can be made based on this data:

1) The hypothesis that aluminum bar-conductor wound stators would exceed efficiency for lower weight as compared to multi-strand copper wound stators is evident if Figure 55 and Figure 56 are compared. However, the single-slot pitch configuration dominates both the configurations in terms of efficiency and weight.

2) The best efficiency for distributed multi-strand copper winding designs is achieved for 8 pole 48-slot configuration and is 95.7% while the best efficiency for

single slot pitch multi-strand copper windings is achieved for 10-pole 12 slot configuration and is 96.4% (Figure 56)

3) For slightly lower efficiency (<95%), higher pole configurations yield lower weight and lower cost designs for the same efficiency for distributed configuration (Figure 55)

4) In most cases, active material weight and cost are directly correlated and are not likely to be conflicting objectives.

5) The dominance of single slot-pitch configurations over distributed can be attributed to lower Carter's coefficient, and smaller, non-overlapping end-windings as compared to distributed winding designs.

6) The minimum weight to achieve 96% efficiency (without accounting for converter, windage, and friction losses) is 2.8 kg for single slot wound multi-strand copper conductors and 3.4 kg for bar-wound aluminum conductors.

7) The best efficiency achieved for any construction is 97% by aluminum pre-compressed open-slot configuration. The weight of active materials of this design is approximately 4.8 kg.

8) The best efficiency for any design that weighs 1 kg (based on the specified design criteria) is 93% for 16 pole-18 slot single slot-pitch pre-compressed aluminum winding configuration.

9) Figure 57 shows the comparison of 10-pole bar-wound copper and aluminum conductor pareto optimal sets. In terms of weight, both topologies show an almost same trend except for the highest efficiency designs obtained by copper conductor designs.

10) A direct substitution of copper windings with aluminum windings may not yield a truly optimum design or realize the best potential of using a different material as can be concluded from the comparison of Figure 58

The results need to be interpreted with caution because better performance of one material/construction over others is valid only in the light of the current problem at hand and may change with design specifications and objectives. Also, the validity of production price results depends on material price fluctuations. Details of representive high efficiency designs of different configurations is given in Table 19 in order to get a better picture of dimensions, configurations, and weight and loss distribution.

(a)

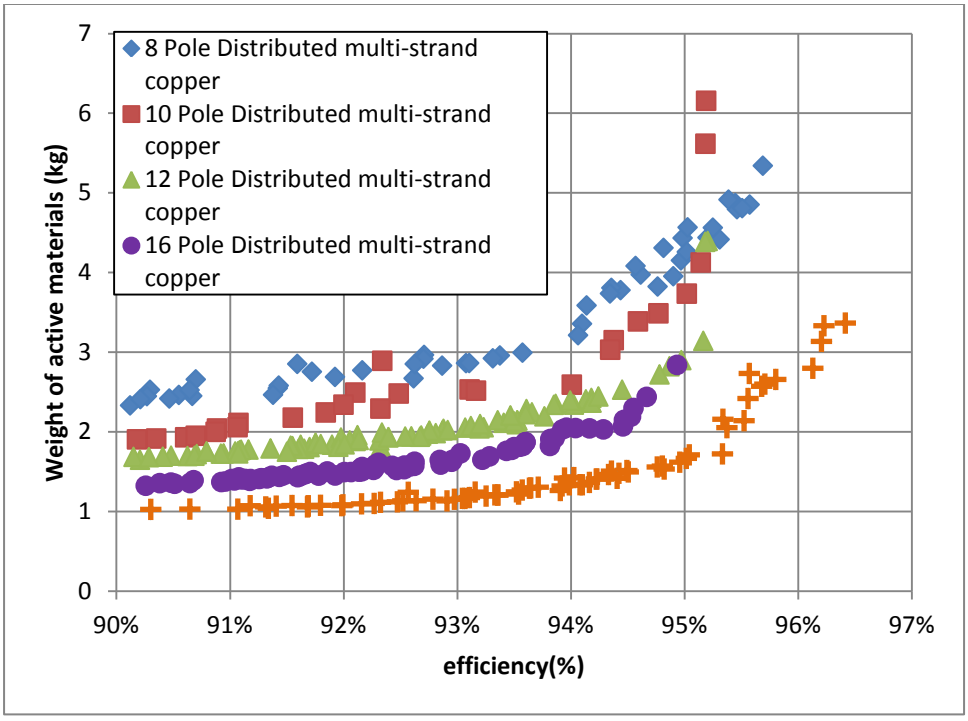

(b)

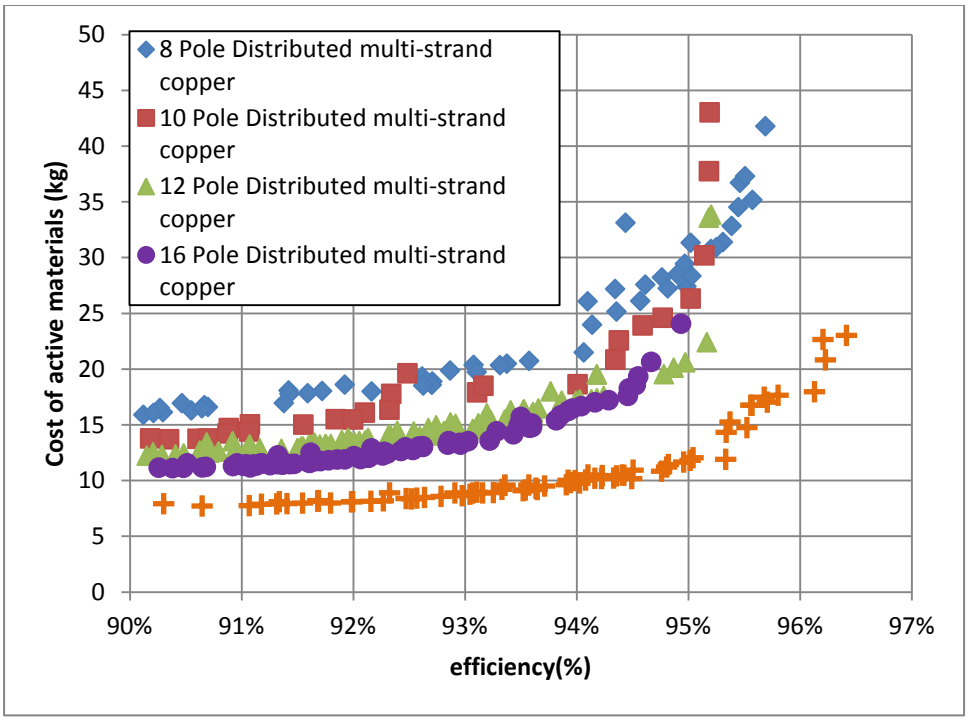

Figure 55 Pareto-optimal sets of multi-stranded copper winding designs (cases 1 and 2)

(a)

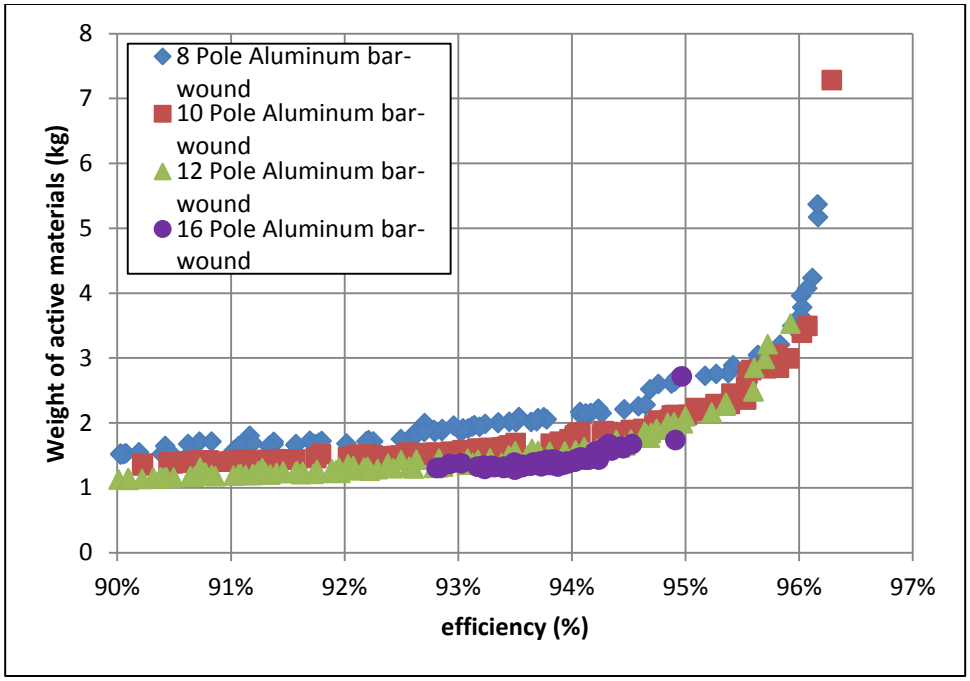

(b)

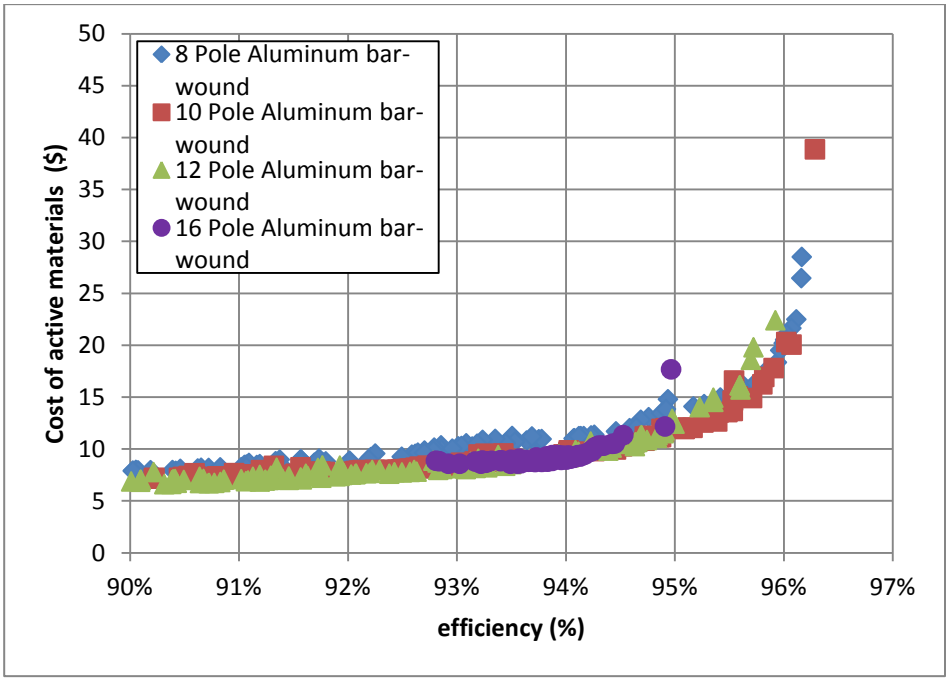

Figure 56 Pareto-optimal sets of bar-wound aluminum conductor designs (case 3)

(a)

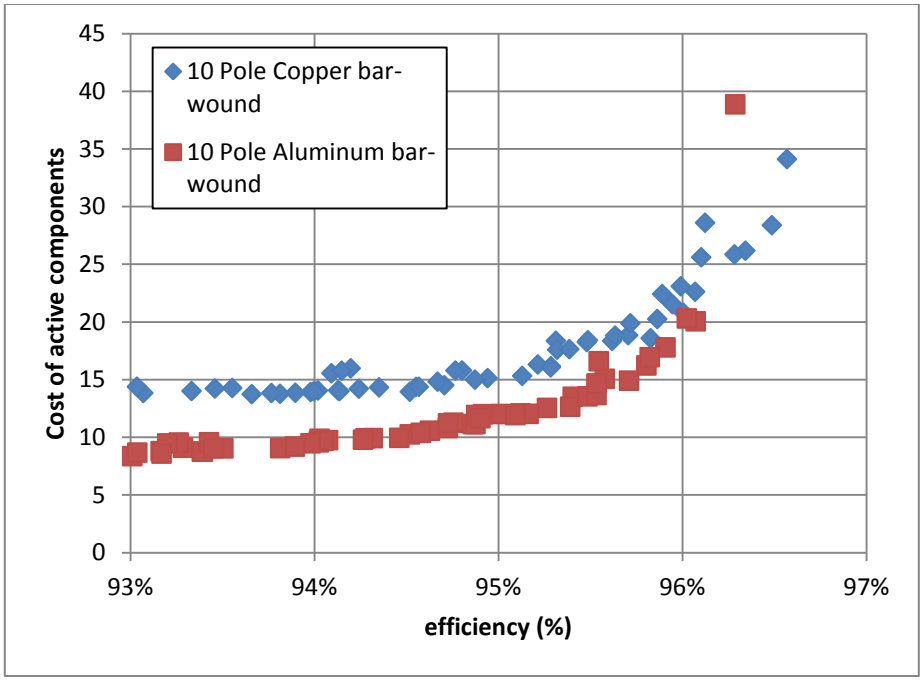

(b)

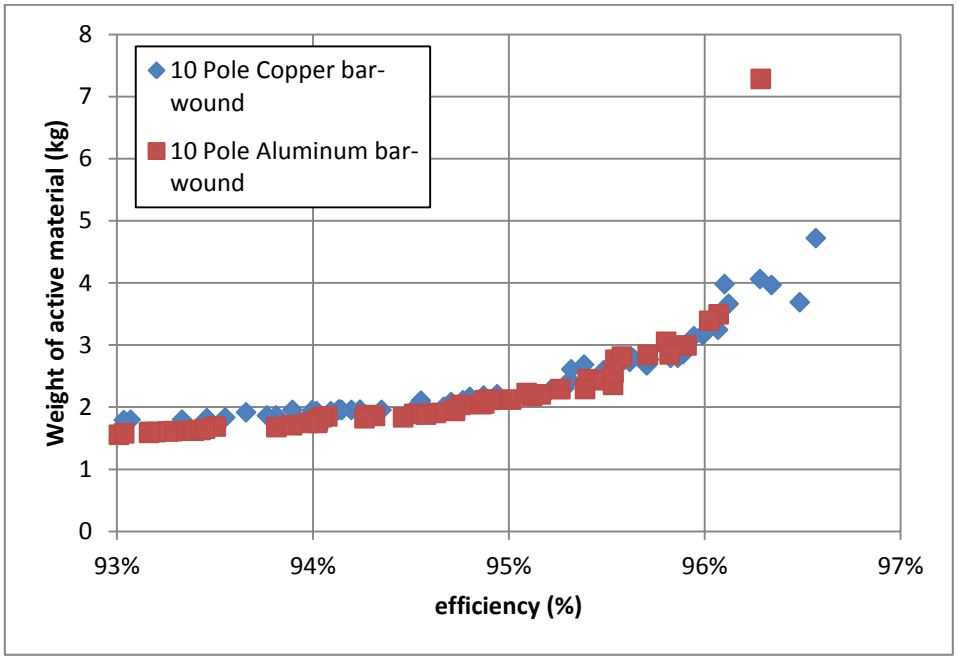

Figure 57Comparison between pareto-optimal sets of 10-pole 60 slot copper and aluminum bar conductor motors

(a)

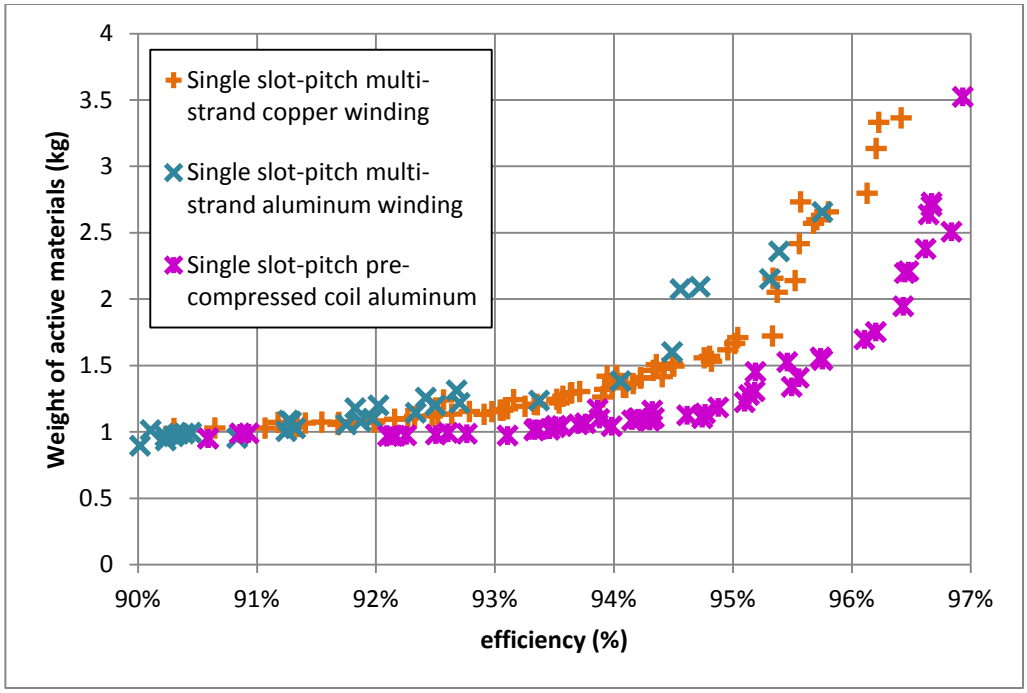

(b)

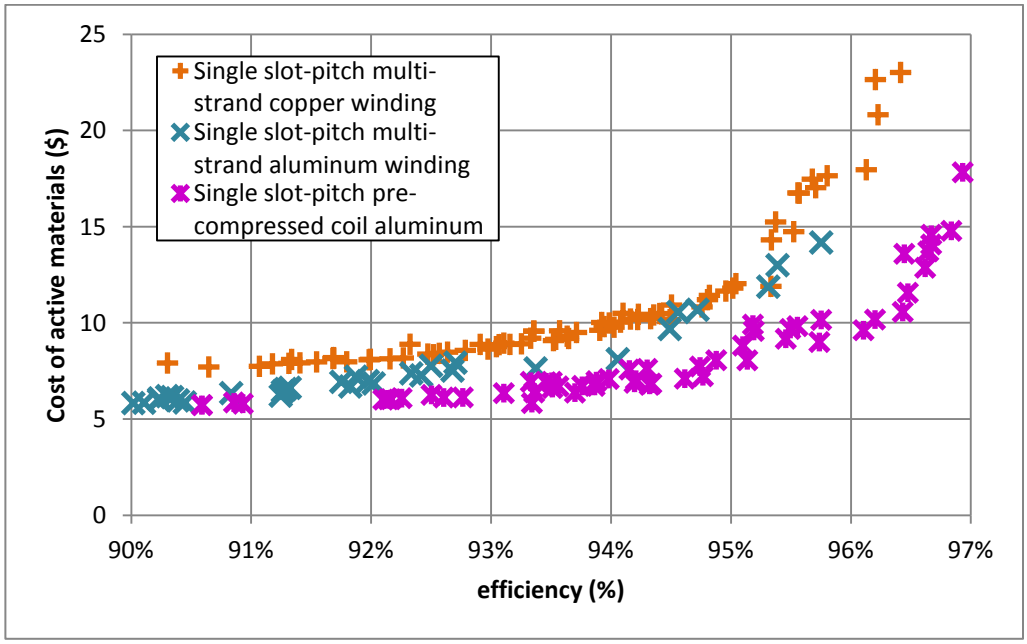

Figure 58 Comparison of designs obtained by substituting multi-strand copper conductors with multi-stand aluminum conductors for single slot pitch windings

Table 19 Characteristics of select optimal designs representative of different winding technologies

		Design 1	Design 2	Design 3	Design 4	Design 5
Winding construction		Copper multi-stranded	Copper bar-wound	Aluminum bar-wound	Aluminum multi-stranded	Aluminum pre-compressed open slot
Poles, slots		10 Pole, 12 Slot	10 Pole 60 Slot	12 Pole-54 Slot	10 Pole 12 Slot	10 Pole 12 Slot
Coil pitch		1	5	4	1	1
Slot fill		42%	81.3%	85.7%	42%	70%
Motor Efficiency*		96.23%	96.0%	95.1%	94.7%	97.0%
Power Factor		94%	99%	99%	86%	94%
Temperature rise		27°C	27°C	33°C	35°C	21°C
Current Density in conductor (pk)		4.6 A/mm^2	5.03 A/mm^2	3.68 A/mm^2	4.7 A/mm^2	2.0 A/mm^2
Fundamental rms Line voltage (wave winding or *p=1*)		3.26 V	16.24V	11.98 V	1.08 V	176 V†
Fundamental rms Line voltage (lap winding *p = gcd(Np,Ns)*)		1.63 V	1.62V	1.99 V	0.54 V	88.0 V
Stator outer diameter		158 (6.2 in)	181 mm	153 mm	179 mm	178 mm
Stack length		35 (1.37 in)	22.86	26.5	18	30 mm
Conduction loss		15.5 W	21.4W	28.7W	34.0 W	12.9 W
Core loss		23.6 W	19.9W	23.1W	21.7 W	18.7 W
Stator conductor	weight	0.62 kg	0.69 kg	0.33 kg	0.354 kg	0.56kg
	cost	$5.90	$6.6	$1.06	$3.40	$1.79
Rotor + stator lamination	weight	2.43 kg	2.2 kg	1.54 kg	1.08 kg	2.73 kg
	cost	$12.14	$10.54	$8.70	$6.20	$13.68
Permanent Magnets	weight	0.28 kg	0.43 kg	0.33 kg	0.22 kg	0.24 kg
	cost	$2.78	$4.25	3.29	$2.21	$2.37
Total active material weight		3.33 kg	3.32 kg	2.2 kg	2.09 kg	3.52 kg
Total active material cost		$20.82	$21.4	$13.04	$10.69	$17.84

*electromagnetic efficiency (does not include bearing and windage friction losses)
†Assuming a maximum possible wire diameter of 17 AWG with all turns in series
Note: loss and weight components may not add up exactly due to round-off error

7. CONCLUSIONS AND FUTURE WORK

7.1. Conclusions

In an ideal world, an "automated" design tool is one that is capable of taking the user from design requirements to the pareto-set without any user insight into the design process. On similar lines, a researcher who seeks alternatives to standard technologies (topology, material or manufacturing technique) with the aim of surpassing what is achievable with standardized technologies should be able to establish fair comparison between existing and new technologies using the automated design tool. To go from this rather abstract definition of such a design tool to a software implementation, this dissertation gives a structure and defines the scope for such a tool. This tool is developed in a Matlab/C++ environment and is employed to research electric machine topologies in this dissertation. The three case studies aim at identifying alternatives to standardized topologies for the respective design requirements. Several interesting conclusions related to topology, construction and design choices for the three case studies were drawn and are summarized in the respective chapters.

A common learning from practical implementation with a broader view is discussed here. Conclusions related to parts of the work are discussed at the end of each chapter. In researching a new topology or designing a machine with very little practical data on certain parameters and approximate models (especially mechanical loss and thermal models), there is a degree of inaccuracy in the overall evaluation function. Uncertainty in parameters also depends on the manufacturing process followed. Uncertainty/inaccuracy stems from one or more of the following factors:

1) Contact resistances: interface gaps depend on geometric tolerances. This variability may be reduced by using a bonding layer, etc.
2) Flow field around the machine
3) Inaccurate material models/nonstandard materials/dimensions or process leading up to degradation of material properties
4) Certain approximations made during modeling may not be valid
5) The optimum design may not be manufacturable and needs modifications for manufacturing, that lead to degraded performance.

The above factors pose a serious limitation to complete automation of design process. A practical design process would involve an intermediate step of manufacturing a machine, calibrating the particular models used in fitness evaluation and then repeating the process if a significant performance improvement is expected. The workflow for such a practical design process is shown in Figure 59.

Another interesting aspect of design is the ever-changing scenario of material prices, energy price and manufacturing costs and techniques. The "optimal set" that involves these factors will take different shapes based on the market scenario. Based on new automation and robotic techniques, the design process also needs to consider the emerging concept of "design for automation." [89]

Due to all of these factors, machine design will always be an area of active research. Regardless of these facts, the proposed framework is a useful link in the design process and needs to be updated to adapt to trends in technology and modeling.

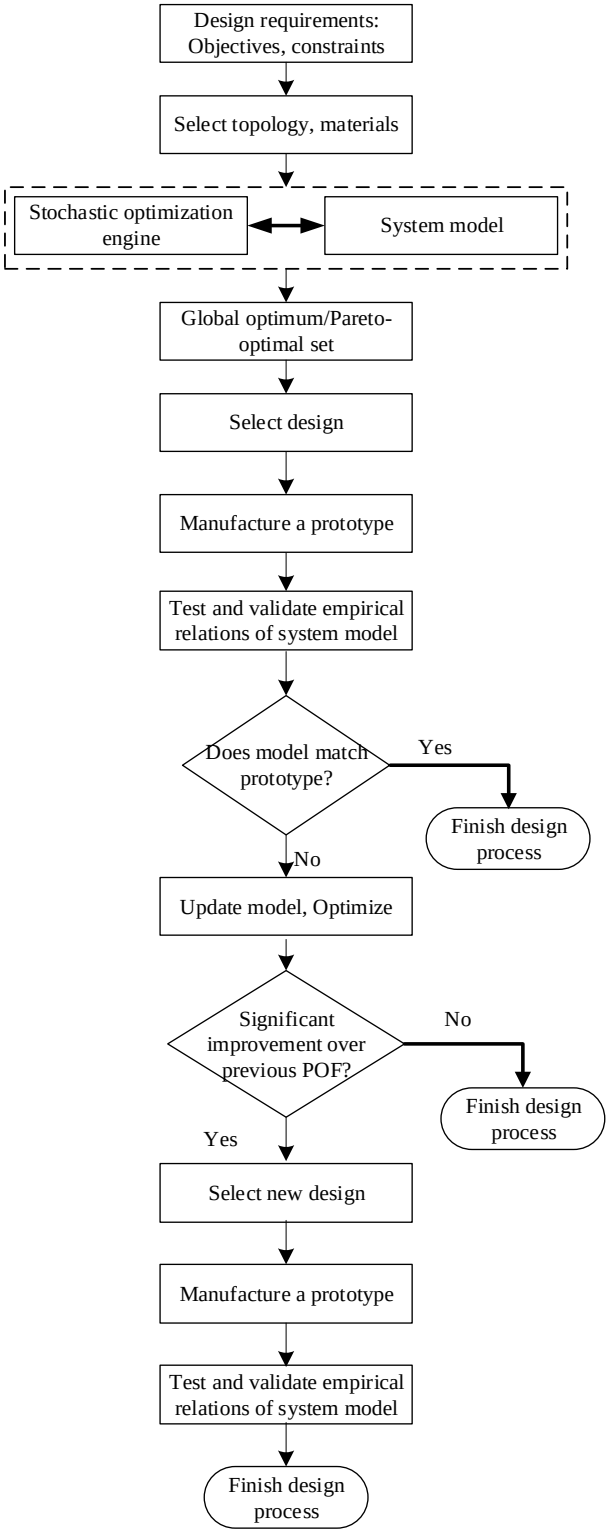

Figure 59 A practical machine design process

7.2. Future work

Some of the possible avenues of future work on this topic are presented here:

1) *Inclusion of effects of manufacturing tolerances:* An electric machine is fabricated by assembling individual components made using different types of manufacturing techniques. Each step of manufacturing introduces some degree of inaccuracy due to geometric tolerances of components used for machining each part. Assembly of such non-ideal components leads to a "stack up" of geometrical tolerance which may result in significant air-gap eccentricity or unbalance in windings or PM fluxes. Any design produced by the optimization process, when manufactured should meet performance criteria even if a sample has the worst expected geometric tolerance stack-up. A short discussion on the effect of disposition of windings in slot was included in design study 1. Inclusion of such an analysis in the fitness evaluation is an essential, but challenging aspect of work.
2) *Automation of design choices:* The process of going from user requirements to the formal definition of an optimization problem involves design choices as discussed in Chapter 3. These design choices are made manually in the current form of implementation. Automation of this process is another challenging and essential step for complete design automation. Two possible approaches for this are: derivation of rules based on physical system models or by means of machine learning/artificial intelligence techniques based on experience with optimization of machines for a large number of design scenarios.

3) *Improvement of models*: The FEA based model used in the proposed method assumes a sinusoidal excitation for computing torque and loss under any operating condition. In a voltage source drive, a non-ideal machine would result in a non-sinusoidal current and would lead to additional torque ripple and losses. To include such effects, an electric transient needs to be solved for the machine. Additional losses due to inverter switching may become significant at low-load conditions for low switching frequencies. The inverter losses can be included in the model. Machine vibration due to resultant periodic stress should also be included in the model if this is an important consideration for the application in question.

4) Combining gradient based local search with global search without re-meshing: The framework and methods presented in this dissertation is suitable for gradient-free search methods. It may be possible to make the search process more effective if local optimization based methods are combined with gradient free global search. Classical methods such as design of experiments or gradient based local search may be employed to improve the local convergence of the solution. This would prove to be computationally burdensome process for high number of geometric inputs. However, as rightly pointed out by Weeber and Hoole [90] this process can be integrated with the existing mesh structure. Very fast convergence of the non-linear FE solver can be achieved using this technique that may pave the way for using gradient based local search.

REFERENCES

[1] S. D. Sudhoff, J. Cale, B. Cassimere, and M. Swinney, "Genetic Algorithm Based Design of a Permanent Magnet Synchronous Machine," in *Electric Machines and Drives, 2005 IEEE International Conference on*, San Antonio, TX, 2005, pp. 1011-1019.

[2] R. Vartanian, Y. Deshpande, and H. A. Toliyat, "Performance analysis of a rare earth magnet based NEMA frame Permanent Magnet assisted Synchronous Reluctance Machine with different magnet type and quantity," in *Electric Machines & Drives Conference (IEMDC), 2013 IEEE International*, Chicago, IL, 2013, pp. 476-483.

[3] D. W. Novotny and T. A. Lipo, *Vector Control and Dynamics of AC Drives*: Clarendon Press, 1996.

[4] T. M. Jahns, "Flux-Weakening Regime Operation of an Interior Permanent-Magnet Synchronous Motor Drive," *Industry Applications, IEEE Transactions on*, vol. IA-23, pp. 681-689, 1987.

[5] R. F. Schiferl and T. A. Lipo, "Power Capability of Salient Pole Permanent-Magnet Synchronous Motors in Variable Speed Drive Applications," *IEEE Transactions on Industry Applications*, vol. 26, pp. 115-123, Jan-Feb 1990.

[6] W. L. Soong and T. J. E. Miller, "Field-Weakening Performance of Brushless Synchronous Ac Motor-Drives," *IEE Proceedings-Electric Power Applications*, vol. 141, pp. 331-340, Nov 1994.

[7] Z. Q. Zhu, D. Howe, E. Bolte, and B. Ackermann, "Instantaneous magnetic field distribution in brushless permanent magnet DC motors. I. Open-circuit field," *Magnetics, IEEE Transactions on*, vol. 29, pp. 124-135, 1993.

[8] T. Lubin, S. Mezani, and A. Rezzoug, "2-D Exact Analytical Model for Surface-Mounted Permanent-Magnet Motors With Semi-Closed Slots," *Magnetics, IEEE Transactions on*, vol. 47, pp. 479-492, 2011.

[9] M. L. Bash, J. M. Williams, and S. D. Pekarek, "Incorporating Motion in Mesh-Based Magnetic Equivalent Circuits," *Energy Conversion, IEEE Transactions on*, vol. 25, pp. 329-338, 2010.

[10] B. Nikbakhtian, S. Talebi, P. Niazi, and H. A. Toliyat, "An analytical model for an N-flux barrier per pole permanent magnet-assisted synchronous reluctance motor," in *Electric Machines and Drives Conference, 2009. IEMDC '09. IEEE International*, Miami, FL, 2009, pp. 129-136.

[11] E. C. Lovelace, T. M. Jahns, and J. H. Lang, "A saturating lumped parameter model for an interior PM synchronous machine," in *Electric Machines and Drives, 1999. International Conference IEMD '99*, Seattle, WA, 1999, pp. 553-555.

[12] S. Salon, *Finite Element Analysis of Electrical Machines*. Boston: Kluwer Academic Publishers, 1995.

[13] N. Bianchi and S. Bolognani, "Magnetic models of saturated interior permanent magnet motors based on finite element analysis," in *Industry Applications Conference, 1998. Thirty-Third IAS Annual Meeting. The 1998 IEEE*, St. Louis, Missouri USA, 1998, pp. 27-34 vol.1.

[14] J. A. Walker, D. G. Dorrell, and C. Cossar, "Flux-linkage calculation in permanent-magnet motors using the frozen permeabilities method," *Magnetics, IEEE Transactions on*, vol. 41, pp. 3946-3948, 2005.

[15] D. M. Ionel and M. Popescu, "Finite-Element Surrogate Model for Electric Machines With Revolving Field: Application to IPM Motors," *Industry Applications, IEEE Transactions on*, vol. 46, pp. 2424-2433, 2010.

[16] D. M. Ionel and M. Popescu, "Ultrafast Finite-Element Analysis of Brushless PM Machines Based on Space and Time Transformations," *Industry Applications, IEEE Transactions on*, vol. 47, pp. 744-753, 2011.

[17] G. Y. Sizov, "Design Synthesis and Optimization of Permanent Magnet Synchronous Machines Based on Computationally-Efficient Finite Element Analysis," Ph.D. dissertation, Department of Electrical and Computer Engineering, *Marquette University*, Milwaukee, WI, 2013 ProQuest Dissertations and Theses.

[18] P. Zhang, "A novel design optimization of a fault-tolerant ac permanent magnet machine-drive system," Department of Electrical and Computer Engineering, *Marquette University*, Milwaukee, WI, 2013. ProQuest Dissertations and Theses

[19] K. Deb, *Multi-Objective Optimization Using Evolutionary Algorithms*. New York: John Wiley & Sons, Inc., 2001.

[20] K. V. Price, R. M. Storn, and J. A. Lampinen, *Differential evolution : a practical approach to global optimization*. Berlin ; New York: Springer, 2005.

[21] W. Price, "Global optimization by controlled random search," *Journal of Optimization Theory and Applications*, vol. 40, pp. 333-348, 1983.

[22] R. Eberhart and J. Kennedy, "A new optimizer using particle swarm theory," in *Micro Machine and Human Science, 1995. MHS '95., Proceedings of the Sixth International Symposium on*, Nagoya, Japan, 1995, pp. 39-43.

[23] S. Dong-Joon, C. Dong-Hyeok, C. Jang-Sung, J. Hyun-Kyo, and C. Tae-Kyoung, "Efficiency optimization of interior permanent magnet synchronous motor using genetic algorithms," *Magnetics, IEEE Transactions on,* vol. 33, pp. 1880-1883, 1997.

[24] N. Bianchi and S. Bolognani, "Design optimisation of electric motors by genetic algorithms," *Electric Power Applications, IEE Proceedings* -, vol. 145, pp. 475-483, 1998.

[25] W. Y. Jiang, T. M. Jahns, T. A. Lipo, W. Taylor, and Y. Suzuki, "Machine Design Optimization Based on Finite Element Analysis in a High-Throughput Computing Environment," *2012 IEEE Energy Conversion Congress and Exposition (ECCE),* pp. 869-876, 2012.

[26] R. M. Saunders, "Digital computers as an aid in electric-machine design," *American Institute of Electrical Engineers, Part I: Communication and Electronics, Transactions of the,* vol. 73, pp. 189-192, 1954.

[27] G. F. Uler, O. A. Mohammed, and K. Chang-seop, "Utilizing genetic algorithms for the optimal design of electromagnetic devices," *Magnetics, IEEE Transactions on,* vol. 30, pp. 4296-4298, 1994.

[28] G. Y. Sizov, D. M. Ionel, and N. A. O. Demerdash, "A Review of Efficient FE Modeling Techniques with Applications to PM AC Machines," *2011 IEEE Power and Energy Society General Meeting,* 2011.

[29] F. Parasiliti, M. Villani, S. Lucidi, and F. Rinaldi, "Finite-Element-Based Multiobjective Design Optimization Procedure of Interior Permanent Magnet Synchronous Motors for Wide Constant-Power Region Operation," *IEEE Transactions on Industrial Electronics,* vol. 59, pp. 2503-2514, Jun 2012.

[30] H. Liang-Yi, T. Mi-Ching, and H. Chien-Chin, "Efficiency optimization of brushless permanent magnet motors using penalty genetic algorithms," in *Electric Machines and Drives Conference, 2003. IEMDC'03. IEEE International*, Madison, WI, 2003, pp. 365-369 vol.1.

[31] N. Bianchi and A. Canova, "FEM analysis and optimisation design of an IPM synchronous motor," in *Power Electronics, Machines and Drives, 2002. International Conference on (Conf. Publ. No. 487)*, Bath, UK, 2002, pp. 49-54.

[32] R. Wrobel and P. H. Mellor, "Design Considerations of a Direct Drive Brushless Machine With Concentrated Windings," *Energy Conversion, IEEE Transactions on*, vol. 23, pp. 1-8, 2008.

[33] G. Pellegrino and F. Cupertino, "FEA-based multi-objective optimization of IPM motor design including rotor losses," in *Energy Conversion Congress and Exposition (ECCE), 2010 IEEE*, Atlanta, GA, 2010, pp. 3659-3666.

[34] G. Pellegrino, F. Cupertino, and C. Gerada, "Barriers shapes and minimum set of rotor parameters in the automated design of Synchronous Reluctance machines," in *Electric Machines & Drives Conference (IEMDC), 2013 IEEE International*, Chicago, IL, 2013, pp. 1204-1210.

[35] G. Pellegrino, F. Cupertino, and C. Gerada, "Automatic Design of Synchronous Reluctance Motors focusing on Barrier Shape Optimization," *Industry Applications, IEEE Transactions on*, vol. PP, pp. 1-1, 2014.

[36] Z. Peng, D. M. Ionel, and N. A. O. Demerdash, "Morphing parametric modeling and design optimization of spoke and V-type permanent magnet machines by combined design of experiments and differential evolution algorithms," in *Energy Conversion Congress and Exposition (ECCE), 2013 IEEE*, Denver, CO, 2013, pp. 5056-5063.

[37] C. Dong-Hyeok, J. Hyun-Kyo, and S. Dong-Joon, "Multiobjective optimal design of interior permanent magnet synchronous motors considering improved core loss formula," *Energy Conversion, IEEE Transactions on*, vol. 14, pp. 1347-1352, 1999.

[38] M. L. Bash and S. D. Pekarek, "Trends on the Pareto-optimal fronts of a portable generator drive system," in *Applied Power Electronics Conference and Exposition (APEC), 2012 Twenty-Seventh Annual IEEE*, Orlando, FL, 2012, pp. 931-937.

[39] P. Zhang, G. Y. Sizov, M. Li, D. M. Ionel, N. A. Demerdash, S. J. Stretz, *et al.*, "Multi-objective Tradeoffs in the Design Optimization of a Brushless Permanent Magnet Machine with Fractional-Slot Concentrated Windings," *Industry Applications, IEEE Transactions on*, vol. PP, pp. 1-1, 2014.

[40] Arnold Magnetics *ARNOX® Permanent Magnets: Hard Ferrite Material*, Available: http://www.arnoldmagnetics.com/.accessed 01/15/2014

[41] W. S. Janna, *Engineering heat transfer*. Boca Raton, FL: CRC Press, 1999.

[42] D. Staton, A. Boglietti, and A. Cavagnino, "Solving the More Difficult Aspects of Electric Motor Thermal Analysis in Small and Medium Size Industrial

Induction Motors," *Energy Conversion, IEEE Transactions on,* vol. 20, pp. 620-628, 2005.

[43] A. Boglietti, A. Cavagnino, D. Staton, M. Shanel, M. Mueller, and C. Mejuto, "Evolution and modern approaches for thermal analysis of electrical machines," *Industrial Electronics, IEEE Transactions on,* vol. 56, pp. 871-882, 2009.

[44] C. Gazley, "Heat Transfer Characteristics of rotating and axial flow between concentric cylinders," *Trans ASME,* pp. pp.79-89, 1958.

[45] A. Boglietti, A. Cavagnino, and D. Staton, "Determination of Critical Parameters in Electrical Machine Thermal Models," *Industry Applications, IEEE Transactions on,* vol. 44, pp. 1150-1159, 2008.

[46] D. C. Meeker, "Finite Element Method Magnetics, Version 4.2 (April 2012 Build) www.femm.info," 2009.

[47] J. R. Shewchuk, "Triangle: Engineering a 2D quality mesh generator and Delaunay triangulator," in *Applied computational geometry towards geometric engineering*, ed: Springer, 1996, pp. 203-222.

[48] T. A. Lipo, *Introduction to AC machine design*. Madison, WI: WisPERC, University of Wisconsin, 2011.

[49] J. J. C. Gyselinck, L. Vandevelde, and J. A. A. Melkebeek, "Multi-slice FE modeling of electrical machines with skewed slots-the skew discretization error," *Magnetics, IEEE Transactions on,* vol. 37, pp. 3233-3237, 2001.

[50] M. Popescu and D. G. Dorrell, "Skin effect and proximity losses in high speed brushless permanent magnet motors," in *Energy Conversion Congress and Exposition (ECCE), 2013 IEEE*, Denver, CO, 2013, pp. 3520-3527.

[51] K. Atallah, Z. Q. Zhu, and D. Howe, "An improved method for predicting iron losses in brushless permanent magnet DC drives," *Magnetics, IEEE Transactions on,* vol. 28, pp. 2997-2999, 1992.

[52] D. M. Ionel, M. Popescu, S. J. Dellinger, T. J. E. Miller, R. J. Heideman, and M. I. McGilp, "On the variation with flux and frequency of the core loss coefficients in electrical machines," *Industry Applications, IEEE Transactions on,* vol. 42, pp. 658-667, 2006.

[53] D. M. Ionel, M. Popescu, M. I. McGilp, T. J. E. Miller, S. J. Dellinger, and R. J. Heideman, "Computation of Core Losses in Electrical Machines Using Improved Models for Laminated Steel," *Industry Applications, IEEE Transactions on,* vol. 43, pp. 1554-1564, 2007.

[54] J. K. Tangudu, T. Jahns, and T. P. Bohn, "Design, analysis and loss minimization of a fractional-slot concentrated winding IPM machine for traction applications," in *Energy Conversion Congress and Exposition (ECCE), 2011 IEEE*, Phoenix, AZ, 2011, pp. 2236-2243.

[55] M. Mirzaei, A. Binder, and C. Deak, "3D analysis of circumferential and axial segmentation effect on magnet eddy current losses in permanent magnet synchronous machines with concentrated windings," in *Electrical Machines (ICEM), 2010 XIX International Conference on*, Rome, Italy, 2010, pp. 1-6.

[56] P. Zhang, G. Y. Sizov, J. B. He, D. M. Ionel, and N. A. D. Demerdash, "Calculation of Magnet Losses In Concentrated-Winding Permanent Magnet Synchronous Machines Using a Computationally Efficient - Finite Element Method," *2012 IEEE Energy Conversion Congress and Exposition (ECCE),* pp. 3363-3370, 2012.

[57] D. M. Saban, "Eddy-current losses in the sleeves of high-speed synchronous permanent-magnet machines," Ph.D., Electrical and Computer Engineering, *The University of Wisconsin - Madison*, Madison, Wisconsin, 2006. ProQuest Dissertations and Theses

[58] T. M. Jahns and V. Caliskan, "Uncontrolled generator operation of interior PM synchronous machines following high-speed inverter shutdown," *Industry Applications, IEEE Transactions on*, vol. 35, pp. 1347-1357, 1999.

[59] J. E. Vrancik, "Prediction of Windage Power Loss in Alternators," *NASA*, 1968.

[60] Mitch Olszewski, "Evaluation of the 2010 Toyota Prius Hybrid Synergy Drive System," O.R.N.L. 2011.

[61] A. Mesrobian and J. H. Holdrege, "Random wound versus form wound on low voltage synchronous generators," in *Petroleum and Chemical Industry Conference, 1990. Record of Conference Papers., Industry Applications Society 37th Annual*, Houston, TX, 1990, pp. 185-190.

[62] H. Akita, Y. Nakahara, N. Miyake, and T. Oikawa, "New core structure and manufacturing method for high efficiency of permanent magnet motors," in *Industry Applications Conference, 2003. 38th IAS Annual Meeting. Conference Record of the*, Salt Lake City, Utah, 2003, pp. 367-372 vol.1.

[63] K. Rahman, S. Jurkovic, C. Stancu, J. Morgante, and P. Savagian, "Design and performance of electrical propulsion system of extended range electric vehicle (EREV) Chevrolet Voltec," in *Energy Conversion Congress and Exposition (ECCE), 2012 IEEE*, Raleigh, NC, 2012, pp. 4152-4159.

[64] H. Lei, "Design and analysis of IPM machine with bar wound fractional slot distributed winding for automotive traction application," presented at the Energy Conversion Congress and Exposition (ECCE), 2013 IEEE, 2013.

[65] R. Wrobel, J. Goss, A. Mlot, and P. Mellor, "Design considerations of a brushless open-slot radial-flux PM hub motor," in *Energy Conversion Congress and Exposition (ECCE), 2012 IEEE*, Raleigh, NC, 2012, pp. 3678-3685.

[66] A. G. Jack, B. C. Mecrow, P. G. Dickinson, D. Stephenson, J. S. Burdess, N. Fawcett, *et al.*, "Permanent-magnet machines with powdered iron cores and prepressed windings," *Industry Applications, IEEE Transactions on*, vol. 36, pp. 1077-1084, 2000.

[67] A. M. El-Refaie, "Fractional-Slot Concentrated-Windings Synchronous Permanent Magnet Machines: Opportunities and Challenges," *Industrial Electronics, IEEE Transactions on*, vol. 57, pp. 107-121, 2010.

[68] L. J. Wu and Z. Q. Zhu, "Analytical investigation of open-circuit eddy current loss in windings of PM machines," in *Electrical Machines (ICEM), 2012 XXth International Conference on*, Marseille, France, 2012, pp. 2759-2765.

[69] Y. Deshpande, H. A. Toliyat, and W. Xiaoyan, "Standstill position estimation of SPMSM," in *IECON 2012 - 38th Annual Conference on IEEE Industrial Electronics Society*, Montreal, Canada, 2012, pp. 2024-2029.

[70] S. Byeong-Mun, C. Ki-Chan, and C. Jang-Young, "Design of an outer-rotor-type permanent magnet motor for electric scooter propulsion systems," in *Power Electronics Conference (IPEC), 2010 International*, Sapporo, Japan, 2010, pp. 2763-2742.

[71] S. S. Nair, S. Nalakath, I. Santhi, S. Jabez Dhinagar, Y. B. Deshpande, and H. A. Toliyat, "Design aspects of high torque density-low speed permanent magnet motor for electric two wheeler applications," in *Electric Machines & Drives Conference (IEMDC), 2013 IEEE International*, Chicago, IL, 2013, pp. 768-774.

[72] Weh H., and H. May., "Achievable Force Densities for Permanent Magnet Excited Machines in new Configurations," *Electrical Machines (ICEM), 1986 International Conference on*, Vol. 3.

[73] Y. Amara, P. Reghem, and G. Barakat, "Analytical Prediction of Eddy-Current Loss in Armature Windings of Permanent Magnet Brushless AC Machines," *Magnetics, IEEE Transactions on*, vol. 46, pp. 3481-3484, 2010.

[74] A. M. El-Refaie and T. M. Jahns, "Impact of winding layer number and magnet type on synchronous surface PM machines designed for wide constant-power

speed range operation," *IEEE Transactions on Energy Conversion*, vol. 23, pp. 53-60, Mar 2008.

[75] R. Wrobel, P. H. Mellor, N. McNeill, and D. A. Staton, "Thermal Performance of an Open-Slot Modular-Wound Machine With External Rotor," *Energy Conversion, IEEE Transactions on,* vol. 25, pp. 403-411, 2010.

[76] D. A. Staton and A. Cavagnino, "Convection Heat Transfer and Flow Calculations Suitable for Analytical Modelling of Electric Machines," in *IEEE Industrial Electronics, IECON 2006 - 32nd Annual Conference on*, Paris, France, 2006, pp. 4841-4846.

[77] J. Wenying and T. M. Jahns, "Development of efficient electromagnetic-thermal coupled model of electric machines based on finite element analysis," in *Electric Machines & Drives Conference (IEMDC), 2013 IEEE International*, Chicago, IL, 2013, pp. 816-823.

[78] M. Morandin, M. Ferrari, and S. Bolognani, "Design and performance of a power train for mild-hybrid motorcycle prototype," in *Electric Machines & Drives Conference (IEMDC), 2013 IEEE International*, Chicago, IL, 2013, pp. 1-8.

[79] M. Barcaro and N. Bianchi, "Interior PM machines using Ferrite to substitute rare-earth surface PM machines," in *Electrical Machines (ICEM), 2012 XXth International Conference on*, Marseille, France, 2012, pp. 1339-1345.

[80] R. R. Moghaddam, F. Magnussen, and C. Sadarangani, "Novel rotor design optimization of Synchronous Reluctance Machine for low torque ripple," in *Electrical Machines (ICEM), 2012 XXth International Conference on*, Marseille, France, 2012, pp. 720-724.

[81] P. Niazi, H. A. Toliyat, and A. Goodarzi, "Robust maximum torque per ampere (MTPA) control of PM-assisted SynRM for traction applications," *IEEE Transactions on Vehicular Technology*, vol. 56, pp. 1538-1545, Jul 2007.

[82] M. Sanada, Y. Inoue, and S. Morimoto, "Rotor Structure for Reducing Demagnetization of Magnet in a PMASynRM with Ferrite Permanent Magnet and its Characteristics," *2011 IEEE Energy Conversion Congress and Exposition (ECCE)*, pp. 4189-4194, 2011.

[83] S.-H. Han, "Reduction of core losses and torque ripple in interior permanent magnet synchronous machines," Ph.D., Electrical and Computer Engineeering, *The University of Wisconsin - Madison*, Madison, Wisconsin, 2010. ProQuest Dissertations and Theses

[84] A. Vagati, B. Boazzo, P. Guglielmi, and G. Pellegrino, "Design of Ferrite-Assisted Synchronous Reluctance Machines Robust Toward Demagnetization," *Industry Applications, IEEE Transactions on,* vol. 50, pp. 1768-1779, 2014.

[85] *Preliminary Technical Support Document: Energy Efficiency Program for Commercial Equipment: Energy Conservation Standards for Electric Motors,* Public document by U.S. Department. of. Energy, Office of Energy Efficiency and Renewable Energy, Washington DC, 2012.

[86] J. D. Widmer, C. M. Spargo, G. J. Atkinson, and B. C. Mecrow, "Solar Plane Propulsion Motors With Precompressed Aluminum Stator Windings," *Energy Conversion, IEEE Transactions on,* vol. PP, pp. 1-8, 2014.

[87] K. Shirabe, M. M. Swamy, K. Jun-Koo, M. Hisatsune, W. Yifeng, D. Kebort, *et al.*, "Efficiency Comparison Between Si-IGBT-Based Drive and GaN-Based Drive," *Industry Applications, IEEE Transactions on,* vol. 50, pp. 566-572, 2014.

[88] T. Morita, S. Tamura, Y. Anda, M. Ishida, Y. Uemoto, T. Ueda, *et al.*, "99.3% Efficiency of three-phase inverter for motor drive using GaN-based Gate Injection Transistors," in *Applied Power Electronics Conference and Exposition (APEC), 2011 Twenty-Sixth Annual IEEE*, Fort Worth, TX, 2011, pp. 481-484.

[89] J. J. Kreidler, W. K. Anderson, S. Venkateswarrao, B. J. Conway, H. D. Willis, and P. Wung, "Roll Up Stator Development for 56 Frame PM Synchronous Motor," in *Energy Conversion Congress and Exposition (ECCE), 2014 IEEE*, Pittsburgh, PA, 2014.

[90] K. Weeber and S. R. H. Hoole, "Geometric parametrization and constrained optimization techniques in the design of salient pole synchronous machines," *Magnetics, IEEE Transactions on,* vol. 28, pp. 1948-1960, 1992.